ABSTRACT

Title of Document:	**EXPERIMENTAL INVESTIGATION OF WING-FUSELAGE INTEGRATION GEOMETRIES INCLUDING CFD ANALYSES**
	Jirapat Supamusdisukul, Master of Science, 2008
Directed By:	Dr. Jewel Barlow Associate Professor Department of Aerospace Engineering and Director of Glenn L. Martin Wind Tunnel

A wind tunnel experiment exploring the influence of interface geometry on wing-body aerodynamics is described and the results are presented. The investigation focuses on the interference effects that occur for several wing-body geometries that are considered candidates for a design of an airplane intended to operate at low subsonic speeds at high altitude. The geometries of the test models were developed by Aurora Flight Sciences as in the process of evolving a preliminary design for a potential future unmanned aerial vehicle. With the support of the Glenn L. Martin Wind Tunnel at the University of Maryland, an experimental program has been carried out in which force data were obtained to identify the most promising wing-fuselage geometries for future detailed development. The research also included computational fluid dynamics simulations to explore flow characteristics around these wing-fuselage systems in greater detail than was possible in the experiments. The experimental data and simulation results are discussed in this thesis.

EXPERIMENTAL INVESTIGATION OF WING-FUSELAGE INTEGRATION
GEOMETRIES INCLUDING CFD ANALYSES

By

Jirapat Supamusdisukul

Thesis submitted to the Faculty of the Graduate School of the
University of Maryland, College Park, in partial fulfillment
of the requirements for the degree of
Master of Science
2008

Advisory Committee:
Professor [Jewel Barlow], Chair and Advisor
Professor John Anderson
Professor Allen Winkelmann

Acknowledgements

I would like to express my sincere appreciation to my advisor, Dr. Jewel Barlow, for his guidance in this accomplishment. This work would not have been possible without the support of Dr. Barlow. Throughout research, he has provided me encouragement through difficult time, inspiration when needed, and good advice for better understanding of materials. Dr. Barlow, thank you for your dedication and investment in me as your graduate student.

I would like to give a special thank to the Aurora Flight Sciences, and especially project leaders, Daniel Hatfield, and Patrick Garrets, for their dedication on this wind-tunnel experiment. Daniel and Patrick, thank you for your time and effort invested in this project.

I wish to thank for friends and colleagues for the helps and supports. Evandro Gurgel Do Amaral Valente, thanks for your guidance with Rhinoceros. Thanks the wind tunnel team for their help during the experiment. Other thanks for friends who studied together through difficult graduate classes.

With love and respect, I greatly appreciate my parents for their inspiration, encouragement, and great supports. The thesis is dedicated for you.

Table of Contents

List of Tables

List of Figures

Nomenclatures

BF   = Bluntness Factor

R_o = Leading edge radius

X_T = Chord wise position of maximum thickness

S_T = Distance from leading edge along the airfoil surface to maximum thickness

T   = Maximum thickness

Γ = Circulation

I   = Turbulent Intensity

L   =   Lift

D   = Drag

C_L = Lift Coefficient

C_D = Drag Coefficient

α = Angle of attack

ρ = Air density

R   = Radius of Fuselage

c   = Wing Chord length

P   = Pressure

K   = Kinetic Energy

Chapter 1: Introduction

Generally, the purpose of aerodynamic analysis of an airplane is to optimize

aerodynamic performance. That is to maximize lift for a given amount of drag, and

conversely to minimize drag for a given amount of lift. Shapes and contours of

individual components and parts on aircraft affect the amount of total aircraft drag.

Nevertheless, the total drag further rises when combining these parts into an airplane.

This increment in drag is called interference drag. It is known to contribute

significantly to overall drag of aircraft. Flowfields generated by complex wing-

fuselage junction geometries have yet remained to be understood and controlled.

Therefore, the investigation of various configurations of aircraft is needed to reach

the goal of optimum aerodynamic design.

Many changes on major components of aircraft have been made to satisfy

performance characteristics. Interference drag related to wing location is among the

problem areas to be understood in order to accomplish design optimization. Different

wing locations lead to different interaction behaviors between the wing and fuselage.

Changing the wing location in horizontal or vertical fashion changes forces and

moments acting on the aircraft wing and body. Although this matter has been widely

studied, a specific wing and fuselage may not behave as others that seem to be

similar. It is rather the case that the wing-fuselage interface behavior is still an

unsolved issue in many designs. The interference between wing and fuselage

frequently causes complex turbulence and separation of the flow in the vicinity of the

junction. Thus, it is necessary to perform research to determine the details of the effects of wing locations for better understanding of characteristics for each considered configuration of an aircraft.

The investigation in this paper concentrates on the determination of aerodynamic forces, especially effects on drag and lift to drag ratio, of a selected set or family of configurations of a single wing geometry an a single fuselage geometry. The aircraft is designed for high-lift, low Reynolds number flight in the low speed incompressible flow regime. Five configurations were defined which are distinguished primarily by variation of wing height. There are other differences in detail due to the need to choose a fairing for each wing height and each of these necessarily differs somewhat from others. The boundary layers of the wing surface and the fuselage interact which is a manifestation of the existence of interference effects. By varying the wing height, the aerodynamic forces on the body of each configuration are altered by unique interference effects. The interference effects generally reduce lift, and increase drag relative to the values for the sum of the lift and drag for the wing and the fuselage in isolation. These increments are known as interference drag and interference lift.

The incentive of this work is specifically to assist a preliminary design for a UAV (Unmanned Aerial Vehicle) developed by Aurora Flight Sciences. The aircraft is designed for a long range mission; hence high aerodynamic performance is one of the important keys to a successful design. Nevertheless, the results could provide benefits to a range of potential design of low-speed incompressible aircraft.

Chapter 2: Theoretical Background and Literature Review

2.1 Wing-Fuselage Junction Flow

Wing-Fuselage junction flow occurs when the boundary layer on a fuselage encounters an obstacle placed on its surface[5]. The result is an interrupted boundary layer causing changes in pressure gradient at the intersection area, which leads to three dimensional separations with horseshoe vortices wrapping around the wing surface. Adverse pressure gradients occur and the cause approach boundary layer on the fuselage separate before reaching the wing surface. This causes multiple horseshoe vortices to form starting in front of the wing leading edge, and the vortex filament to stretch as they are moving in the downstream direction. Figure 1 shows the schematic of an idealized wing-fuselage juncture encountering the flow along its body. The separation occurs at the junction with horseshoe vortices formed and stretched along the obstacle. The stagnation point occurs on the surface forming a separation line of vortices traveling along the wing and fuselage body. Generally, these vortices are highly unsteady, and lead to turbulent flow downstream on the surface. As a consequence of flow interaction, load distributions, forces, pressure distributions on body near junction can be significantly altered.

SEPARATED BOUNDARY LAYER.

STREAMLINE OFF WALL.

'LIMITING' STREAMLINES ON WALL.

ATTACHMENT LINE MAY LIE EITHER ON WING OR WALL.

SEPARATION LINE.

SECONDARY SEPARATION PRODUCING EITHER A SECONDARY VORTEX, AS ILLUSTRATED, OR A BUBBLE.
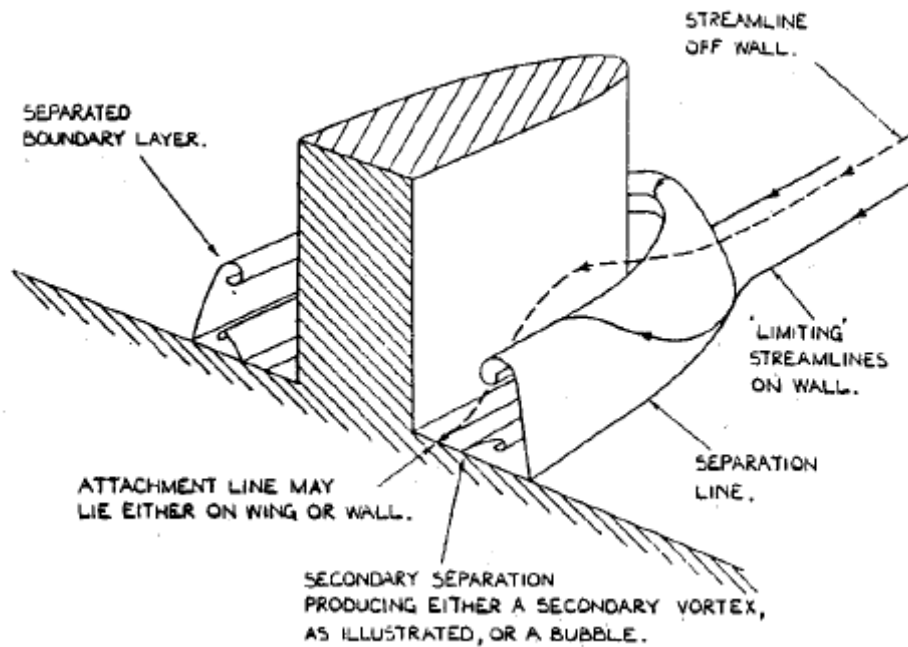
Figure 1: The flowfield around the obstacle in an idealized case of fuselage juncture [9]

Simpson explained factors that determine characteristics of junction flow including nose bluntness, Reynolds number, displacement thickness of approach boundary layer, free-stream turbulence levels, and surface roughness[5]. The nose bluntness is commonly related to separation lines, and stagnation point. The effect of nose shape can be accounted for by introducing the "bluntness factor" (BF), in which it is defined as,

$$BF = \frac{1}{2} \frac{R_0}{X_T} \left[\frac{T}{S_T} + \frac{S_T}{X_T} \right]$$

Where R_0 = leading-edge radius

X_T = chord wise position of the maximum thickness T

S_T = Distance from the leading edge along the airfoil surface to

Maximum thickness

A higher bluntness factor means the more possibility of stronger flow separations. Moreover, the effects of high Reynolds numbers increase the intensity of velocity components of the vortices and their neighbors. This causes the behavior of vortices to interact strongly with the vortices adjacent to them and nearby, called "leapfrog" behavior. They may also combine to form a larger vortex, or even lead to the formation of single large vortex, called a burst of vortex structure. These horseshoe vortices produce higher-speed velocity components than the freestream in a rotational behavior, which results in a drag increment along the obstacles. The angle of attack is also a variable in the wing-fuselage junction flow. Nonzero angles of attacks cause the approach flow to experience a larger effective blunt nose. This results in the formation of a stronger vortex system traveling along the body causing a greater amount of drag. Other effects such heat transfer from junction flow is not applicable in this case study which is for a low-speed incompressible flight condition.

The interactions between boundary layers of two surfaces; wing and fuselage, causes significant losses in aerodynamic efficiency. Many suggestions from researches over the years have been contributing to increasingly better methods of reducing drag from wing-fuselage junction flow effects. They have sometimes been attempts to design fuselage shapes to conform to the streamlines of the wing. Some research recommended using a shaped wing leading edge to minimize this effect; however, this may refer to restriction of the range of angles of attack. McGinley (1987) used vortex generators to produce counterrotating vortices in an attempt to nullify the horseshoe vortices from the junction flow[5].

By far, it seems that the most traditional and effective way to control the junction flows is by using a fairing. A fairing can substantially reduce interference drag of the junction (Hoerner) [3]. Simpson stated that Haines (1983) advises the main objectives of a fairing design are the following: (a) eliminate flow separations, including those that lead to standoff vortices, (b) reduce cross-flow in boundary layers, (c) merge different streams smoothly, and (d) avoid the development of thick boundary layers[5]. Smooth transition between wing and fuselage helps reduce strong impact by distributing force further along the side. This, in turn, cuts down the strength of the horseshoe vortices. Effective fairing design of fairing will help reduce adverse pressure gradients, lessen extent of separations, reduce vortex strength, and thus reduce interference drag.

2.2 Wing-Fuselage System

A wing-fuselage system in incompressible flow is the main focus of this study. Complication arises from the aerodynamic interaction between the two components. As is common knowledge, the wing is the main source of lift; nevertheless, the aerodynamics of fuselage should be paid attention not less than the wing itself. When the wing and the fuselage are assembled into wing-fuselage system, their aerodynamic interactions contribute to changes in the flows and in the aerodynamic force. The interference flow between components produces extra drag and alters lift components at the wing-fuselage junction. In some case, these alterations can be very drastic, but with attention to details, these adverse effects can be largely alleviated. One interesting remark, these interference problems are hardly

determinable theoretically, especially on interference drag. Experimental approach is considered to be more effective.

Wing-fuselage aerodynamics is a case of junction flow with basic features similar to that described in section 2.1. The streamline flow along the fuselage body is broken at the junction forming horseshoe vortices behind the juncture body. This causes changes in aerodynamic forces and their components which are most likely to deteriorate performance of the system. Typically the lift slope of a wing-fuselage combination remains similar to those of wing alone, but the maximum lift coefficient decreases by some extent. The moment coefficient is greatly moved into the positive direction. In the case of side-slip, a high-wing airplane typically tends to suffer a larger increment of rolling moment coefficient due to cross flow over the fuselage.
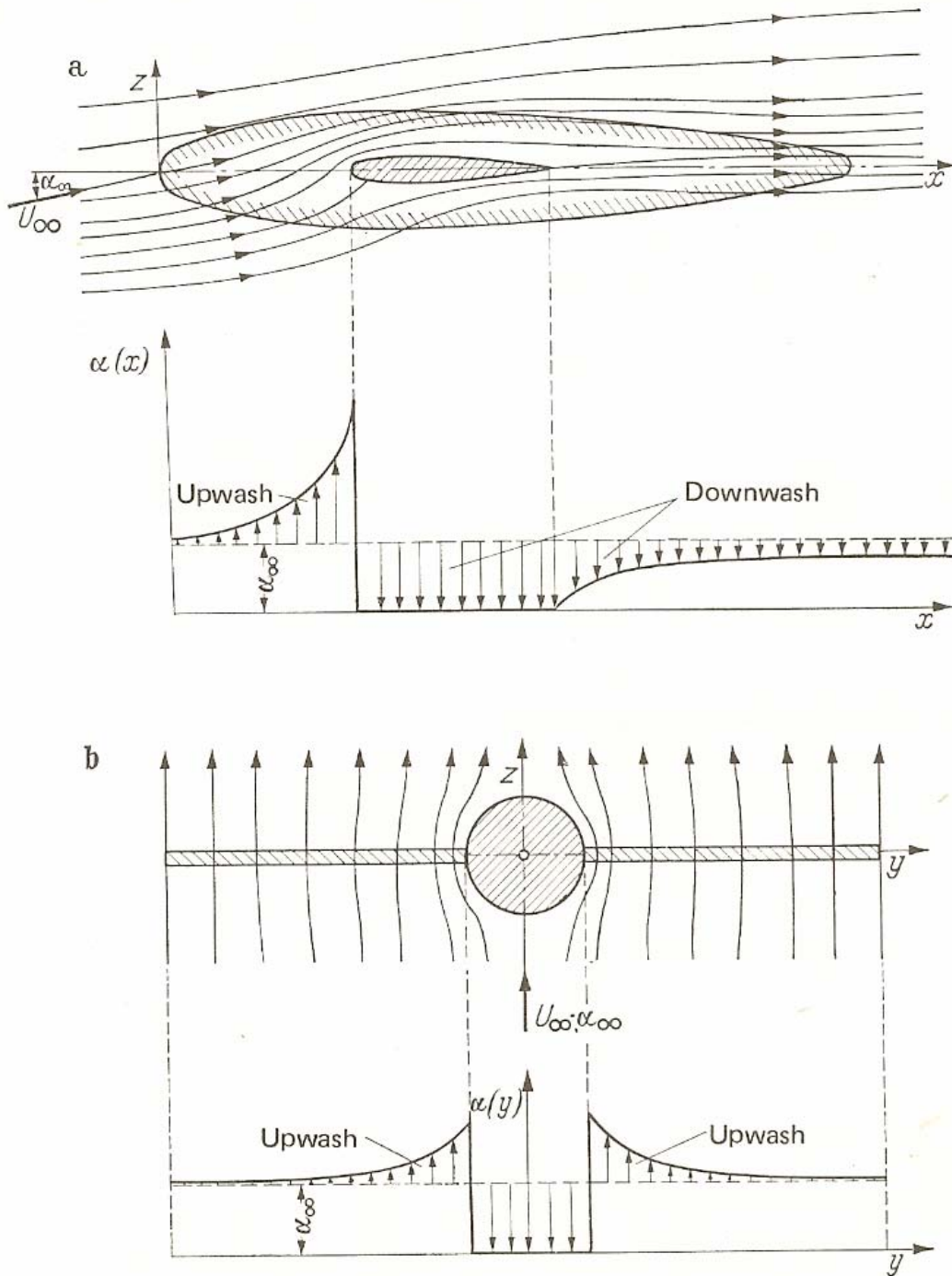
Figure 2: The general flowfield characteristics of wing-fuselage system with upwash and downwash components.(a) along fuselage axis (b) along wing spanwise axis[4]

A fundamental understanding of the flow field of the wing-fuselage is

desirable. The theoretical approach presented by Schilichting and Truckenbrodt is an

elaborated discussion on the aerodynamics of the wing-fuselage system. Subsonic incompressible and inviscid flow in symmetric about the xz plane is assumed[4]. Additive velocities normal to the fuselage axis are induced by the wing producing an upwash velocity field in front of the wing, and downwash components behind the wing. Figure 2 shows a schematic flow of upwash and downwash components of wing-fuselage system during flight with a constant angle of attack. The downwash components are continuously decreased in magnitude toward the end of fuselage. This shows that angle of attack distribution along the fuselage is greater in front of the wing; in which it implies that the wing-fuselage system is subjected to positive pitching moment. Moreover, the upwash components are distributed along the wing span, with discontinuous drop for downwash velocity within the range of fuselage along the wing span. The upwash component is larger toward the roots of the wing. One interesting point to note is that in cross flow the angle of attack distribution due to fuselage interference has opposite sign for high-wing and low-wing, but is neutral for mid-wing.

The lift distribution of wing-fuselage system can be determined by vortex and circulation principles. The horseshoe vortices of width dy with vortex strength Γ bounded around the wing-fuselage system and stretching downstream creates flow creating spanwise circulation distribution $\Gamma(y)$. Schilichting and Truckenbrodt explained how kinematics flow conditions must be satisfied by means of reflection principle; "for every free vortex outside of the fuselage, a vortex reflected with respect to a circle has to be placed into the fuselage that has the same vortex strength

but the opposite sense of direction of rotation"[4]. The imagery in Figure 3 below

explains the vortex system and lift circulation of wing-fuselage system.
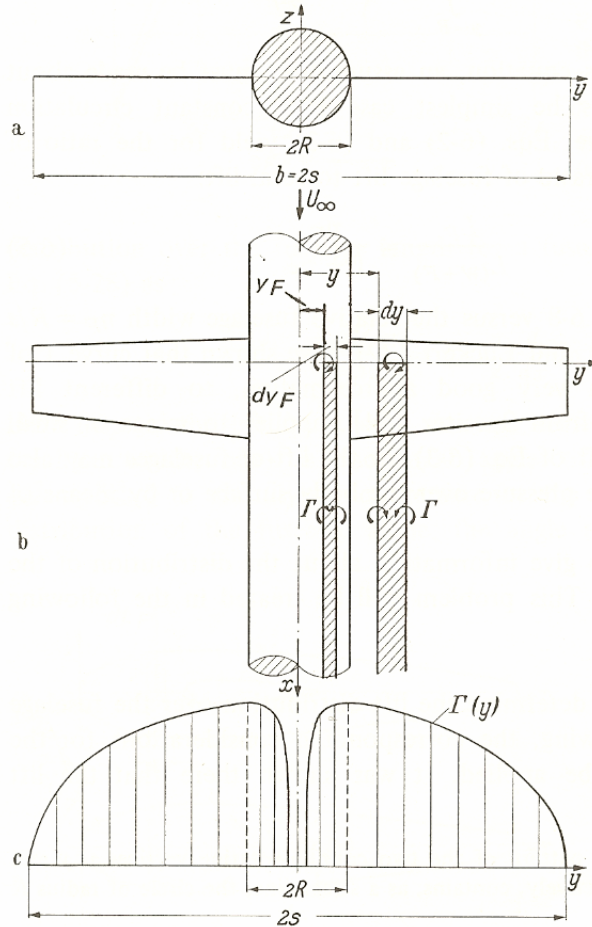
Figure 3: The schematic for total lift determination of wing-fuselage system. (a) rear view (b) top view with vortex system. (c) Circulation distribution spanwise of wing-fuselage[4]

Let y_F be the distance from fuselage axis defined as $y_F = R^2 / y$, in which R is radius

of fuselage cross section. This can be used for the estimation of total lift of wing-

fuselage system.

$$L_W' = 2\rho U_\infty \int_{y=R}^{s} \Gamma(y)dy \text{, Where } U_\infty = \text{freestream velocity}$$

Likewise, with $dy_F = -(R^2 / y^2)dy$, lift of fuselage can be approximated as,

$$L_F = 2\rho U_\infty \int_{yF=R^2/s}^{R} \Gamma(y_F)dy_F = \int_{y=R}^{s} \Gamma(y)\frac{R^2}{y^2}dy_F$$

Therefore, the total lift of wing-fuselage system is the summation of equations above, and can be expressed as;

$$L_{W+F} = L_W' + L_F = 2\rho U_\infty \int_{y=R}^{s} \Gamma(y)\left(1+\frac{R^2}{y^2}\right)dy$$

The above calculation can be accounted only in wing spanwise distribution, but it fails to represent lift distribution over the length of fuselage. To resolve that aspect one can consider the lift distribution of fuselage under the influence of the wing[4]. The angle of attack distribution is suitable for this subject as it has direct relation to the lift distribution. And the angle of attack distribution of the fuselage under the influence of the wing can be expressed as[4]

$$\alpha(x) = \alpha_\infty + \alpha_w(x) \quad ; \text{Where } \alpha_w(x) \text{ represents upwash and downwash angle}$$

induced by the wing at x location of fuselage.

Schilichting and Truckenbrodt concluded from the downwash distribution of an inclined profile of finite thickness for $\alpha_w(x)$, which yields local angle of attacks as[4],

$$\alpha(X) = \alpha_\infty \sqrt{\frac{X-1}{X}} \quad \text{For } X \geq 1 \text{ and } X < 0 \quad ; \text{Where } X = x/c$$

c = wing chord length and Within the range of the wing $\alpha(x) = -\alpha_\infty$, which gives

$$\alpha(X) = 0 \quad \text{For } 0 < X \leq 1$$

The equations above show that local angle of attack distribution is discontinuous at the wing leading edge. The upwash angle drops abruptly from positive $\alpha(X)$ to zero. This yields the result to lift distribution along the fuselage axis, where the lift profile

is peaked at the front of the wing leading edge. On the other hand, the lift peak of the wing, in general, is greatest at vicinity the wing leading edge. However, being compromised with fuselage lift distribution, it occurs that the lift peak of the wing is reduced by the negative lift peak of fuselage. Further analysis indicates that the effect of aspect ratio also plays an important role in the wing fuselage system. The upwash angles decreases as the aspect ratio is reduced, but the downwash angle becomes greater with decreasing aspect ratio.
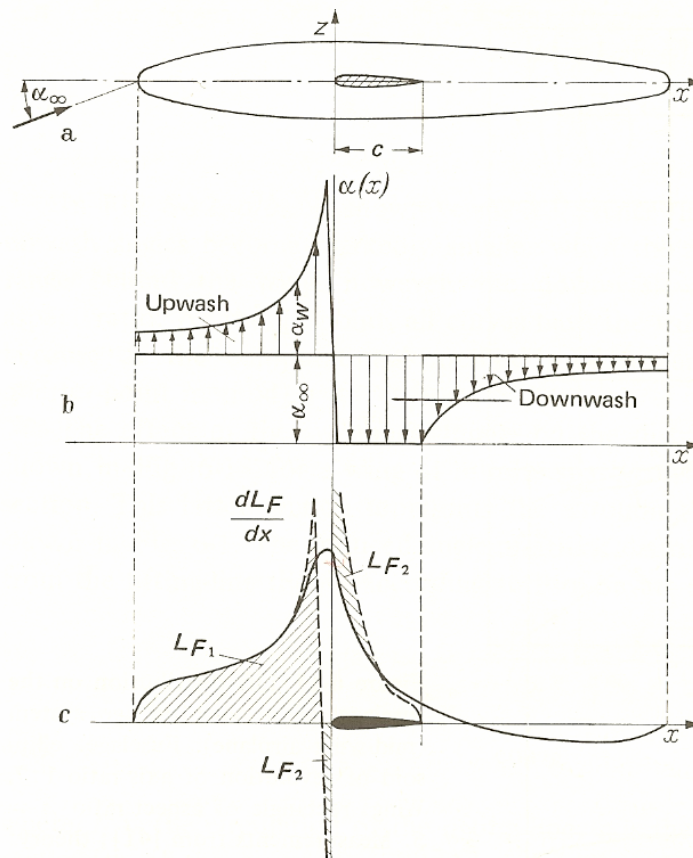
Figure 4: (a) General wing-fuselage system (b) angle of attack distribution (c) lift distribution[4]

Figure 4(b) shows the abrupt discontinuity of $\alpha(x)$ at the wing leading edge from large negative value of change in angle of attack. Change in angle of attack along the

system yields the lift distribution of fuselage. L_{F2} represents large negative value of lift on fuselage from the existence of the wing. This causes the sudden drop of fuselage angle of attack, and thus causes wing lift distribution, shown in solid curve, to be noticeably reduced at the leading edge.

The other case to consider is the lift distribution of the wing under the influence of fuselage. The data extracted from Moller pressure distribution measurement of mid-wing system with rectangular wing show the lift distribution of the wing with existence of fuselage[4]. The result exhibits favorable interference effects to slightly increase lift distribution of the wing outside the fuselage range with 3 angles of attacks. This, however, is considered to be a very small effect. The lift distribution within the fuselage range, on the other hand, drops substantially in comparison to that of wing alone.

The general aerodynamic characteristics of wing-fuselage system have been discussed. Further analysis is focused on wing position on fuselage. The maximum lift coefficient $C_{L\max}$ of wing-fuselage system depends greatly on wing position on fuselage body. The research investigation was conducted by Jacobs and Ward, and by Sherman, reviewed and published by Schilichting and Truckenbrodt[4]. The study reveals the effects of both vertical and horizontal wing position to maximum lift coefficient. According to figure 5(a), the wing rearward position shows continuous decrease in $C_{L\max}$ as the wing position moves toward the rear end of fuselage. The best case appears that $C_{L\max}$ approximately equal to the $C_{L\max}$ of the wing alone, but it is not practically possible since the wing must be placed near to fuselage nose. If the wing is located too much aft the fuselage, $C_{L\max}$ deteriorates significantly.

Furthermore, the effect of vertical wing position is favorable to both high-wing and low-wing airplanes, but is not beneficial for mid-wing design. As show in figure 5(b), the $C_{L\max}$ plot versus variation of wing high positions shows that wing located at the centerline of fuselage, the $C_{L\max}$ is the lowest. This makes the mid-wing airplane appear to be least favorable. The high-wing airplane generates the most favorable $C_{L\max}$ with its $C_{L\max}$ equal to or slightly higher than the $C_{L\max}$ of the wing alone. Similarly, the lowest wing position has its $C_{L\max}$ equal to the wing alone, but never greater. In shorts, the $C_{L\max}$ of the wing increases as the wing position is shifted to both high and low positions.
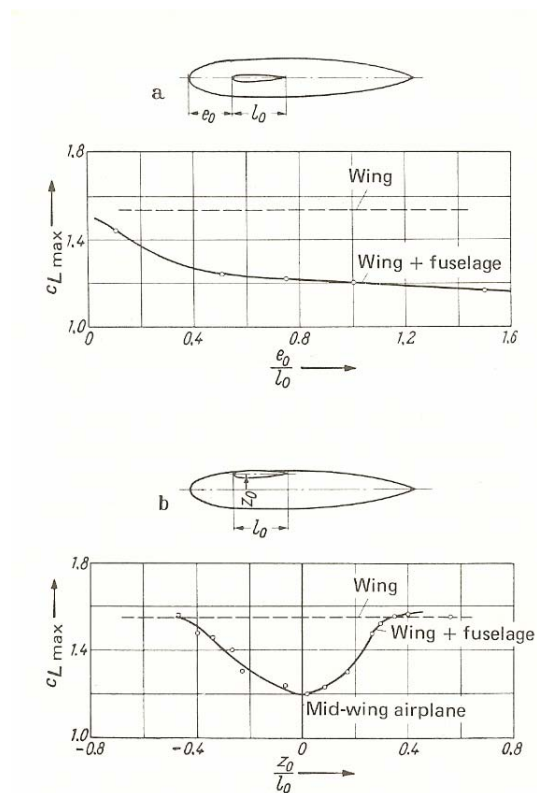
Figure 5: Maximum lift coefficient of wing-fuselage system (a) with variation of wing aft position, (b) with variation of wing high position[4]

14

The study on maximum lift coefficient yields useful insight of wing location characteristics. Drag on the wing-fuselage system is also important, but rather remains difficult to determine theoretically. However, researches and experiments have been done to illuminate this question. Further research is conducted by Kentfield and Jones on fuselage-wing interference drag of aircraft with relatively short, pod-type, fuselages[8]. The investigation is involved in studying interference drag on different configurations of fuselage with variation of wing positions. The study reveals that aerodynamic characteristics of low-wing aircraft is not preferable, except for the case that wings were mounted unrealistically towards the fuselage nose. With aft wing locations, the low-wing configuration produces unfavorable interference effects. Conversely, the high-wing fuselage configuration tends to produce favorable interference drag when the wing is located at realistically further back on fuselage, rather than in forward locations. This favorable interference effects help reduce total drag of aircraft. Although the study is constrained with short-pod type fuselage, one may assume other general types of fuselage follow the same trend within similar flight conditions.

The adverse effects of wing-fuselage system can be alleviated for better design performance. Many research efforts have been dedicated to solve this problem. Bradford E. Green and John L. Whitesides have published a method for designing leading-edge fillets to eliminate flow separation[11]. The research elaborates how changing fillet's surface slopes lead to variety of results. It overall shows great achievement to alleviate the effect of flow separation. Dickenson (1990) suggests a constant radius leading edge fillet that is twice the approach boundary layer

thickness[5]. Another traditional approach is to use a fairing to reduce flow separation effects. Good fairing design methodology is previously discussed in the earlier section. Experimental research investigation of wing-fuselage integration geometries by Maughmer, Hallman, Ruszkowski, Chappel, and Waitz conclude that a sharp-nosed fairing that extends the root section in the direction of the leading edge has much better performance than a blunted geometry[9]. Many methods can be applied to reduce adverse effects of wing-fuselage juncture flow. The most favorable design varies for different geometries of aircraft. Effective designs of these tools can help improve flow quality over wing-fuselage.

The interference effect of wing-fuselage remains difficult for theoretical prediction. Precise method of calculation has yet to be discovered. The experimental approach is still considered an efficient and accurate way to evaluate the wing-fuselage interference effects. Nevertheless, with today's technologies, Computational Fluid Dynamics (CFD) becomes a powerful tool to determine aerodynamic characteristics of any models, including wing-fuselage system. A wide range of studies can be done with CFD codes such as analysis on 3D turbulent junction flow in subsonic or supersonic speed. It potentially eases difficulty and complexion of wind tunnel experiments.

Chapter 3: Experimental Procedures and Methodology

3.1 Model Characteristics

3.1.1 Airfoil and Wing Characteristics

The wing airfoil section is a Mark Drela DAE-11, a low-Reynolds number airfoil used on the Daedalus human powered airplane, and modified within the Aurora Flight Sciences research team to have higher t/c and a longer laminar region on the upper surface for the operating Reynolds number of 9.0E5[7]. The original DAE-11 is designed to minimize the losses from the transitional separation bubbles without restoring mechanical turbulation. Such advantage is inherited to Orion-Root Airfoil promoting a long run of laminar flow, and reducing drag during the turbulent transition. Figure 6, shows the airfoil predicted characteristics. As indicated by Figure 7, the wing is installed at a 6.5 degree angle of incidence, which approximates best L/D angle of attack for the airfoil.
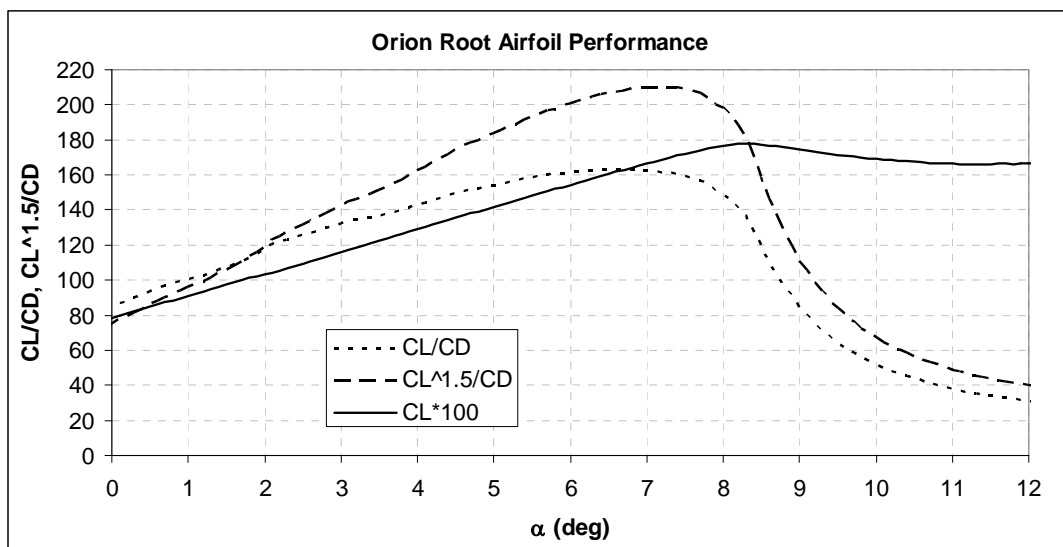
Figure 6: Predicted Orion Root Airfoil Performance (a) CL/CD, (b) CL$^{1.5}$/CD, (c) CL*100 [7]

The airfoil is designed to have maximum lift coefficient of approximately 1.8 with maximum lift to drag ratio of approximately 164 at 6.5 degree angle of attack. Minimum drag occurs at the value of 0.0087.
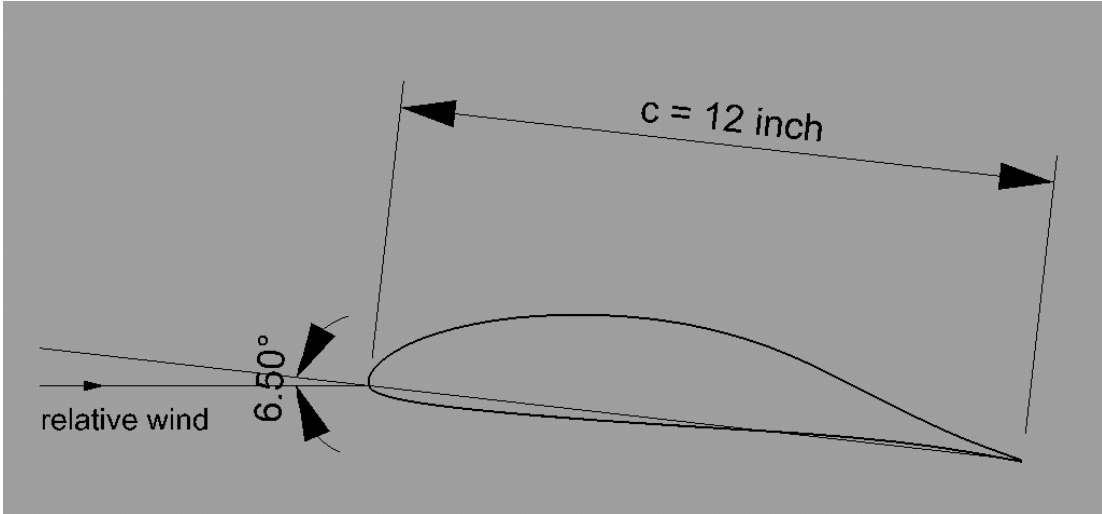
Figure 7: Airfoil layout showing wing schematic with 6.5 degrees incident angles as set up in the test section
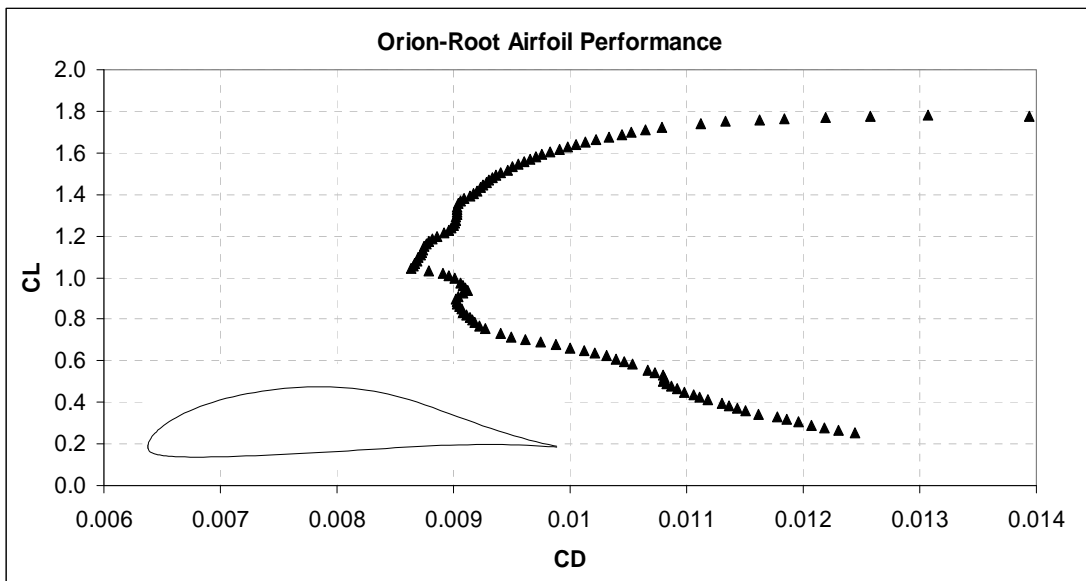
Figure 8: Predicted Orion Root Airfoil Performance featuring Lift coefficient vs. Drag Coefficient [7]

The non-swept, non-tapered rectangular wing has 12 inch constant chord length. It spans 131 and 3/8 inch across the wind tunnel wall with the incident angle set up at 6.5 degrees. The wing surface is covered with smooth carbon fiber composite material to help reduce skin friction drag. The setup of the wing is aerodynamically uncomplicated in that it is not equipped with aileron, flaps, and other wing components. This reflects the current focus on analysis of wing-fuselage interaction behavior. No tails are included in this experiment.

3.1.2 Fuselage Characteristics

The 1/5 scaled model is used to provide full scale Reynolds numbers. The fuselage is radially symmetric with 8.5 ft in length and 22 inches maximum diameter at $x/l = 0.3$. For the designed Mach number and Reynolds numbers, an airplane five times the size of the test model is expected to fly over 200 miles per hour at high altitude. The fuselage body is generally larger in the forward section and its radius gradually decreases towards the tail, nearly a tail-boom like. This serves to encourage natural laminar flow on the body. Another purpose of the fuselage design is possibly to allow maximum capacity for storing avionics and fuel at about the center of gravity of the aircraft. The designs of wing-fuselage, fairings vary for each model configuration, but they are expected to help maintain laminar flow on the body as much as possible.

3.1.3 Overview of the Five Tested Model Configurations

To study the effects of drag on different wing-fuselage configurations, the model system can be assembled into 5 distinctive arrangements. All use the same fuselage

and wing. The primary variable in this experiment the vertical positions of the wing on the fuselage. An L-strut holds the wing fixed to the fuselage, but it allows the vertical position of the wing to be changed by adjusting its height. The designs of fairings are applied to some configurations, and were intended to achieve the greatest possible drag reduction.

The wing positions vary from mid-body to well above the fuselage. The first configuration, shown in figure 9, has the wing located slightly higher than the mid-fuselage. The fuselage maintains its shape, only with the wing placed through its body. The middle section of the wing is fully covered by the fuselage. No fillet is installed in this model leaving a sharp corner at the wing-fuselage intersection.

Figure 9: Configuration 1 wing-fuselage geometry [7]

The configuration 2, shown in figure 10a, has its wing positioned partly above the fuselage. The fairing is designed to partially cover the top, back section of the wing to alleviate the effects from sharp conjunction between aft wing and fuselage. The configurations 3 and 4 as shown by Figure 10b and Figure 10c have their wing located well above the fuselage, with the wing height of configuration 4 higher than the height of configuration 3. The fairings extend from fuselage to the wing to help minimize separation, and wing-fuselage interference effects.
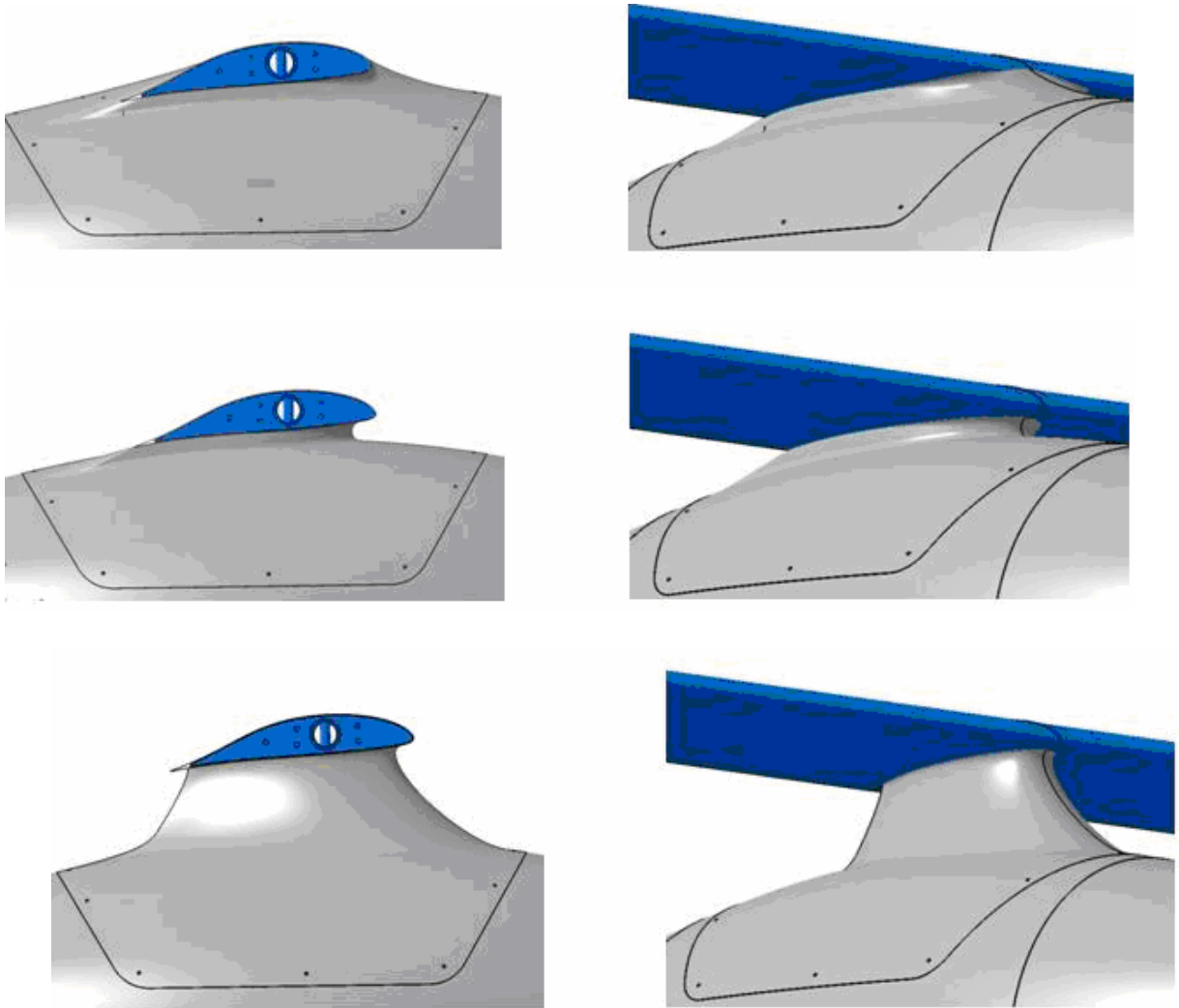
Figure 10: (a) Configuration 2, geometry (b) Configuration 3 geometry (c) Configuration 4 geometry. [7]

The wing-fuselage configuration 5, shown in figure 11, has its wing position high above the fuselage at a distance of 20.25 inches above fuselage center. The unsheltered strut is fully extended to support the wing, and connect it to the fuselage. No fillets or fairings cover wing-fuselage extension. The strut is relatively thin, and behaves as a flat plate. The design of configuration 5 is rather simple and aerodynamically clean.
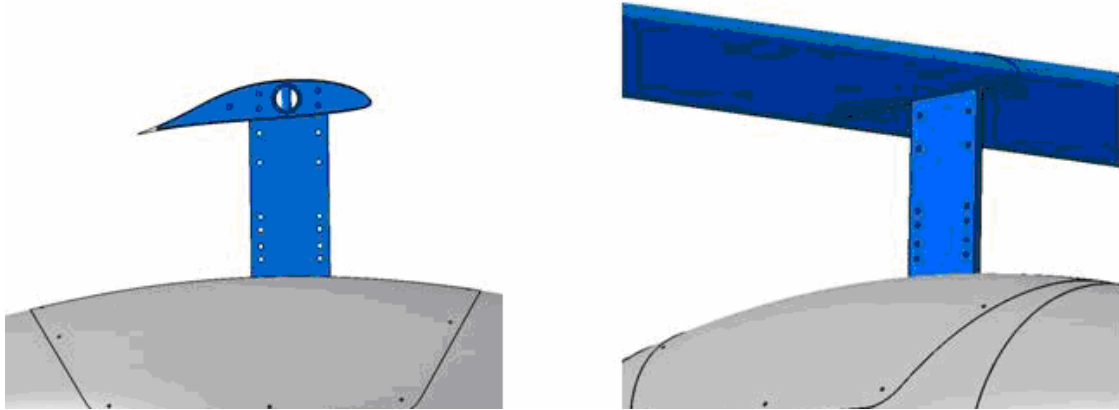
Figure 11: Configuration 5 geometry [7]

3.1.4 Wind Tunnel Description

The experiments for this study were done in the Glenn L. Martin wind tunnel

(GLMWT). The GLMWT is a low-speed subsonic, closed-circuit wind tunnel. It is

capable of generating wind speeds up to a maximum of 230 miles per hour, with

turbulence factor of 0.21%. Its test section is approximately 11 feet wide, 7.75 feet in

height, and 13 feet long. Models are fitted perfectly inside the test section. The

characteristics of the GLMWT are suitable for the test subject.

3.2 Experiment Methodology

3.2.1 Experiment Setup

The model is held fixed on the external balance of the wind tunnel. The wing

spans across the test section with small gaps on each side of the wing between the

wing tips and the side walls. The gap flows at the tips are remote from the

fuselage/wing intersections and are considered to be unaffected by the changes in the

wing/fuselage geometries understudy. Since the primary goal of this study is the

comparison of the effects of the wing/fuselage geometries, the gap flows at the wing

tips are simply considered to have a constant characteristic for all cases. No attempt is

made to correct for these gap flows. For data runs, the model mounted on 3 main

supports; 2 main struts and 1 pitch strut as shown by Figure 12 and 13. The L-fixture,

mentioned earlier, fixes the wing to the fuselage.
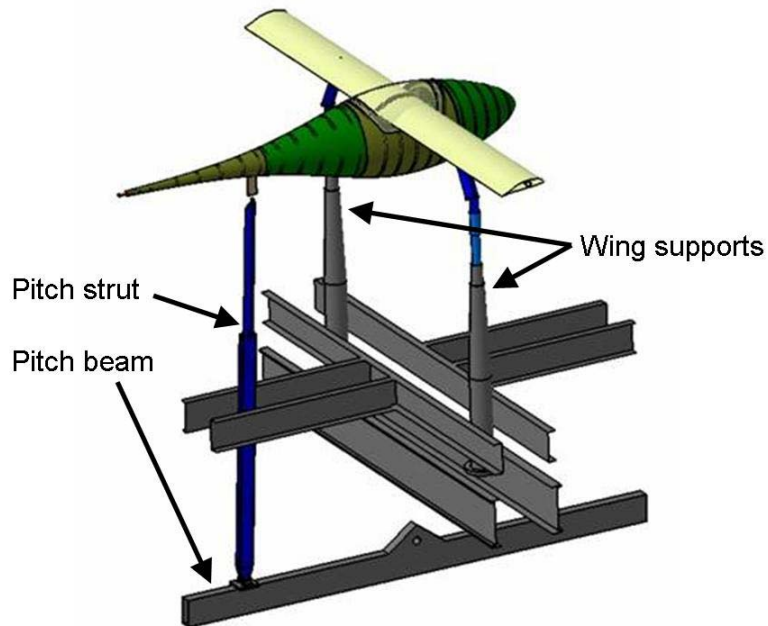
Figure 12: Experiment set up schematic on the wind tunnel test section and balances [7]

The Main Struts are non-movable, and are used to support the wing with

rotate-able connecting joint. Two Main struts support both sides of the wing in which

its stationary ends are fixed to the balance under test section floor. During the

experiment, the wing supports are shielded by strut fairings, known as the

windshields, to preserve smooth streamline, and prevent excessive tare forces acting

directly on the support systems. The Pitch strut is connected to the rear section of the

fuselage. It is installed on the pitch beam which is adjustable in vertical manner to vary the angles of attack of the model.
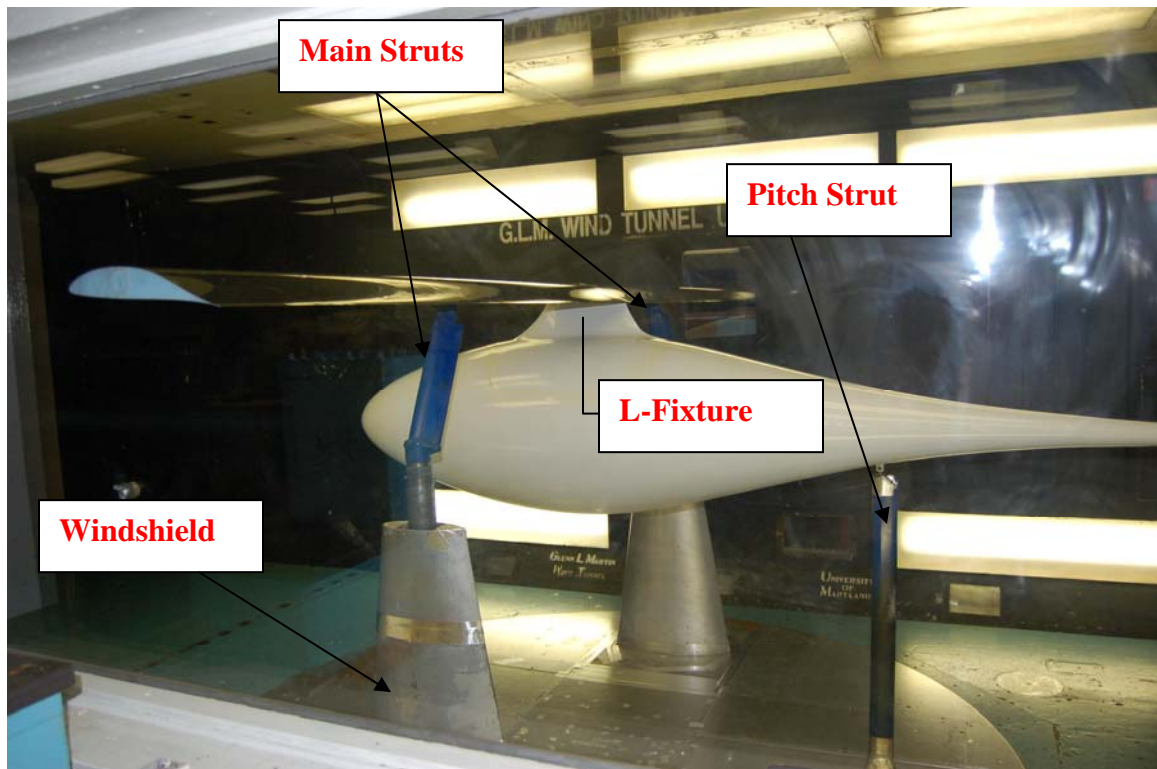
Figure 13: Wing-fuselage configuration 3 inside the test section prior to the wind tunnel run.

The L-fixture connects the middle section of the wing through the fuselage. The height of the wing relative to the fuselage is adjusted by varying the height of the L-fixture. The wing is practically held fixed in the wind tunnel test section by the two main struts for data runs. In the experimental set up, the fuselage height is adjusted rather than the wing for the various configurations. It is lowered by adjusting the L-fixture as to increase the distance between wing and fuselage. The pitch strut is higher or lower to increase or decrease pitch angle of the models. This setup is used by all the data runs and aerodynamic tare runs.

3.2.2 Experimental Procedures

3.2.2.1 Aerodynamic Tare

Prior to the actual data runs, aerodynamic tare runs must be performed to identify

forces on exposed parts of the support system which are referred to as "tare". Forces

due to aerodynamic interference of the support system on the model were not

evaluated in this experiment since the hardware to do those measurements was not

available.

In order to obtain tare of the support system it is necessary to have an alternative

way of holding the model in place in the presence of the primary support system, but

not in contact with the primary support system. This is accomplished in the present

experiment by hanging the model from the ceiling as indicated by Figure 14.

The main struts and pitch strut are first tested in combination for each height of

the pitch beam for 5 model configurations with variation of angle of attack from -10

to 5 degrees. This test is required the wetted surface of the exposed part of the pitch

strut changes with angle of attacks and with the fuselage height as it is adjusted for

the different configurations. The main struts, on the other hand, are fixed to the floor.

These aerodynamic tares are only run at 90 MPH airspeed because, the differences in

force coefficients at different airspeeds used in this experiment are assumed

insignificant. Data from the tare run is will be used to subtract from full model data

runs to obtain forces on the model.

Aerodynamic drag tare tests on individual supports were also performed to

study aerodynamic forces for each individual support components. Furthermore, the

main struts and wings were tested together with out the fuselage. Cylinder is used to replace the wing in order to test supports all together as shown in Figure 15.

Second aerodynamic interference testing is the evaluation of tare drag combining with the effect from model setting. The test uses wing-fuselage configuration 3 with zero degree pitch. The purpose is to study the aerodynamic interference between the model and the supports. The process is similar to the "image system", but without having the actual image supports. The model is setup by attaching the model, wing and fuselage, on the tunnel roof using an aluminum plate holding it through wing and fuselage.
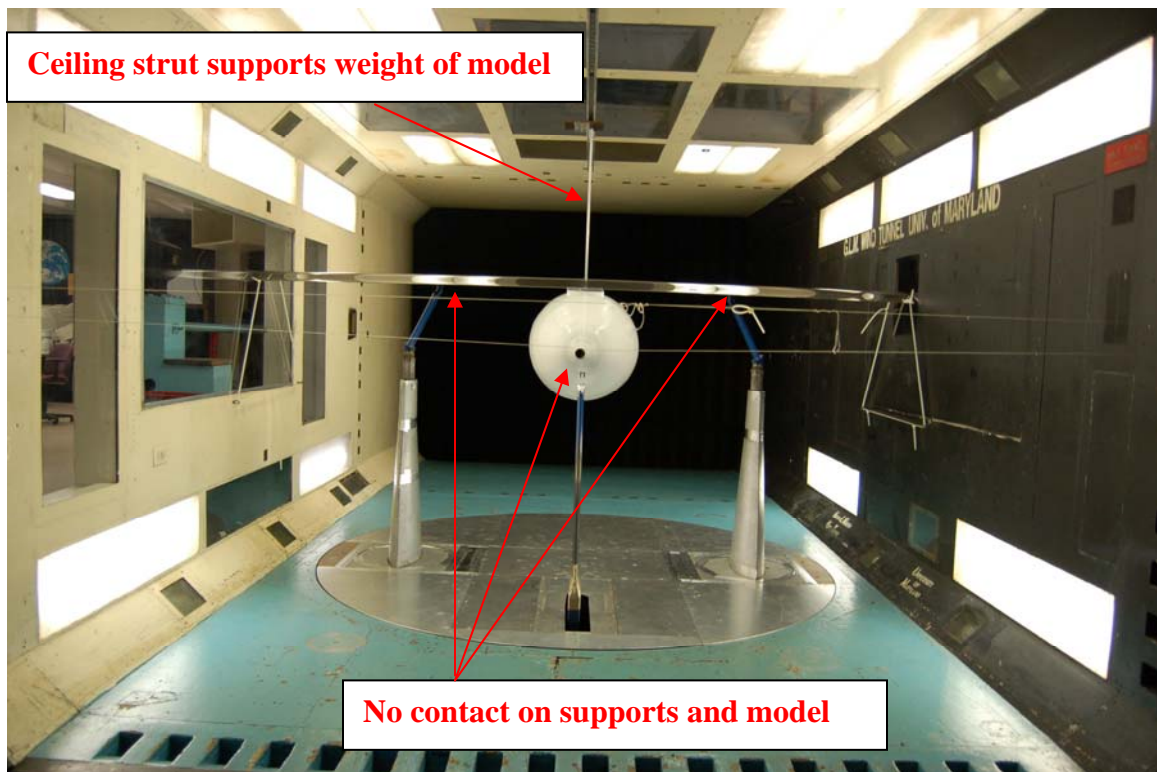
Figure 14: Model set up of Wing-fuselage configuration 3 for aerodynamic interference study.

The weight of the model is entirely carried by the aluminum plate. Main struts and pitch strut are placed at the exactly the same positions as the actual testing. Wings

are strapped at the wall to prevent the wing from moving under load. The wing and fuselage will be nearly touching the struts, yet without actual contact. The aerodynamic force measured is only from the main struts and pitch struts in the presence of the model. These forces included the interference of the model on the struts.
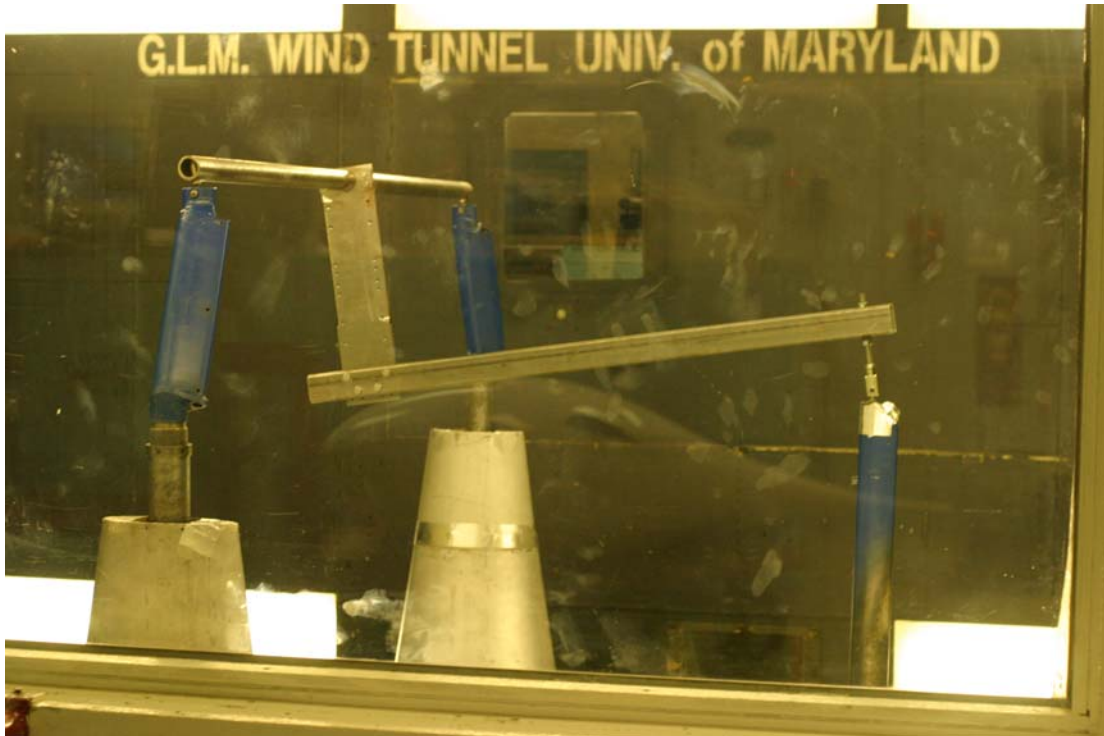
Figure 15: Aerodynamic tare tests for forces acted on supports. Cylinder is used to hold all the supports together

3.2.2.2 Aerodynamics Test of Wing Alone and Full configuration models

Having done the aerodynamic tare measurements; the aerodynamic force measurements on wing and full wing-body combinations were then performed. The variables of this section of the experiments are models, airspeeds, and pitch angles. The strategic plan was to test one model at a time for 3 airspeeds, with variation of pitch angles for each airspeeds, as specified in table 1. Wing and five models were

tested in numerical orders starting with wing. Experiment runs at 3 airspeeds; 80

MPH, 90 MPH, and 100 MPH. Table 1 gives the test routine planned and followed.

Table 1: Schedule and plan for wind-tunnel test for the experiment

Run #	Run Types	Speed (MPH)	Pitch	Purpose
1-3	M+W+L+P	80, 90, 100	A	Test on wing and supports
4	M+C+L+P	80	A	Tare on all supports
5	M+P conf 1	90	B	Tare on main and pitch struts for W/F 1
6	M+P conf 2	90	B	Tare on main and pitch struts for W/F 2
7	M+P conf 3	90	B	Tare on main and pitch struts for W/F 3
8	M+P conf 4	90	B	Tare on main and pitch struts for W/F 4
9	M+P conf 5	90	B	Tare on main and pitch struts for W/F 5
10-12	M	80, 90, 100	N/A	Tare of main struts only
13-15	M+C	80, 90, 100	N/A	Tare of main struts and a cylinder
16-18	M+W+F+P conf1	80, 90, 100	A	Test on full model W/F 1
19-21	M+W+F+P conf2	80, 90, 100	A	Test on full model W/F 2
22-24	M+W+F+P conf3	80, 90, 100	A	Test on full model W/F 3
25-27	M+W+F+P conf4	80, 90, 100	A	Test on full model W/F 4
28-30	M+W+F+P conf5	80, 90, 100	A	Test on full model W/F 5
31-33	M+W+F+P conf3	80, 90, 100	C	Test on interference drag W/F 3

Pitch Angles index
A = -10. -9, -8, -7, -6, -5, -4, -3, -2, -1.5, -1, -0.6, -0.2, 0, 0.2, 0.4, 0.6, 1, 1.5, 2, 3, 4, 5 degrees
B = -10, -8, -6, -4, -2, 0, 2, 4, 6 degrees
C = 0 degrees

Abbreviation index

M = Main Struts,   W = Wing,   Conf = Configuration

P = Pitch Strut,   F = Fuselage

C = Cylinder,   L = L-fixture Strut

Experimental conditions inside the test section are as described in table 2.

Temperatures and pressures used to calculate speed, dynamic pressure, and density

are measured simultaneously for every data point taken. The values in Table 1 are

representative. Air density, temperature, and atmospheric pressure remain

approximately the same for all airspeed. This information will also be used to define

the physical condition for the simulations.

Airspeed	Dynamic Pressure, (psf)	Density (lb/ft^3)	Temperature (F)	Atmospheric Pressure (psi)
80 MPH	16.35	0.002265	80	14.69
90 MPH	20.7	0.002266	81	14.69
100 MPH	25.73	0.002255	82	14.69

Table 2: Experiment conditions at three airspeeds; 80MPH, 90MPH, and 100MPH
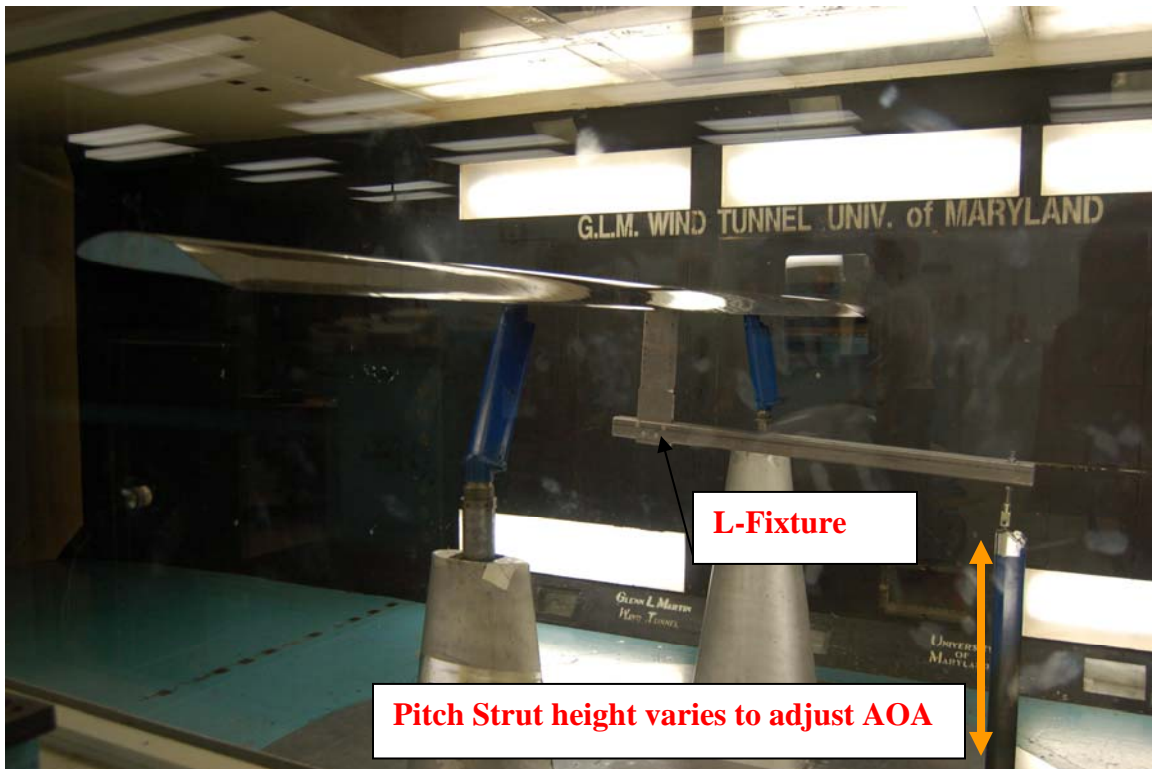
Figure 16: Aerodynamic force measurements of Orion wing with variation of angles of attack

The schematic setup of wing aerodynamic force measurements is illustrated in figure 16. The main supports held the wing in place and were connected to the external balance of the wind tunnel. The pitch struts were used to adjust pitch angles which had the L-fixture served as the linkage. The complete wing-fuselage configurations 1 through 5 are tested individually after the wing. The set up of the full configuration is similar to the wing test; expect that the L-fixture is assembled inside the fuselage, in which it is not exposed to airstreams except for configuration 5. Both wing and wing-fuselage models were tested individually at three airspeeds and pitch angles variations at zero yaw and zero roll angles.

The pitch angle increment is more frequent near stall region between -1 to 1 degree pitch angles. Angles calibrations were done to maintain accuracy of pitch angles. In some cases, illustrated in Figure 17, aluminum tapes are used to shield the gaps between parts if the gaps are large enough to cause alteration in the results. The repeated runs are encouraged if necessary.
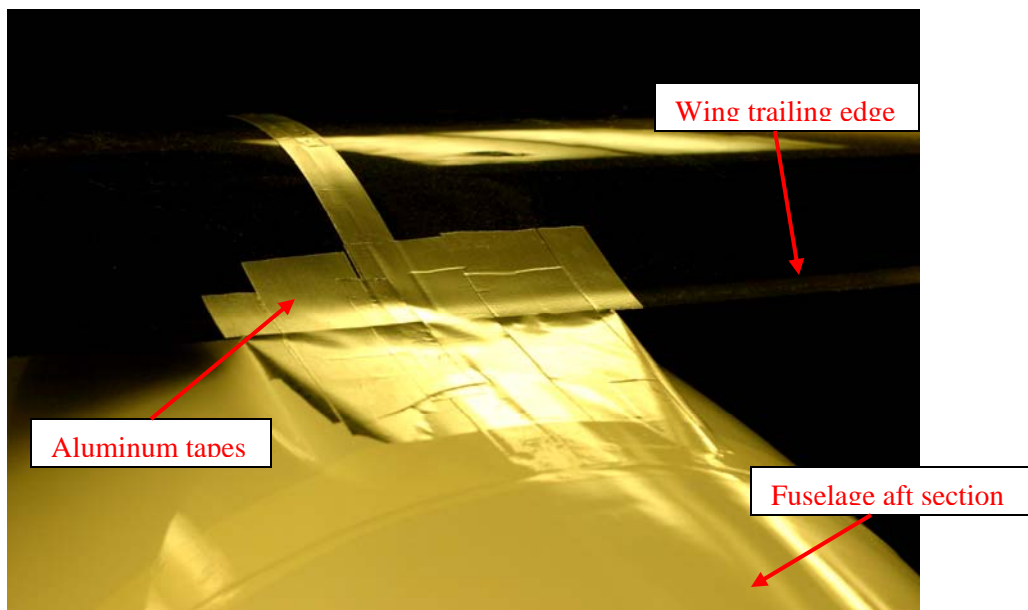
Figure 17: Aluminum tapes were applied on gaps of the models to help eliminate possibility of flow interuptions or force alterations caused by these gaps

Chapter 4: Experimental Results and Discussion

4.1 Experimental Results

4.1.1 Tare Measurements

As discussed in the chapter 3, aerodynamic tares were performed to identify

forces on exposed parts of the support systems, which are composed of main struts

(M), pitch strut (P), cylinder (C), L-fixture (L). The results of aerodynamic tares,

primarily on drag forces, are used to determine direct forces acted on the models

alone. The tare experiments are divided into 5 categories as described in table 3.

Category	Configuration	Speeds (MPH)	Pitch (deg)	Comments
1	M+P	90	B	Interpolate forces for other angles
2	M	80,90,100	N/A	Allow direct force on P and C
3	M+C	80,90,100	N/A	Preparation to obtain direct force on L
4	M+C+L+P	80,90,100	A	Allow direct force on L
5	M+W+F3+P	80,90,100	C	Interference force measurements

Pitch Angles Index
A = -10. -9, -8, -7, -6, -5, -4, -3, -2, -1.5, -1, -0.6, -0.2, 0, 0.2, 0.4, 0.6, 1, 1.5, 2, 3, 4, 5 degrees
B = -10, -8, -6, -4, -2, 0, 2, 4, 6 degrees
C = 0 degrees

Table 3: Aerodynamic tares test schedule summary

4.1.1.1 Aerodynamic Tare of main strut and pitch strut without presence of the model

Tares for the main struts and pitch strut were obtained both individually and in

combination. Tare runs were done at only one airspeed of 90 mph, because the

variation of tare force coefficient within the test speeds range is not significant. The

pitch strut is initially set up for each model configuration so that the angle of attack of

the reference line is zero. During the test, pitch angle was varied from -10 to +5 degrees.

Tare drag of MainStrut and Pitch Strut
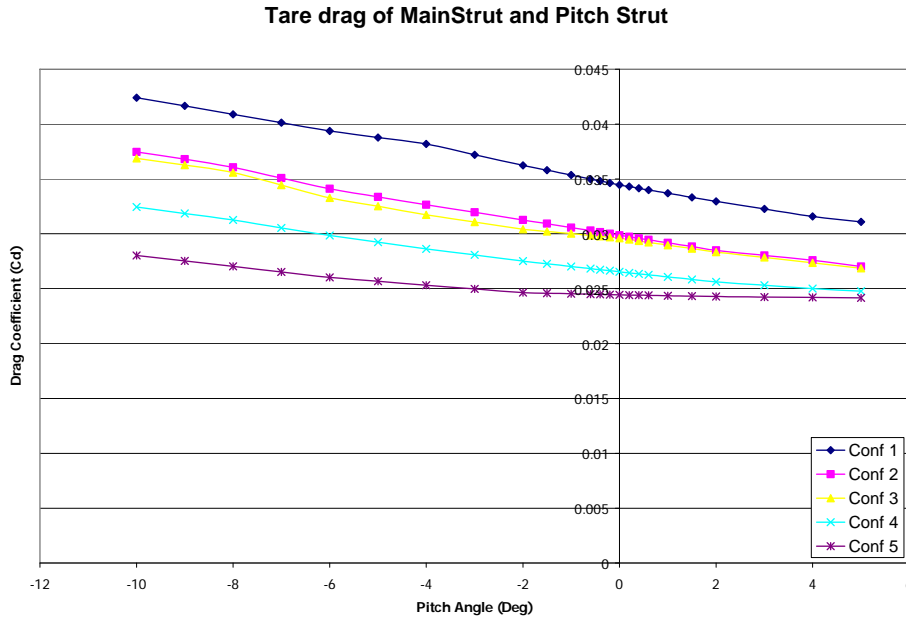
Figure 18: Drag Coefficient of Main Struts and Pitch Strut tested at 90 MPH at all angles of attack

According to figure 18, the result shows that supports for wing-fuselage configuration 1 introduce the highest tare drag. This is because more of the pitch strut is exposed to airstreams in comparison with other configurations. On the other hand, the configuration 5 has pitch strut at the lowest positions with a smaller exposure of the pitch strut to the airstreams, thus drag is less than others. The wing-fuselage configurations 2 and 3 exhibits approximately similar results, because their wing heights are only slightly different. The pitch strut rises as pitch angle decreases thereby exposing more of the strut to the airstreams.

32

4.1.1.2 Tare of Main Struts without presence of the model

The purpose of aerodynamic tare of the main struts alone is to obtain direct force values on individual support components. Data can be also used to identify true drag value on a clean model by using it to subtract off of total drag of full wing-fuselage tests.

M		
Airspeed	**CL**	**CD**
80 MPH	0.005364	0.022218
90 MPH	0.005809	0.0215
100 MPH	0.006182	0.021155

Table 4: Result of lift and drag force coefficients from aerodynamic tares of main strut alone

According to table 4, drag coefficients of M decreases as airspeeds increase, which is opposite to their lift coefficients. Lift forces are considered insignificant since it is very small relative to the predicted values described in chapter 3. Thus, it would have very little effects on lift generated by the model. On the other hand, drag forces are substantial and it affects largely on the total drag. Therefore, it needs to be accounted in the drag force calculation of the model. This shows clear comparison of lift and drag forces of the support systems, and how drag force is tremendously more significant than lift to the direct drag calculation on the model.

4.1.1.3 Tare of Main Struts and cylinder without presence of the models

Cylinder is included in the tare measurements in order to replace the wing, which makes it possible to measure forces on L-fixture and other support components. It was placed a cylinder bar across the main struts.

M+C		
Airspeed	**CL**	**CD**
80 MPH	0.007564	0.087455
90 MPH	0.008027	0.087409
100 MPH	0.008418	0.087345

Table 5: Result of lift and drag force coefficients from aerodynamic tares of main struts plus cylinder without presence of the model

The measured result of main struts with cylinder is similar to the result of the main strut alone. The pitch angles variations do not alter this measurement. Table 5 shows that drag coefficient arises four times with presence of the cylinder. Lift coefficients, on the other hand, are not affected by much from adding cylinder, and provide insignificant influences on total lift of the clean models. Thus, data will be only for drag to subtract off of total drag of full wing-fuselage test.

4.1.1.4 Tare of Main Struts + cylinder + L-link + pitch strut

It is useful to realize force dedications of each support pieces on the total forces. The tare results of MLPC allows direct force calculation on the L-fixture after having known the values of M, M+P, and M+C, as L = (M+C+L+P) – (M+C) – (M+P) – (M). The result of MLPC is shown in figure 19. Again, little lift force is generated, thus little will affect the model's total lift force.

CL vs. CD [MLPC]
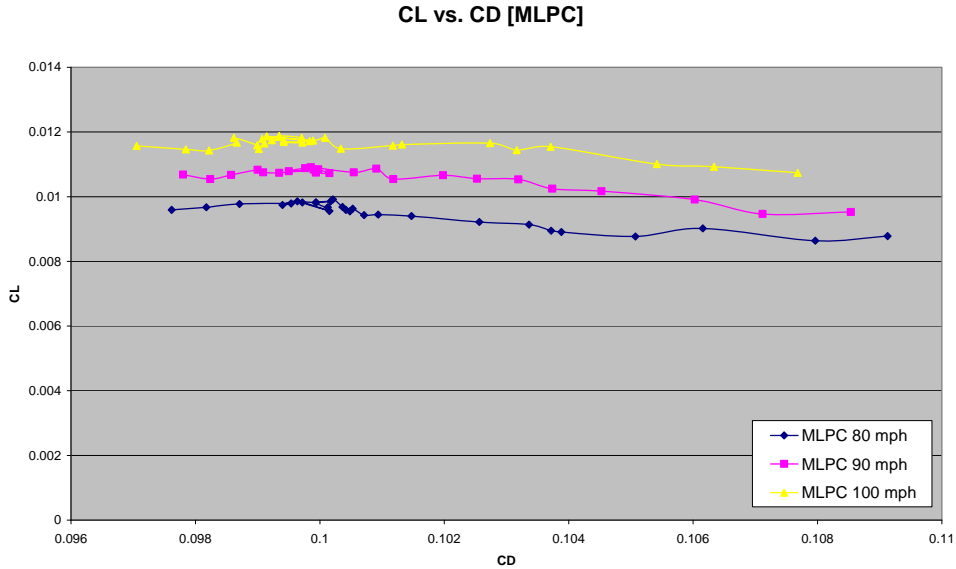
Figure 19: Aerodynamic tare of M+L+P+C featuring Lift vs. Drag plot

As pitch angle increases, drag coefficients decrease because the exposed part of the pitch strut is less. Lift coefficients, on the other hand, stay nearly constant throughout pitch angle sweeps. Lift force also seems to have very little effects on the expected total force in comparison with drag force.

4.1.1.5 Tare of the Main Struts + Pitch Strut in presence of model

Recall that the model is supported from the wind tunnel ceiling for the tare run; therefore the aerodynamic forces are measured only on main struts, pitch struts in the presence of the model. This data includes the interference of the model on the struts. The wind tunnel data displays surprising results. The drag force on the struts in the presence of the model is slightly lower than drag force of the supports alone. In other words, [M+P] > [M+P+interference drag].

Speed	CD Struts (M+P) + Interference	CD Struts (M+P)
80	0.028691	N/A
90	0.028327	0.029609
100	0.027664	N/A

Table 6: Drag Coefficient of main struts and pitch strut from Interference drag study

Look now at a more specific result. At zero degrees angle of attack, the strut tare drag coefficient in the presence of configuration 3 is 0.028327, whereas the tare drag coefficient of the main struts plus pitch struts without the model is 0.029609. In other words, CD [M+P = 0.029609] > CD[M+P+interference = 0.028327].

The assumption for this phenomenon is that there is velocity deficit on both supports in the presence of the model. Since the fuselage and wing are located upwind of both main struts and pitch strut, it appears that the flow field in the presence of the model has a reduced dynamic pressure on average over the regions of the struts. This causes the amount of drag from interference tests to be less than those of the supports alone.

4.1.2 Aerodynamic Performance of the Wing

Figure 20 shows the wing performance parameters, CL and CL/CD, versus pitch angles. Figure 21 shows the drag polar, lift coefficient against drag coefficient for the wing. The lift coefficient value can be obtained directly from the data run as no tare correction is made to the lift. On the other hand, value of drag coefficient needs to be corrected based on the tare runs.

Wing drag = (M+L+P+W) – (M+P) – [(M+C+L+P) – (M+C) – (M+P) + M]

36
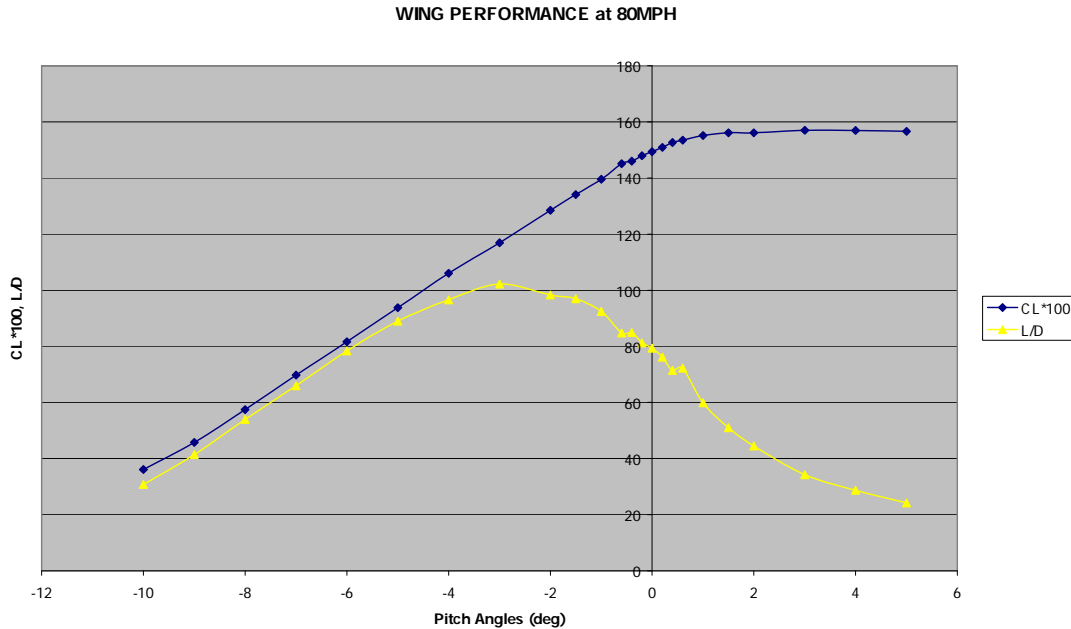
Figure 20: Measured Wing Performance Parameters, CL*100 and CL/CD

Recall figure 6 and figure 8, the wing performance from the experiment is much lower than the simulated airfoil root performance. The maximum lift coefficient of the wing is 1.57 at 3 degree pitch angle, in comparison with simulated airfoil root maximum lift coefficient of 1.8. Its maximum value of measured lift to drag ratio is 102 compared to other simulated value of 164 for the infinite span case. The difference is partly due to real chord-wise differences in the 2 cases and to the fact that the experimental case is not 2 dimensional but has hap flow at the wing tips. Nevertheless, the wing performance shows great potential of maintaining laminar flow of over the wing with considerably high lift and low drag coefficient. The maximum lift is reached at a pitch angle of approximately 2 degrees with no significant drop out to +5 degrees.

The measured wing lift polar, figure 21, shows the minimum drag coefficient value as 0.0104 at lift coefficient of 0.8162. Comparing the measured wing properties

37

to the simulated airfoil performance shows the lift values at the minimum drag point

to be approximately the same, but measured drag value is higher by almost 100%.

Wing CL vs. CD at 80 MPH
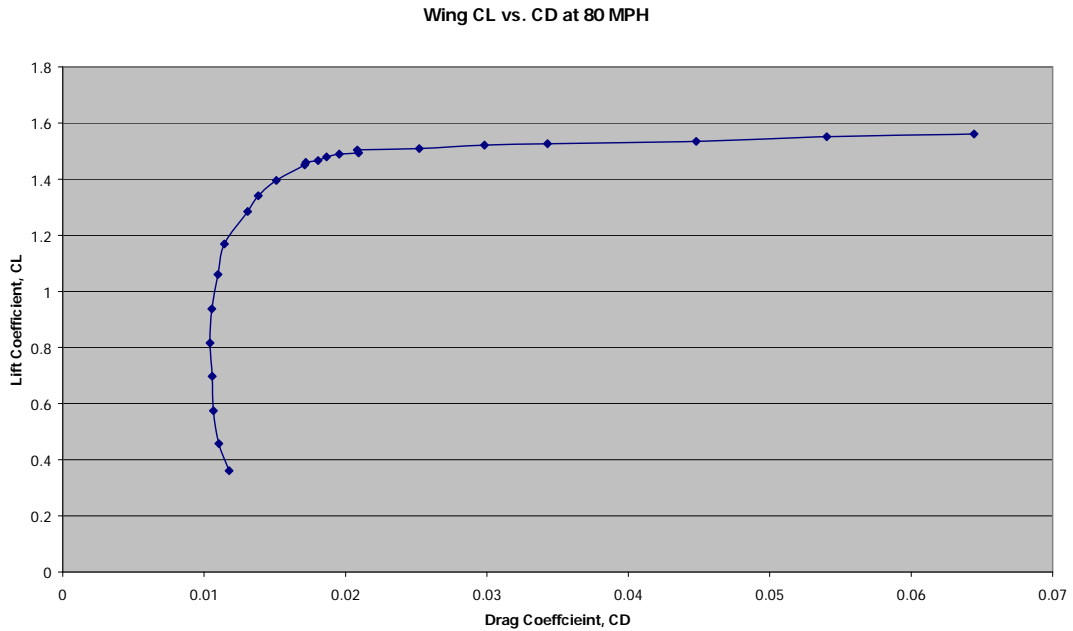
Figure 21: Measured Wing Polar Plot lift Coefficient vs. Drag Coefficient

4.1.3 Aerodynamic results of the wing-fuselage configurations: Lift Coefficient vs. Drag Coefficient at different airspeeds

Figure 22 shows polar curves, lift coefficient (C_L) versus drag coefficient

(C_D), for the wing-fuselage configurations and Figure 23 is a close-up for part of the

polar plot at airspeed 80 mph.
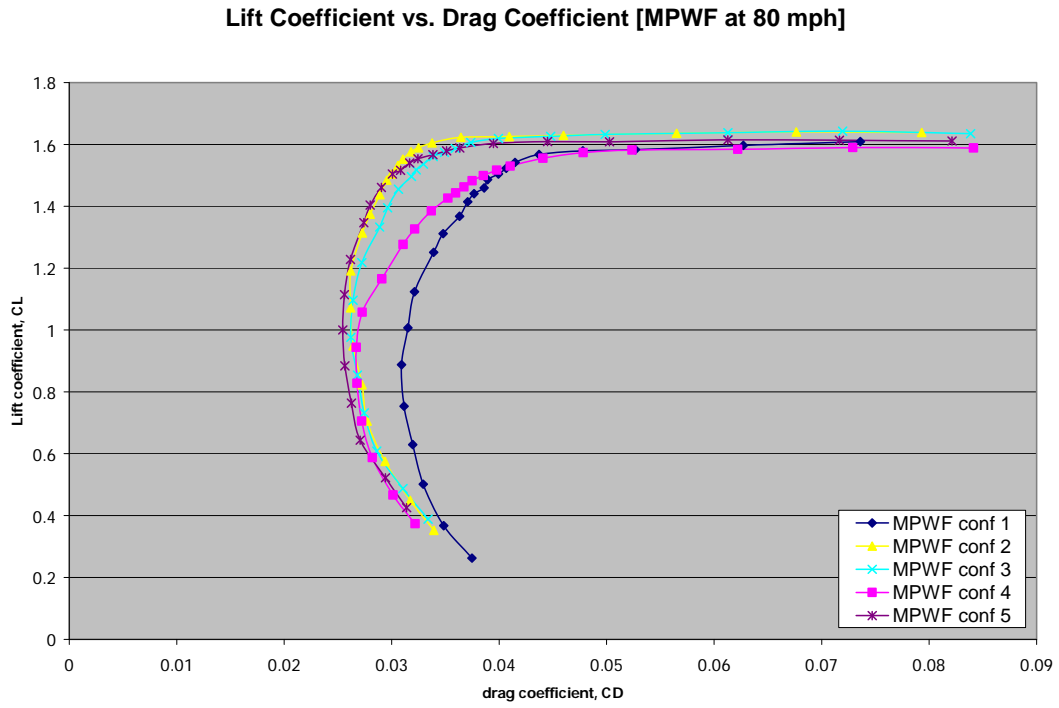
Figure 22: Result from experiment CL vs. CD in comparison of all five configurations at80 MPH
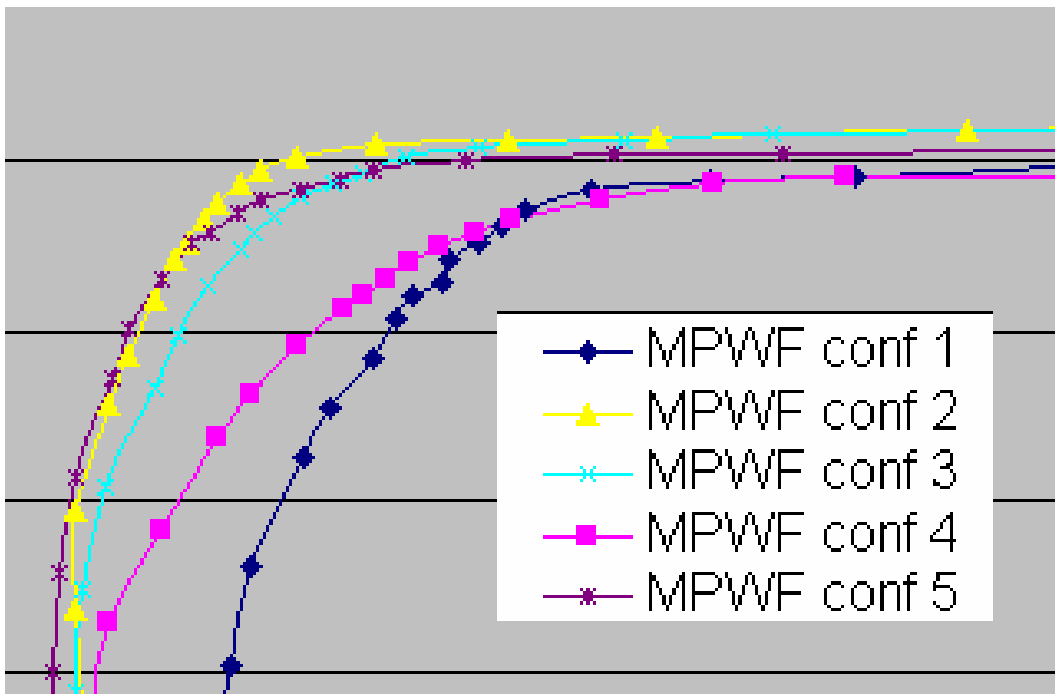
Figure 23: Zoom-in of figure 22 around stall region

Figure 22 shows the polar curve from the wind tunnel experiment for the five configurations at three airspeeds; 80 MPH. The data shows that the configuration 1 has the highest drag with lower lift in comparison with others. Wing-fuselage configuration 1, mid-wing model clearly has the poorest performance of all five configurations in this aspect. According to figure 22, the configuration 5 has lowest drag values along negative pitch angles. At higher pitch angle, its lift coefficients drop slightly below the configuration 2 and configuration 3. Looking very closely, the configuration 2 and configuration 3 tend to operate better at higher angle of attack than others. The configuration 2 specifically performs better than the configuration 3 near the stall region, where its drag coefficient is lower, and lift coefficient is higher.

The polar curves show the similar characteristics for the following airspeeds, 90 and 100 mph, which are plotted in figure 24 and 25. At these higher airspeeds, the performance of configuration 2 surpasses the performance of the configuration 3 and 5 at high angle of attacks. At higher airspeed, drag coefficient tend to be slightly lower for all models. This implies that higher airspeeds tend to delay separation. The maximum L/D increases by some degree. Airspeed increment may have helped attaching the flow throughout the body encouraging a reduction in areas of separated flow and thus reducing drag and increasing lift.

Lift Coefficient vs. Drag Coefficient [MPWF at 90 mph]
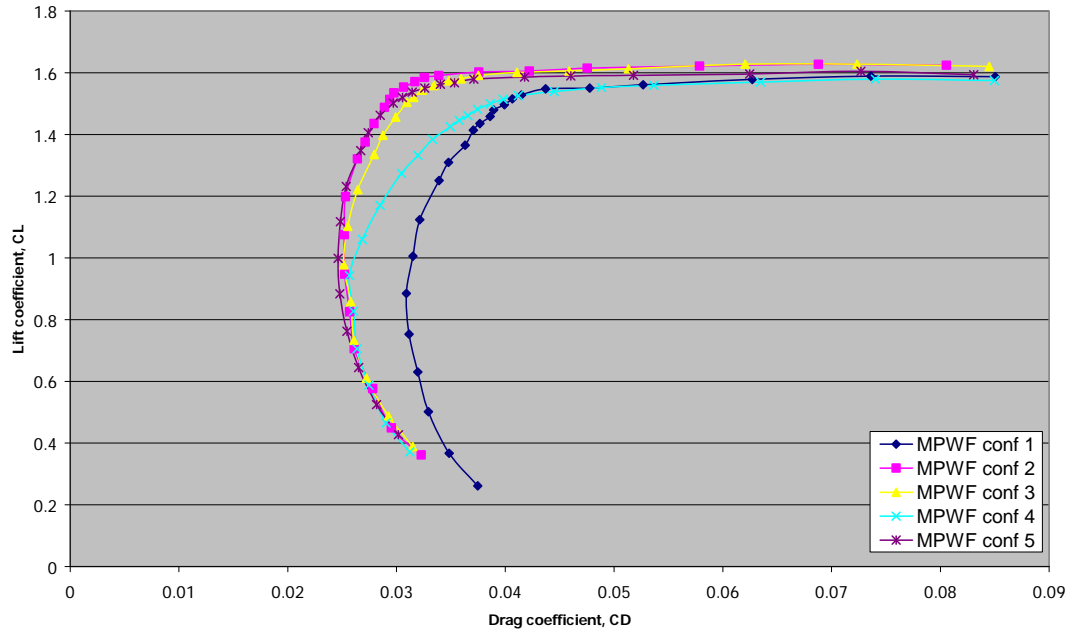
Figure 24: Result from experiment C$_L$ vs. C$_D$ in comparison of all five configurations at 90 MPH

Lift Coefficient vs. Drag Coefficient [MPWF at 100 mph]
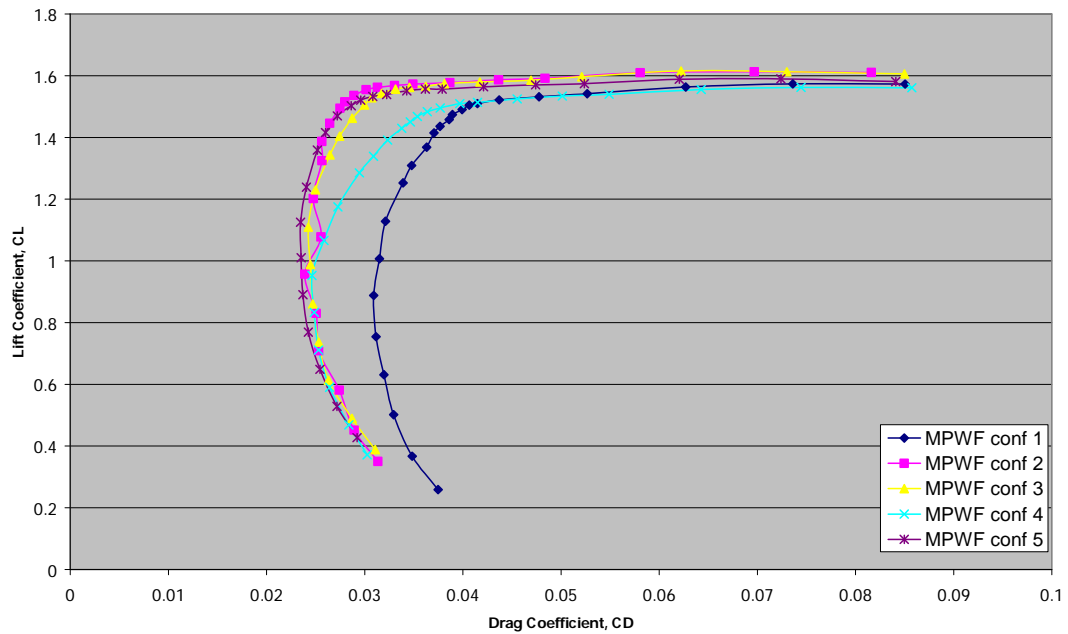
Figure 25: Result from experiment C$_L$ vs. C$_D$ in comparison of all five configurations at 100 MPH

Overall, the aerodynamic performance of configurations 2, 3 and 5 are considered preferable to configuration 1 and 4. Configuration 3 tends to perform best after stall region. Configuration 2 performs better near stall region. Nevertheless, configuration 5 may yield overall best results because it performs best at operating range of aircraft.

4.1.4 Aerodynamic results of the wing-fuselage configurations: Lift Coefficient vs. Pitch Angles at different airspeeds

Figure 26, 27, and 28 represent lift coefficient at different angle of attack and airspeed. Maximum lift and stall regions can be observed from this graphical display.

Lift Coefficient vs. pitch angle [MPWF at 80 mph]
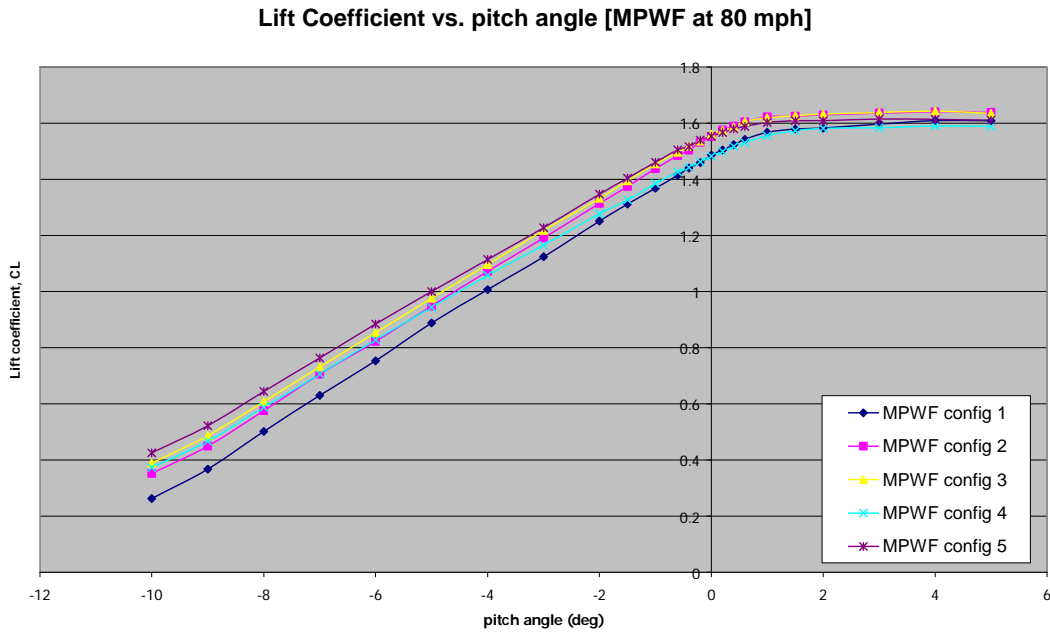
Figure 26: Result from experiment C_L vs. Pitch Angles in comparison of all five configurations at 80 MPH

Figure 26 shows lift coefficient versus pitch for all model configurations comparison at 80 MPH airspeed. The configurations 2 and 3 exceed performance

42

of others after or near stall region. On the other hand, at the primary operating region (lower pitch angle), configuration 5 has the best performance. This interpretation is confirmed with the polar plot in the section above.

Table 7 shows the maximum lift coefficient obtained from the wind tunnel experiment corresponding to the comparison of all models at 80 MPH. The maximum lift of all configurations occurs at the pitch angles range of 3-4 degrees. Larger pitch angles initiate stall behavior on aircraft model. According to the table 4, it is clear that configuration 3 has highest maximum lift coefficient, followed by configuration 2, 5, 1, and 4. Nevertheless, operating range lift coefficients indicates that configuration 5 is best in its region.

Configuration	MAX C_L	Pitch Angle
1	1.6091	4 deg
2	1.6405	4 deg
3	1.6425	4 deg
4	1.5900	4 deg
5	1.6148	3 deg

Table 7: Maximum Lift Coefficient comparison of five configurations

Similarly to those of 80 MPH airspeed, the results show that the model configuration 5 produces greater amount of lift at the lower (negative) pitch angles than others. However, as pitch angles progress toward the positive side, configuration 2 and 3 takes the lead on generating lift force, where configuration 2 has slightly higher lift coefficient produce. This is different from the result at 80 MPH airspeed. It may imply that the configuration 2 performs slightly better than configuration 3 at higher speed.

Lift Coefficient vs. pitch angle [MPWF at 90 mph]
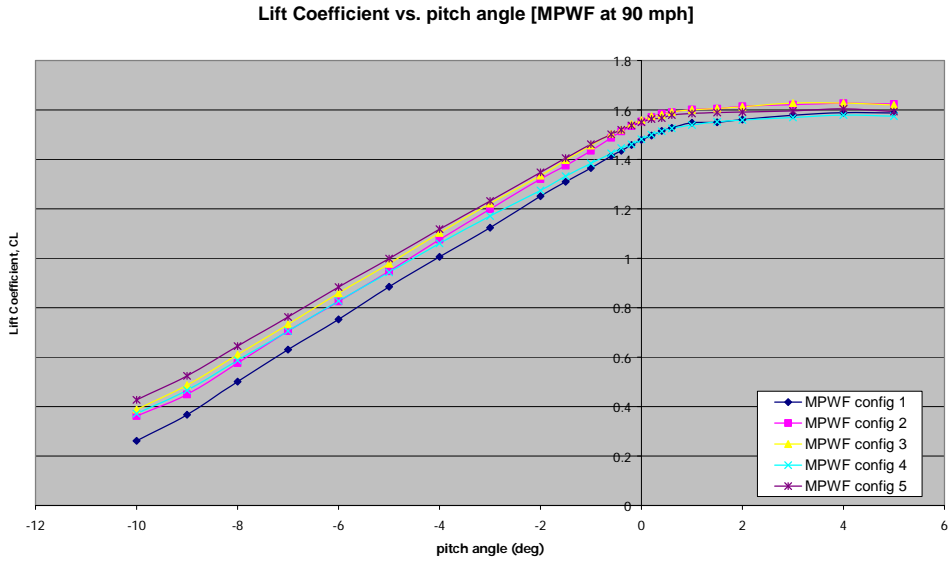
Figure 27: Result from experiment C$_L$ vs. Pitch Angles in comparison of all five configurations at 90 MPH

Higher airspeed allows higher lift coefficient at lower angle of attacks, but at stall regions lift coefficients decrease as airspeed increases. The interchange point is at initial wing stall angles, or around 0 degree pitch.

Lift Coefficient vs. pitch angle [MPWF at 100 mph]
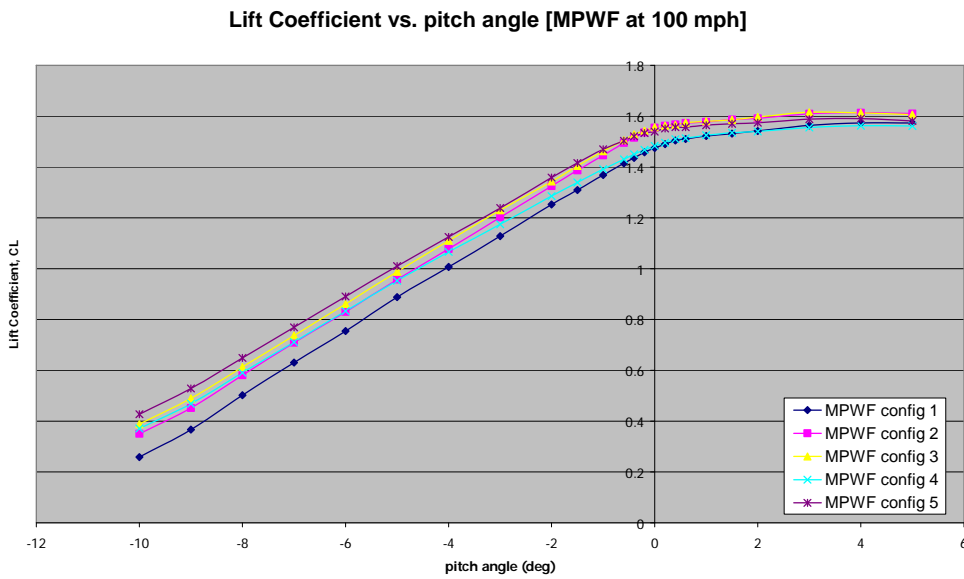
Figure 28: Result from experiment C$_L$ vs. Pitch Angles in comparison of all five configurations at 100 MPH

44

Overall result from C_L vs. pitch angles shows model configuration 5 perform best at lower angle of attacks or at operating range, but slightly worse than configuration 2 and 3 as angle of attacks increases to higher values.

4.1.5 Aerodynamic results of the wing-fuselage configurations: Drag Coefficient vs. Pitch Angles at different airspeeds

Figure 29, 30, and 31 represent drag coefficient at different angles of attack and airspeed. Drag comparison of five models can be observed from this graphical display.

Drag Coefficient vs. pitch angle [MPWF at 80 mph]
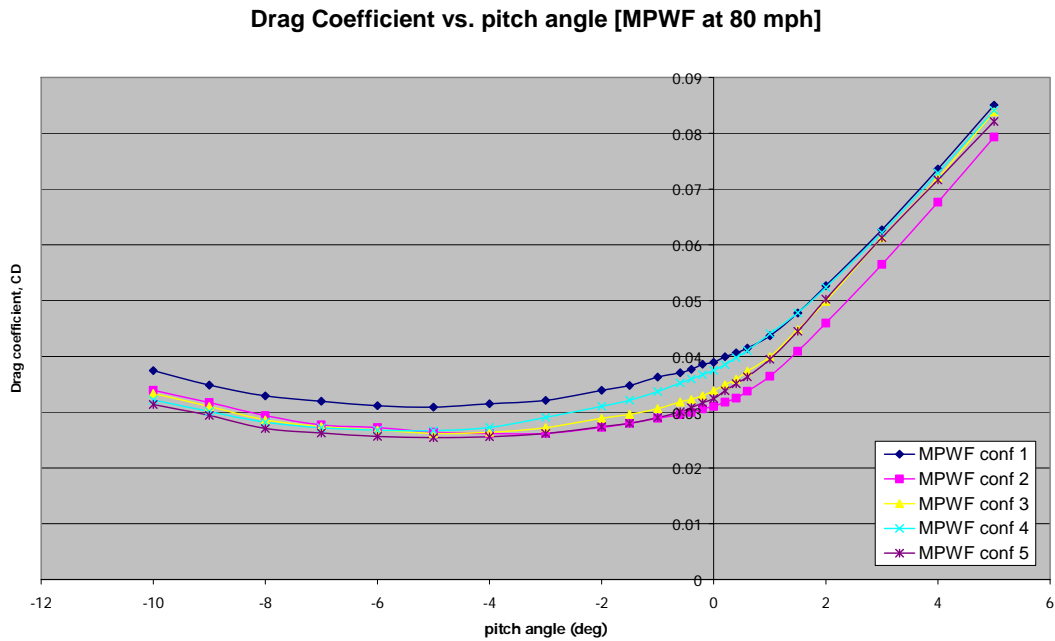
Figure 29: Results of drag Coefficient in comparison of all five configurations at 80 MPH

The results of drag coefficient from the experiment clearly show that configuration 1 has highest drag at both negative and positive regions. Configuration 4 has subtle amount of drag generated at low negative pitch angles, but its drag starts rising continuously at around -4 degrees pitch angles with higher rates than other models. At positive pitch regions, configuration 4 produces drag nearly as high as the

configuration 1. Configuration 5, on the other hand, has the smallest minimum drag, as shown in table 10, plus it produces the least amount of drag at negative pitch regions. However, at positive pitch, near or passing stall regions; configuration 2 is able to outperform the configuration 5 by having its drag reduced for great amount. Configuration 3 is in a mediocre position where its drag is not the highest nor the lowest comparing to other configurations.

Drag Coefficient vs. pitch angle [MPWF at 90 mph]
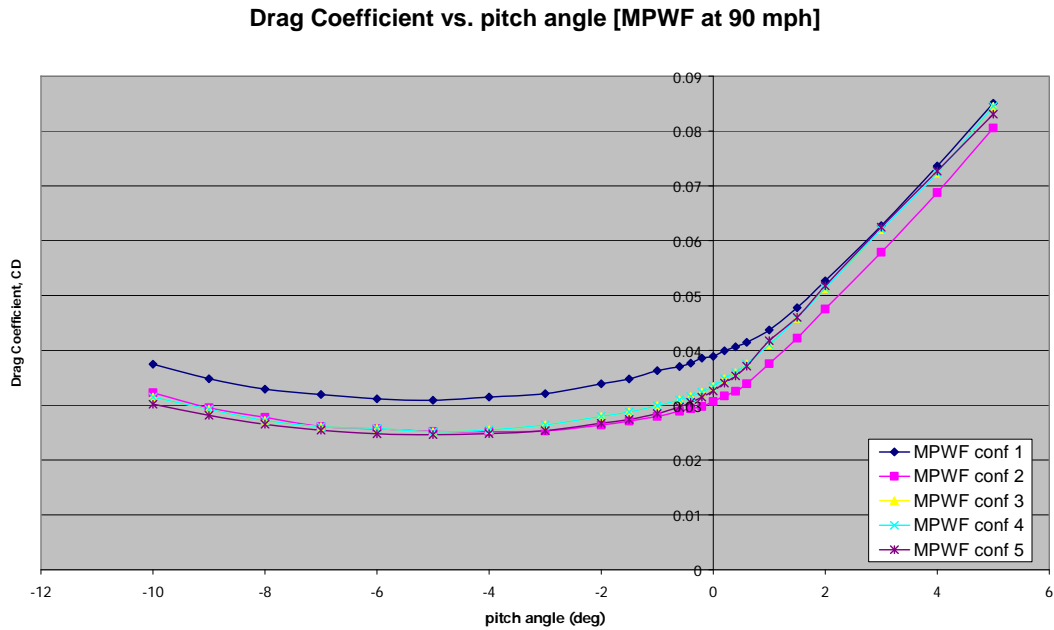
Figure 30: Results of drag Coefficient in comparison of all five configurations at 90 MPH

Slight changes occur as airspeed increases. Figure 30 and 31 shows drag coefficients in comparison of five models at airspeed 90 mph and 100 mph. The results illustrate that airspeed increments reduce drag at negative pitch regions, and increasing it at positive pitch regions. The transition point occurs at approximately zero degrees pitch angle. At 100 mph, configuration 4 drag rises so high that it becomes even larger than drag of configuration 1 at positive pitch angles. Overall

46

airspeed increment does seem to benefit all models at negative pitch, or primary
operating regions.
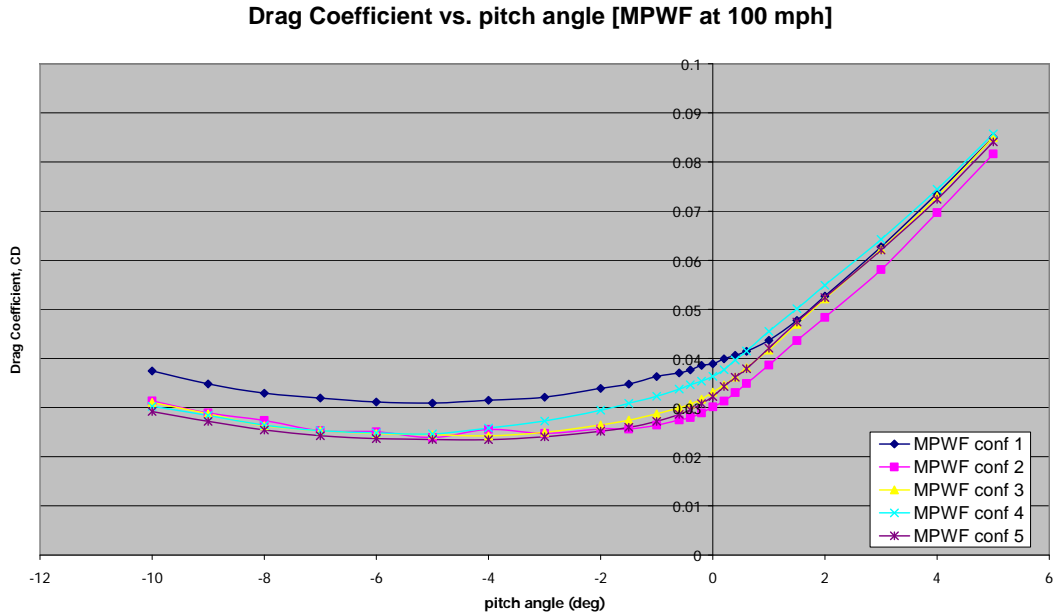
Figure 31: Results of drag Coefficient in comparison of all five configurations at 100 MPH

4.1.6 Aerodynamic results of the wing-fuselage configurations: Lift to Drag Ratio (C_L/C_D) Analysis

Lift to Drag Ratio is a primary characteristic to determine performance of aircraft. Higher C_L/C_D generally indicates better aerodynamic performance, and lower indicates worse. Often time even when a model generates higher lift force than the others does not necessarily mean that it performs better as long as drag value is higher as lift increases. That is drag due to lift, or induced drag may increase as lift increases. Variation depends on geometry of models

Figure 32 is experimental result of C_L/C_D VS. Pitch angles for the five configurations at 80 MPH airspeed. It shows that C_L/C_D progresses in a linear fashion

with similar slopes until near the stall region at approximately before zero degree

pitch angle where it progressively deteriorates. It is clear than the configuration 5's

performance is more superior to the others at negative pitch angles region.

Nevertheless, at higher pitch angles especially near or passing stall regions,

configuration 2 has higher performance than the rest including configuration 5.

Lift/Drag Ratio vs. Pitch Angles
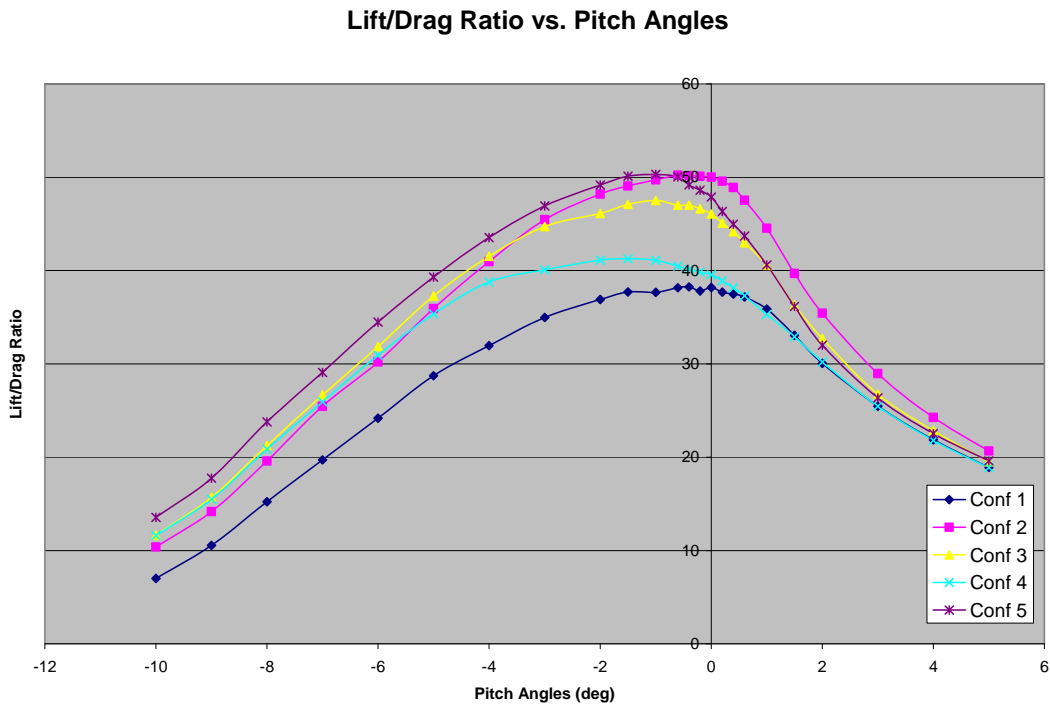
Figure 32: Result from experiment C_L/C_D vs. Pitch Angles in comparison of all five configurations at 80 MPH

Configuration	MAX C_L/C_D	Pitch Angle
1	38.16	-0.6 deg
2	50.22	-0.6 deg
3	47.54	-1 deg
4	41.26	-1.5 deg
5	50.29	-1 deg

Table 8: Maximum lift-drag ratio of five configurations at 80MPH

48

Table 8 shows the maximum C_L/C_D of five configurations. The configuration 5 has highest maximum C_L/C_D, simply slightly better than the configuration 2. Stall regions of the model 2 is delayed and shifted for better performance within positive boundary pitch angles. The configuration 1, on the other hand, is clearly shows the worst performance of all five configurations. Its maximum and average C_L/C_D is substantially lower than other configurations. Since it is not much difference in lift, the mid-wing configuration experiences a large drag increment apparently due to a higher intersection drag.

CL/CD vs. CL [MPWF 80 mph]
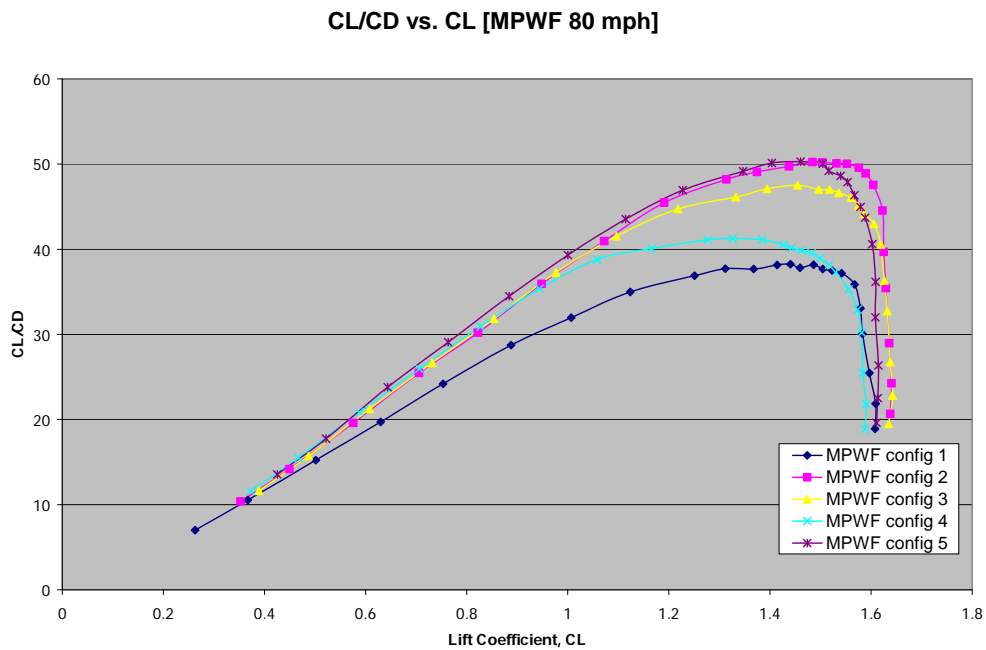
Figure 33: Result from Experiment C_L/C_D vs. C_L of all five configurations at 80 MPH

The plot of C_L/C_D vs. C_L, figure 33, is another useful plot for interpreting aerodynamic characteristics of configurations. It enhances comparisons between different models. Above is the result from the experiment at 80 MPH airspeed.

It is shown that the performance of each model is similar at lower lift

coefficient, thus lower pitch angles. As the lift coefficient progresses higher, the

configuration 2 maintains linear increments longer than other models. It is able to

generate the most lift at higher lift-drag ratio, which implies that its stall angle is

slightly higher than other models. In contrast, the configuration 1 is confirmed to

have worst performance of all five configurations. Results from higher airspeeds are

consistent with these at 80 MPH.

4.1.7 Aerodynamic results of the wing-fuselage configurations: Drag increment added to the wing alone

The previous sections treated the performance measures that included all of

the wing and fuselage configurations as though they were complete aircraft, although

the wings extended essentially to the wind tunnel walls. This introduces an

unrealistically high effective aspect ratio. An alternative means of making a

comparison is to consider the incremental drag added to the wing alone drag as a

performance criterion. If the reasonable assumption is made that the addition of the

fuselage does not change the wing-wall interaction significantly, then the drag

increment added by the fuselage for the various configurations can be taken as

representative of the addition that would be added to a wing of realistic aspect ratio.

Figure 34 shows the drag increments added to the wing alone for each of the five

configurations, all as a function of pitch

Drag Coefficient (CD) increment added to the wing alone
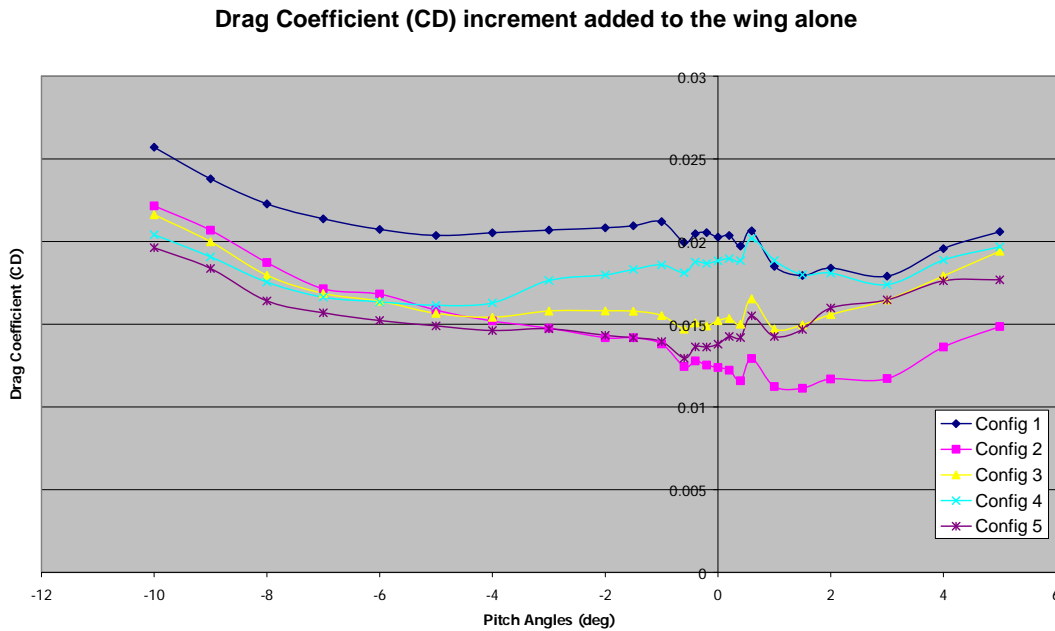
Figure 34: Drag increment added to the wing alone in comparison of five configurations at 80 mph airspeed

Figure 34 shows the drag increment is greatest at -10 degrees pitch angle for all models. The drag increment decreases for all configurations as pitch angle increases from -10 to about -5 degrees where the increments for configurations 1 and 4 turn upward, configuration 3 flattens, while configurations 2 and 5 continue to decrease out to the incipient stall region. At that point near zero pitch, the increment for configuration 5 turns upward while the increment for configuration 2 continues to decrease even into the stall region. Configuration 2 exhibits the longest decrement interval and it has overall the lowest drag increment. On the other hand, the model which generates the overall highest drag increment is configuration 1. Figure 31 further indicates that configuration 4 has its drag increment rise beginning at a lower

pitch than other models. This implies inefficiency of its wing-fuselage junction design at higher angles of attack, at which it is very prone to flow separations.

Model	Min CD increment	Pitch [deg]
Configuration 1	0.017909091	3
Configuration 2	0.011127273	1.5
Configuration 3	0.014709091	-0.6
Configuration 4	0.016154545	-6
Configuration 5	0.012954545	-0.6

Table 9: Minimum drag increment added to the wing alone in comparison with five configurations at 80 mph airspeed

Table 9 shows minimum drag increments added to the wing alone by the various configurations and the corresponding pitch angle at which this minimum occurs. Configuration 2 has the smallest minimum drag increment. Configuration 1 has the highest. Although configuration 5 does not give the absolute minimum, it performs better than configuration 2 at moderate lift regions and is equal to configuration 2 out to incipient stall pitch angles. The drag increment for configuration 5 rises considerably high after reaching the pitch angles for which lift has become flat.

4.2 Experimental Results Discussion

It may be a bit ambiguous to judge the best performing model in these comparisons. The configuration 2 and the configuration 5 have their own distinguishing characteristics. One is performing better at lower pitch angles and others at higher pitch angles. On the other hand, the mid-wing configuration 1 clearly possesses the least desirable aerodynamic characteristics. The detail discussion will review performance of all five configurations.

Table 10 shows a summary of significant results including maximum CL and minimum CD with the values of pitch and CL at which these extreme values occur. The maximum CL/CD is shown in table 8. The typical mid-wing design, configuration 1 performs overall poorest in every aspect. Its minimum drag coefficient is the highest regarding to the table 9. Having the wing located in the middle of fuselage leads to the effects of junction flows occurring directly on both wing and fuselage, encouraging stronger unstable vortices. These unstable vortices easily combined at the trailing edge of the wing creating more loss in lift and increase in drag. The mid-wing configuration also easily creates turbulent side-wash along aft fuselage. Another reason for its poor performance is assumed to be the design flaw, in which it lacks of junction fillets. This enhances the degrees of separated flow and turbulence at the wing-fuselage intersection, and therefore lower performance characteristics. There is a possibility that, if the fillets were installed, junction drag would be alleviated. The separation in front of the junction, and trailing edge would be lessened; thus leading to an increase in performance characteristics.

Configuration	MAX C_L	Pitch Angle		Configuration	MIN C_D	Pitch Angle
1	1.6091	4 deg		1	0.03091	-5 deg
2	1.6406	4 deg		2	0.02618	-4 deg
3	1.6426	4 deg		3	0.02621	-5 deg
4	1.5900	4 deg		4	0.02670	-5 deg
5	1.6148	3 deg		5	0.02544	-5 deg

Table 10: Maximum lift coefficient and minimum drag of five configurations at 80MPH

Configuration 4 shows the least amount of C_{Lmax}, and has a large amount of drag in comparison to all five configurations. It is designed to be a high wing model, quite similar to the configurations two and three. With high wing position, a longer

fairing is required to help reduce drag and separation from wing-fuselage intersection. However, this may induce an extra amount of drag on itself. The assumption is that larger gaps between wing and fuselage should have provided sufficient space to allow vortices not to strongly interact compress with one another and gives smoother flow. Yet, it may induce a more turbulent wake and spoil smooth flow on the wing and introducing even more interference drag between fuselage, wing, and fairings.

A high-wing configuration 3 displays a mediocre performance comparing to the others. As a matter of fact, it generates largest maximum lift coefficient at 4 degree pitch angle. However, it does not generate as much lift as other models at lower pitch angles. This means that its lift to drag ratio is generally low at lower pitch angles. Thus, its performance is judged less than that of configuration 2 and configuration 5. The fairing design tends to promote smooth flow and relieve separation around wing-fuselage intersection. The design of configuration 3 delays drag and stall effects at high angle of attacks. But at the same time it performs poorer at lower angle of attack. Overall, it exhibits good aerodynamic design, yet is not the best.

The wing-fuselage configuration 2 has outstanding performance near and after zero pitch angles where stalling starts to occur. Despite less lift at lower angle of attack, the configuration 2 provides impressive lift to drag ratio at higher angles of attacks where it surpasses the performance of wing-fuselage configuration 5. The amount of drag generated at higher angle attack is slightly larger than other models, but it is surprisingly able to generate sufficient amount of lift to compensate occurrence of more drag. This shows that the fairing design of configuration 2

promotes a favorable lift increment. It simply promotes good and continuous flow across the wing to encourage lift at higher angle of attack, and gives considerably smoother separation at the wing-fuselage junction. Overall, the model configuration 2 may yet perform the best at higher pitch angles, but at lower pitch angles which are an expected operating region of aircraft, it does not surpass the performance of configuration 5. Therefore, it is simply the second best in terms of aerodynamic performance.

The best aerodynamic performance, the highest wing design, wing-fuselage configuration 5, exhibits a surprisingly good aerodynamic capability. The best characteristic of configuration 5 is the outstanding performance around operating region, or negative to zero pitch angles.

Configuration 5 is designed to have the wing located very high above the fuselage with one flat plate strut as a holding structure. In terms of aerodynamics, this makes wing-fuselage junction fairly clean, because it minimizes surface area of fairings. The wide space between wing and fuselage may help reduce the drag from flow compression between wing and fuselage. This, in turn, gives configuration 5 the best aerodynamic design. However, the flaw of the design may be its structural limitations, especially to the wing. Although the experiment shows no sign of structural problems during the test runs, this design may be structurally fragile in the real flight high-lift and high wing loading, and maneuvering conditions.

Overall, according to experimental results, the aerodynamic performance of all models can be ranked from best to worse as configuration 5, 2, 3, 4, and 1.

Chapter 5: Computational Fluid Dynamics (CFD) Procedure and Methodology Applied in this Study

5.1 Aircraft Modeling

The geometry for the models used in the wind tunnel experiments were created on CATIA by the design team of Aurora Flight Sciences. The original CATIA CAD models were created solely for manufacturing purposes, in which individual parts are not attached within allowable tolerance for CFD simulation. The original files were transformed into Initial Graphics Exchange Specification (IGES) files format, a neutral data format for Computer Aid Design (CAD) systems, for appropriate modification in RHINOCEROS.

RHINOCEROS is a powerful CAD software application used, specifically in this case, to regenerate the surfaces of the model to be suitable for the CFD simulation. The seams of different individual parts are completely tied together into one piece creating a watertight model with 0.001 inch of tolerance. The modification proceeded with care to avoid any shapes and contours of aircraft models, in order to obtain an accurate representation for the geometry as tested. The size of all models remains unchanged with 1:1 full scale. An elliptical shape free-stream boundary region is generated around the aircraft model. Sufficient spacing between the aircraft model and the boundary region was chosen for appropriate meshing and free-stream simulation. Since the models have mirror symmetry relative to the x-y plane, it is possible to split the model in half in order to create a finer mesh, and save memory

during the simulation. The finished models are exported into IGES file format for the simulation in Star CCM+, a product of CD-Adapco, Inc.

5.2 Surface and Volume meshing

Meshing is a vital step for CFD simulation. Mesh is defined as geometry and space on model being solved by mathematical methods of fluid dynamics[6]. Volume mesh is composed of 3 basic mesh elements; vertices, faces, and cells. Individual cells are connected and formed within boundary region of the model to be computed in the simulation. Therefore, refinement of meshes has major effects on accuracy of the simulation results. It may be true that greater numbers of mesh cells yield better chances of obtaining more accurate results; nevertheless, other factors must be considered, such as time and computer capability. Quality and validity of mesh are also as important because it concerns to validity of results being computed at certain space.

Star CCM+ is equipped with a powerful meshing capability. The semi-automatic meshing tool allows user ease of generating both surface mesh and volume mesh. The tool allows a user to focus solely on interacting with region and boundary of model, rather than mesh elements. Meshes are to be automatically generated upon user's inputs, and are expected to be valid, and of good quality.

Surface mesh serves as starting surface for volume meshing. It is typically originated by CAD software; generally it is not of good quality, unless created and exported into mesh files. In this case, surface is created by RHINOCEROS, and is imported as IGES format into STAR CCM+. These meshes are not structured, and its quality is too poor for volume meshing. STAR CCM+ offers tool options to

regenerate, improve triangulation, and prepare surface mesh in order to obtain high quality volume mesh. Such features used in this simulation case are surface remesher, and surface wrapper. Surface wrapper includes features to literally wrap surface in order to create or ensure a watertight model. This is an ideal function for repairing imported poor quality surfaces with intersecting surfaces, holes, and gaps, which is not for initiation of volume meshing. Surface remesher offers re-triangulation features to produce higher quality surface. It also enhances surface triangulation resolution. It is typically used in cooperation with surface wrapper to improve poor quality closed surfaces.

STAR CCM+ volume mesher contain three different types of volume mesh, each of which offers advantages and disadvantages of their own kinds. These three types are tetrahedral, polyhedral, and trimmed mesh. The tetrahedral volume mesher offers tetrahedral shape based core mesh. It provides an efficient and simple solution, which in turn uses the least amount of time and memory for a given numbers of cells. This, however, requires 5 to 8 times more mesh density than polyhedral and trimmed mesh to obtain same accuracy. It could be an ideal method when not much accuracy is required. Polyhedral mesher produces arbitrary polyhedral shape based core mesh. It provides a solution for complex mesh generation problems. Polyhedral mesher is relatively easy and efficient to execute. Polyhedral mesh contains approximately five times fewer cells than tetrahedral mesh for a given starting surface, and is more efficient. Both tetrahedral and polyhedral mesher is dependent on the quality of the surface mesh, meaning that bad quality surface mesh will lead to poor quality volume mesh. Trimmer model produces trimmed mesh based on hexahedral shape based core

mesh. It is similar to structured mesh, and provides high quality grids. Its methodology is robust and efficient for both simple and complex mesh generation problems. It utilizes hexahedral template mesh in which it is trimmed based on starting input surface. Unlike tetrahedral and polyhedral, trimmed mesher is independent on quality of starting surface. This means that bad quality of surface will not lead to bad quality volume mesh, and implies that it likely will produce good quality volume mesh in most circumstances. For reasons above, trimmer model is chosen to be a volume mesher used in the simulations, because it provides efficiency, quality and robustness of generated mesh.
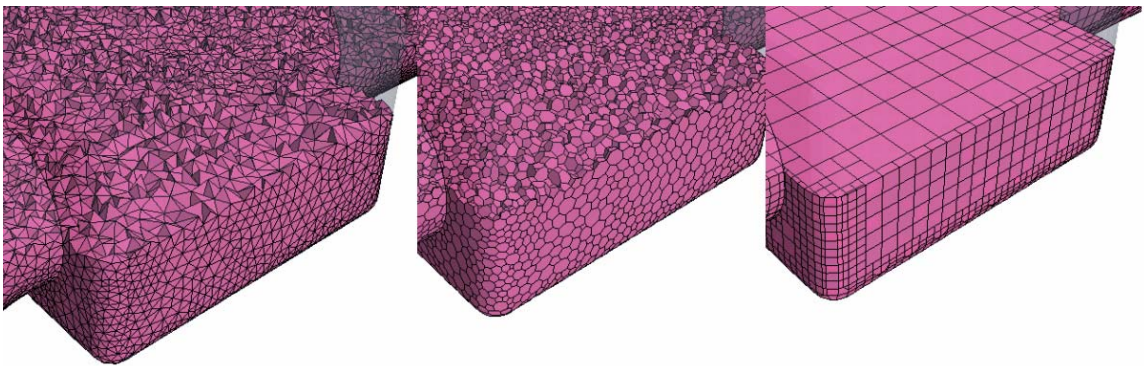
Figure 35: Three types of volume meshing; left: tetrahedral, middle: polyhedral, right:trimmer[6]

The quality of mesh depends on another factor which is grid density. It is very important for the volume mesh to contain a sufficient amount of grids at all or specific regions on the model. In certain regions where there are rapid changes in aerodynamic properties, a finer mesh is required in order to follow greater details of study of those changes, and enhance the accuracy of the results. Often times, these changes of aerodynamics properties occur due to shape complexity. It is beneficial to refine the number of mesh cells as this helps in maintaining the true shape of the

model. In other regions where finer mesh is not necessary, it is still important to assign a sufficient amount of grid cells because it may affect overall results.

Star CCM+ contains a useful tool, called volume shape, to adjust grid density where needed. Volume shape can be used prior to generating volume mesh. Three shapes could be assigned on the model, brick, cylinder, and cone. Regions where these volume shapes are placed on can be assigned different grid densities. This tool is very efficient for assigning specific grid density where needed. In this simulation, five models have the same fuselage and wing, but different geometry at fuselage-wing intersection, and varying overall position of the wing and fuselage. Thus, the first region that needs be considered for finer mesh is near the wing-fuselage intersection. The junction is a sensitive area which leads to differences in aerodynamics properties of each configuration. Secondly, another vital region is the wing itself. It is necessary that a sufficiently fine mesh needs be applied to maintain its shape and characteristics, because the wing is a primary source of aerodynamic forces on the airplane. Slight twist or changes in shape of the wing may alter aerodynamic forces significantly. The fuselage also requires sufficient numbers of mesh points as it significantly affects drag forces on the model. For both wing and fuselage, regions near and in front of nose area should also be assigned with greater numbers of grids since the changes in aerodynamic properties typically start near the nose area of the model. There should be sufficient amount of fine grids in front of the model such that alteration of forces can be thoroughly and properly calculated. Mesh within the free-stream boundary region should require enough grids to allow

simulated flow vectors to go through and be able to connect with finer regions for

precise calculation.

Model	Numbers of cells (half of model)
wing	1286141
configuration 1	1235649
configuration 2	2094913
configuration 3	1346558
configuration 4	1365803
configuration 5	1748566

Table 11: Numbers of cells used in volume mesh of wing and five wing-fuselage models
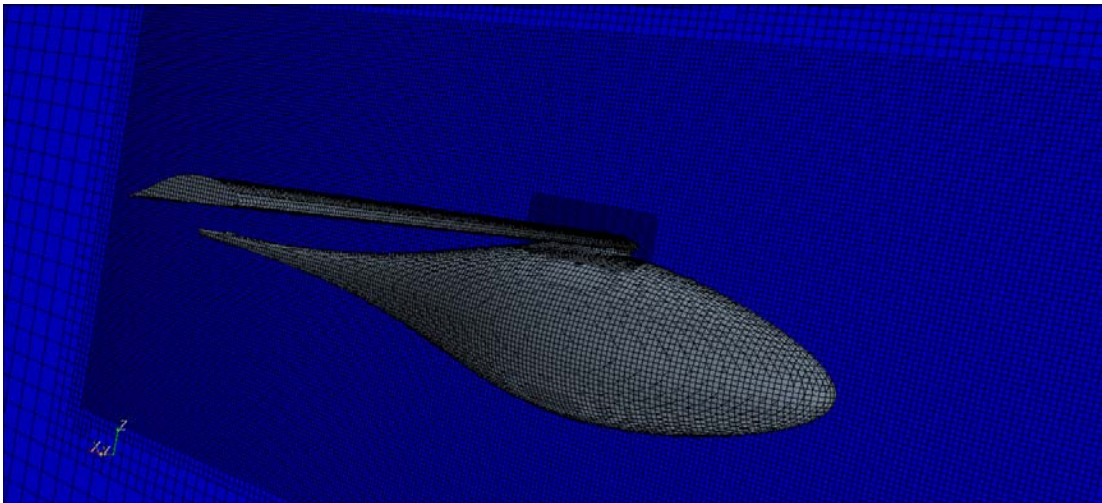
Figure 36: Mesh of configuration 3 generated with trimmer model meshing method

5.3 Physical Modeling

Physical modeling is a step in which physical condition are applied to the

models. It defines every environmental condition within the modeling domain that

will be simulated during computation. This is a most critical step before running the

simulation. The process must be done with great care because slight errors may cause

alteration of results. Therefore, all physical criteria expected to be simulated should

be precisely defined in this step.

STAR CCM+ has designed its functions to make physical modeling as simple as possible. It defines different physical categories, step by step for ease of operation. There is a total of 8 categories; some of which will be accounted for this case, and some of which will not. Here are 8 physical condition defined by STAR CCM+.

Physical Categories	Assigned Physical Conditions
Space, time and motion	Three-dimensional, Steady, Stationary
Materials	Gas, Air
Flow and energy	Segregated Flow Solver
Species	N/A
Turbulence	K-Omega model
Radiation	N/A
Combustion	N/A
Multi-phase flow	N/A

Table 12: Physical conditions for simulation

Space, time and motion characterize the basic physical environment of the model. Space refers to spatial independent variables, which the model is encountering, which in this case is three-dimensional. Time is specified to be steady, which means physical time-step is not required. The solution will be solved at one physical condition, and one physical time-step. Motion is assigned to be stationary as all mesh boundaries are motionless, and all reference frames are stationary.

Material assigned to the physical property is gas. Detail properties of air are specified including its dynamics viscosity, molecular weight, specific heat, thermal conductivity, and turbulent Prandtl number.

The flow and energy solvers are offered in two options; coupled flow solver, and segregated flow solver. The Coupled flow model solves the conservation equations for mass and momentum simultaneously using a time- (or pseudo-time-) marching approach [6].It offers both explicit and implicit integration schemes that are

first-order and second-order upwind. On the other hand, the segregated flow model solves the flow equations (one for each component of velocity, and one for pressure) in a segregated, or uncoupled, manner. The linkage between the momentum and continuity equations is achieved with a predictor-corrector approach [6]. The segregated model offers central and DES hybrid (second-order upwind/central) integration scheme for both first-order and second-order upwind.

Coupled flow solver offers more robust and accurate method to solve compressible flow problems. It also costs more time and computation resources than segregated flow solver. Coupled flow model is recommended for compressible flow, or model with large body forces and energy. However, this simulation demands solver merely solving especially incompressible flow with a low turbulence level. The segregated flow solver is chosen to solve the problem since it is the most efficient, and is expected to provide satisfactory accuracy. It solves the governing equations with second-order central integration scheme.

A turbulence model must be chosen appropriately, even though turbulence level of 0.21%, default value of GLMWT wind tunnel, may seem insignificant. It does influence occurrence of boundary layers separations and transitions. There are four models available in STAR CCM+; Spalart-Allmaras, K-Epsilon, K-Omega, and Reynolds Stress Transport. K-Epsilon models offer good balance between robustness, costs and accuracy. It is suitable for complex recirculation problem. Reynolds Stress Transport is most suitable for strong and complex turbulent situation. And it is the most computationally expensive models available. Both K-Epsilon, and Reynolds Stress Transport, therefore, are not well suited for this incompressible flow problem.

Spalart-Allmaras models and K-Omega models are most seen in Aerospace industry application. They are suitable for application in which its boundary layers are not largely separated. K-Omega models are claimed to captures performance by differences in model, rather than focusing on a higher-degree complexion of physics. K-Omega appears to be the best option to use in the current simulation. The input values require turbulence intensity of 0.21% with mild turbulent viscosity ratio ($\frac{\mu_t}{\mu}$) of approximately 100.

Other physical modeling options are not applicable to the current computation. After physical model is being set, input values must be entered in order to proceed the analyzing step.

Input Condition	Input Values
Air Dynamic Viscosity	1.417E-5 Pa-s
Reference Pressure	101325 Pa
Static Pressure (Initial Condition)	0 Pa
Static Temperature (Initial Condition)	300 K
Air Density	1.17 kg/m^3
Initial Velocity	80 MPH
Mach Number	0.102709
Turbulent Intensity	0.21%
Turbulent Viscosity Ratio	100
Flow Direction	Varies with AOA

Table 13: Input conditions for physical condition setup

Air Dynamic Viscosity is obtained by using Reynolds equation. Air density value is the same as the value of wind tunnel experiment air density at 80 MPH, which is 1.17 kg/m^3.

$$\text{Re} = \frac{\rho U_\infty L}{\mu} \qquad \text{, where } \rho = 1.17 kg/m^3$$

$$U_\infty = 35.7632 m/s \text{ (80 MPH)}$$

$$\text{Re} = 9 \times 10^5$$

$$L = 0.3048 \text{ m (12 inch chord)}$$

Therefore, the value of dynamic viscosity corresponding to the design Reynolds number is, $\mu = 1.417\text{e-}5$ kg (m/s). Other specifications of air such as molecular weight, specific heat and turbulent Prandtl Number use standard values set by the software. It is considered reasonable because at incompressible flow condition, these values are close or unchanged from standard sea level values, which are provided by the software

Reference pressure and temperature values are taken from experimental data. They are roughly the same as standard sea level condition. Initial velocity is set as experiment at 80 MPH or 35.7632 m/s free-stream flow condition. Mach number is the result of wind velocity, pressure and density. The calculation is as of this equation,

$$U_\infty = M\sqrt{\frac{\gamma P_{ref}}{\rho_{ref}}} \quad \text{Therefore, } M = U_\infty \left(\sqrt{\frac{\gamma P_{ref}}{\rho_{ref}}} \right)^{-1}$$

, where $P_{ref} = 101325 Pa$, $\rho = 1.17 kg/m^3$, $\gamma = 1.4$, and $U_\infty = 35.7632$ m/s

Thus, Mach number achieved from this calculation is 0.102709.

Turbulent intensity is approximately 0.21% which is a characteristic of the flow in the GLMWT. Turbulent viscosity ratio is roughly approximated to be 100, which is considered mild or non boundary layer separation. By choosing turbulent

suppression option, the program will automatically calculate transition boundary layer, and transition boundary distance. Flow direction specification depends on angle of attack. The simulation runs at 7 different pitch angles; +5, +2.5, 0, -1, -2.5, -5, -7.5, -10 degrees, which is the same range as the experiment. All of which also has its wing incidence at 6.5 degrees angle of attack. The calculation of flow direction specifications is simply varied upon sine and cosine law.

5.4 Running simulations

After having set up proper physical and initial conditions, simulations can be initiated. Each simulation run takes approximately takes 10 hours per configuration, but it also varies upon mesh numbers and convergence behavior. STAR CCM+ produces a residuals plot for each simulation, which graphically display products from solving equations versus iteration step in log-log scale. The products from residuals are not necessarily interesting engineering variables such as forces, or pressure, etc. Residual displays are good for judging convergence of simulations. Good convergence is judged by having all residuals to be steady and/or drop by some order of magnitude. However, sometimes if initial conditions match perfectly for solutions, residuals may drop only slightly, and stay level throughout the simulation.

Often times, a solution may not converge and oscillations occur. This may be caused from insufficient number of cells. One can try to stabilize or take the result as is. Figure 37 shows convergence of residuals. It can also be observed by looking at the report plot. Once the plotted result becomes unchanged per iteration; that

indicates the sign that the convergence has occurred. It is important to judge

convergence with care in order to obtain final and correct results.
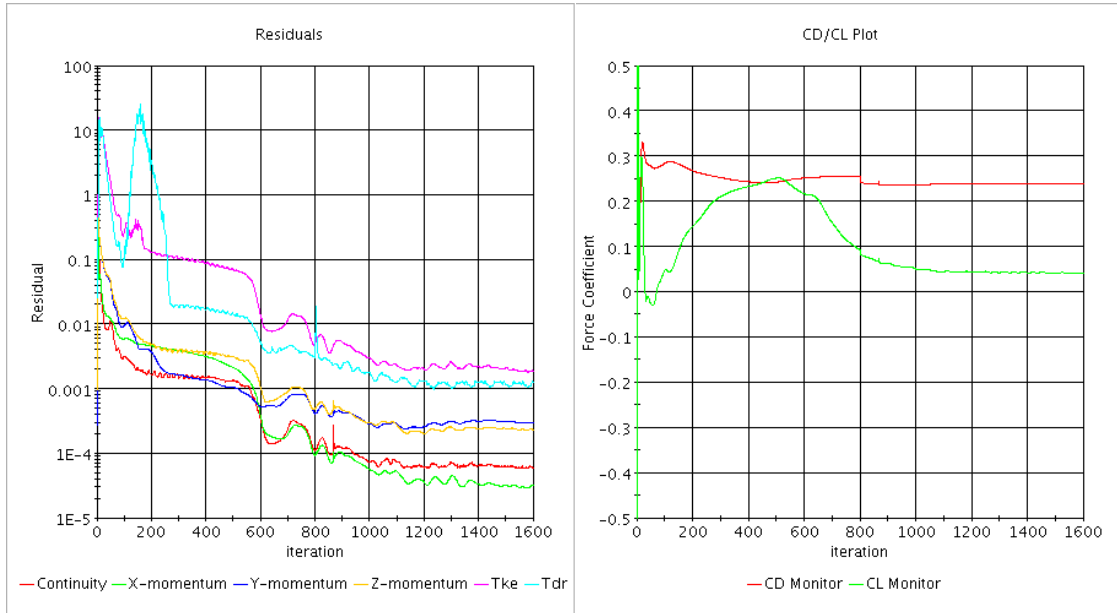
Figure 37: Sample of convergence residuals [6]

CHAPTER 6: Computational Fluid Dynamics (CFD) Simulation Results and Discussion

The CFD simulation is included in this research for the purpose of studying flow behavior over the models, including flow interaction between the wing and the fuselage. The flow field information available from the CFD simulation helps to understand of the experimental results. The aerodynamic forces from the CFD simulations exhibit larger differences from the experiment than are easily explained, but the inclusion of the results is considered useful. The results from the CFD simulations are given only at the 80MPH airspeed condition. This is because performing the computations for additional conditions would require more resources than were available for this study. Results were obtained for five configurations including wing. For each configuration simulations were done for 8 pitch angles; +5, +2.5, 0, -1, -2.5, -5, -7.5, -10 degrees. The wing has its wing incidence angle of 6.5 degree. Flow conditions are described in details in section 4.2. The results of the CFD simulations are displayed in this chapter.

6.1 Computational Results of the Wing

Figure 38 shows the computational results for wing lift coefficient versus pitch angles along with the experimental results. Figure 38 shows the computational results for the wing drag coefficient versus pitch along with experimental results. Results of the wing simulation are within a respectable range of comparison with the experimental results. The lift coefficient agrees with the experiment quite well. The drag coefficient curve has a similar shape to that from the experiment, but the values

are not close throughout the range of pitch angles computed. Typical wing stall occurs for the CFD results around 2.5 degrees pitch while the experiment does not exhibit a typical stall characteristic. This is not typical wing alone case, as the wing tips are quite close to the wind tunnel walls. Overall, lift coefficient prediction is rather more accurate than drag prediction.

Wing Lift Coefficient
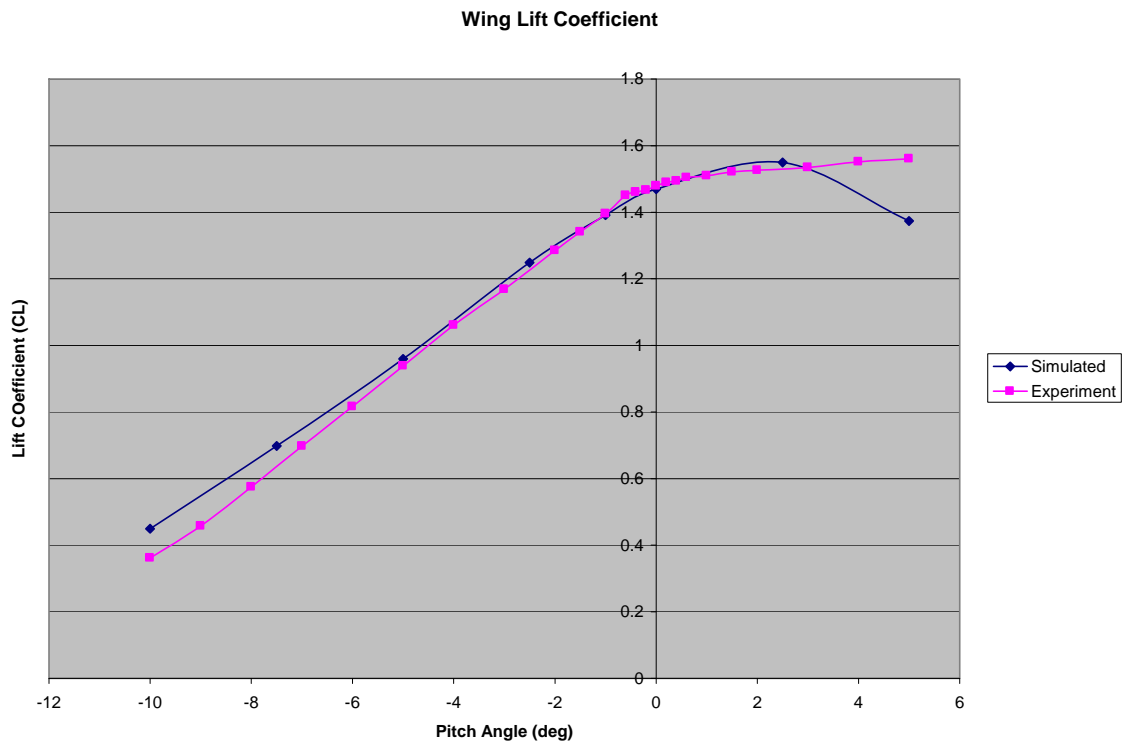
Figure 38: Wing lift coefficient C_L comparison between computational result and experimental result

At the extreme of negative and positive pitch angles, wing lift prediction has the largest errors. This is where separation occurs on the upper and the lower surfaces of the wing. In the mid-range of pitch angles, lift prediction is very close to the experiment. Positive pitch angles are where the wing is expected to gradually stall as pitch angle increases. The CFD result shows stall occurs at +5 degree pitch angle although the experimental result shows no significant reduction in lift at this pitch

angle. As lift coefficient drops, the drag coefficient rises due to flow separation on top of the wing. This is in contrast to the experiment, where lift continues increasing slowly out to the maximum measured pitch angle of 6 degrees.

Wing Drag Coffficient
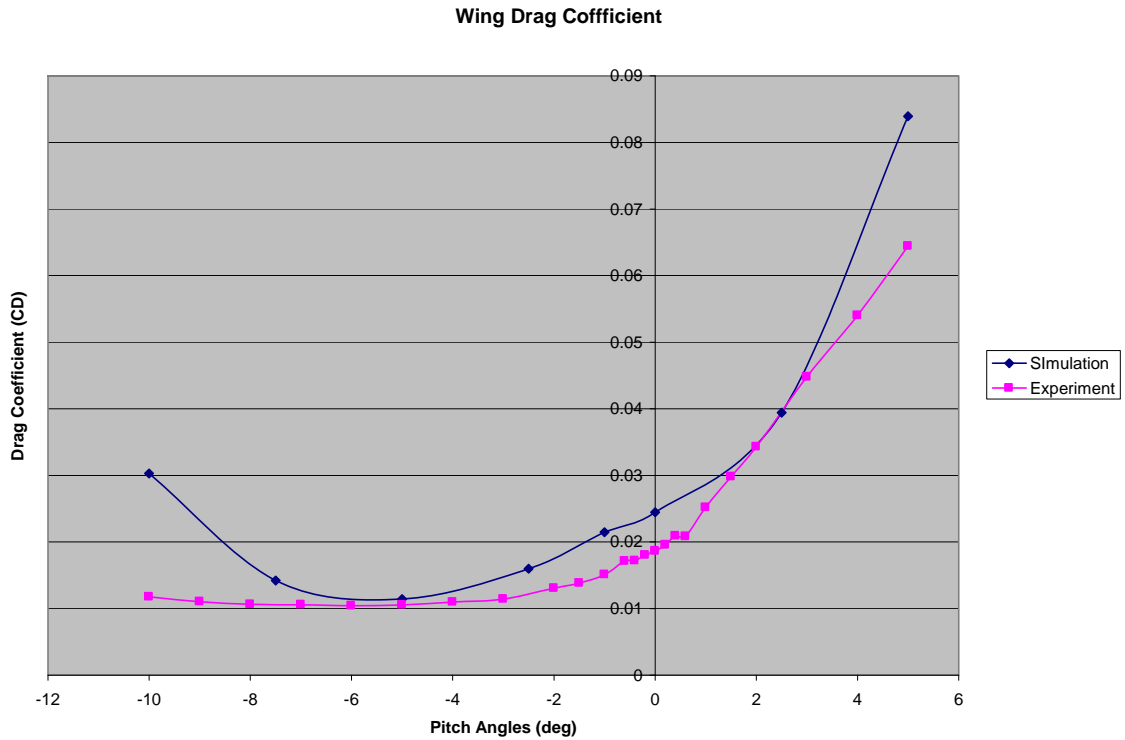
Figure 39: Wing drag coefficient comparison between computational result and experimental result

The wing drag coefficient curve from the simulation has characteristics somewhat similar to the experiment but always higher. The largest differences between the experiment and CFD simulation are at -10 and +5 degree pitch angles. This is due to high sensitivity to separated flow regions in the simulation. At -10 degree pitch, separation occurs on the lower surface of the wing. And at +5 degree, the separation occurs on the upper surface of the wing. Other points within the non-stall region offer reasonable prediction. Nevertheless, in comparison with lift prediction, the drag prediction tends to be less accurate. The drag coefficient

70

prediction also shows more intensive stall behavior especially at -10 degree pitch

angles.

Wing Lift to Drag Ratio
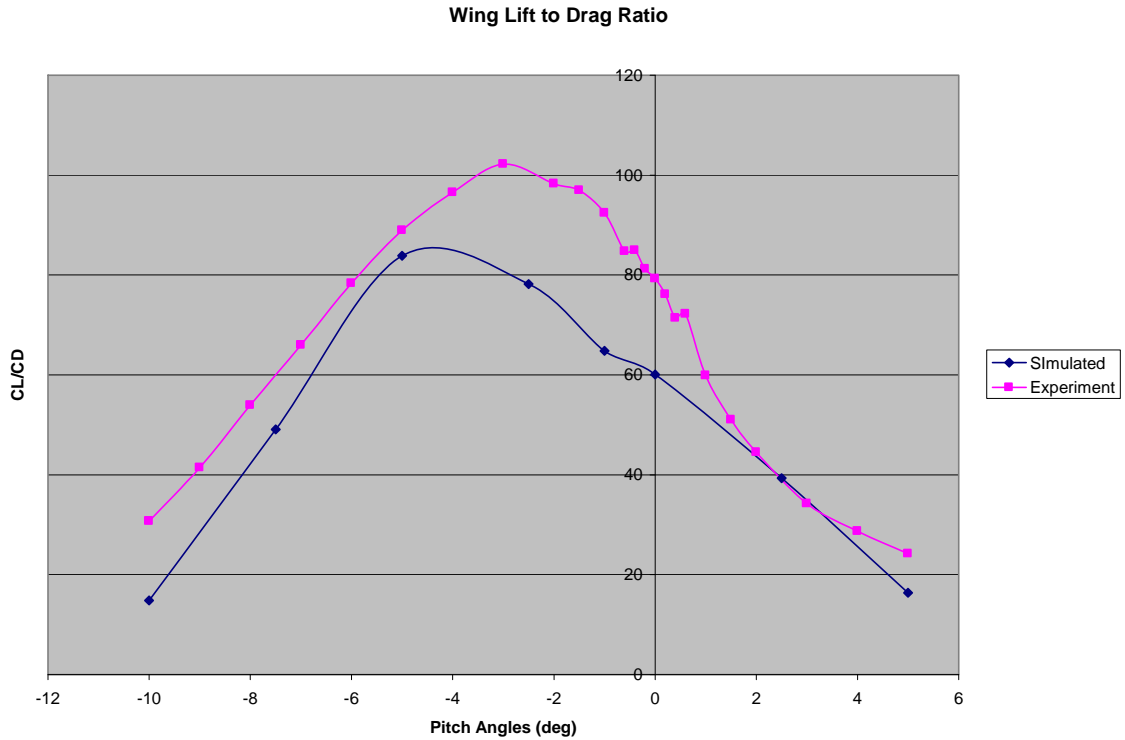
Figure 40: Wing lift to drag ratio comparison between computational result and experimental result

Figure 40 shows a comparison of simulated and experimental results for the

C_L/C_D. Errors of prediction for C_L/C_D of is larger than drag and lift prediction

individually. Nevertheless, the predicted plot has a similar shape and slope as the

experiments. The predicted C_L/C_D is overall less favorable as the result of higher

overall predicted drag values. Maximum lift to drag ratio from the computation

occurs at about -5 degree pitch with a value of 83.84, where the experiment yields

maximum C_L/C_D of 102.24 at -3 degree pitch.
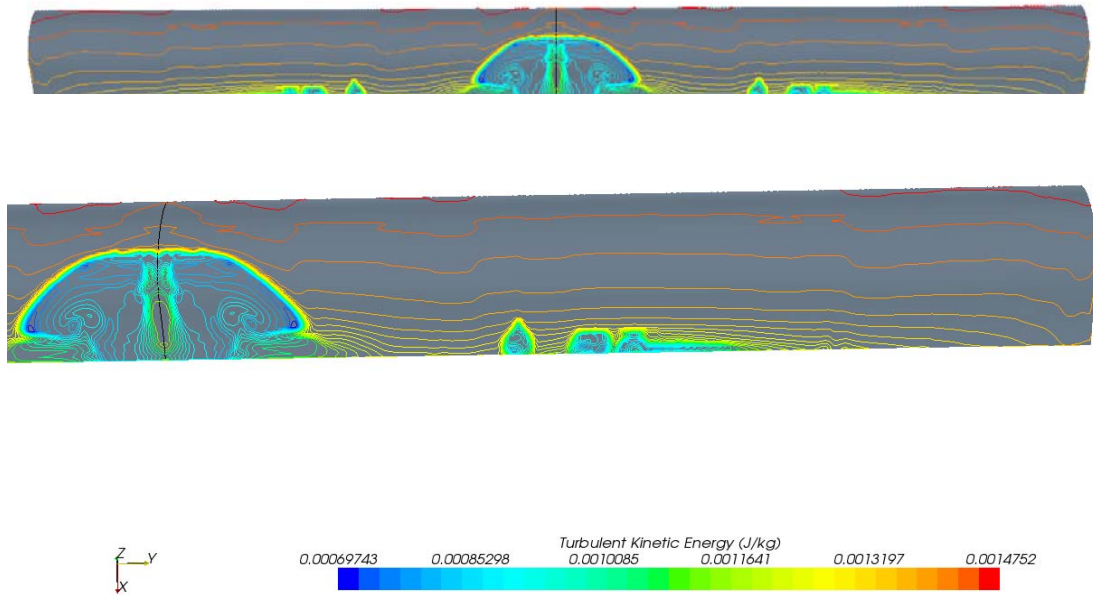
Figure 41: Result of turbulent kinetic energy (J/kg) calculation of wing at +5 pitch angle showing mushroom pattern separation over the wing upper surface

Figure 41 shows turbulent kinetic energy at the wing surface for pitch equal +5 degrees. The upper image shows the full span view of the upper surface while the lower image shows a zoomed in view of the right semi-span and part of the left semi-span.   The pattern on the wing upper surface exhibits a primary mushroom shaped separation at the center and 3 small regions approximately half way out the semi-span. The central cell extends from the trailing edge to a bit forward of the half chord and is somewhat more than a chord length in total span.   This phenomenon takes place at high angle of attack showing aspects of wing stall.

The graphical display is generated as contours of turbulent kinetic energy (K) which is calculated as follows,

$$K = \frac{3}{2}(U_{avg}I)^2 \qquad , \text{where } U_{avg} = \text{mean flow velocity}$$

$$I = \text{turbulent intensity}$$

Lighter turbulent kinetic energy occurs over the separation regions and higher values occur over non-stall regions. This is because flow velocity over the separated region on the wing surface is either diverse or lower than non-stall regions regarding to above equation.

Separation also occurs at -10 degree pitch angles, but over the wing lower surface. The shapes of separation pattern differ from those of high angle of attack separations. For both types, reversed shear stress can be observed over separation regions. The flow starts from the trailing edge moving upward against incoming flow until reaching the separation line. The separation spreads sideway toward both wing tips. A vortex shape is formed, in which its strength is combined with wing tip vortices.
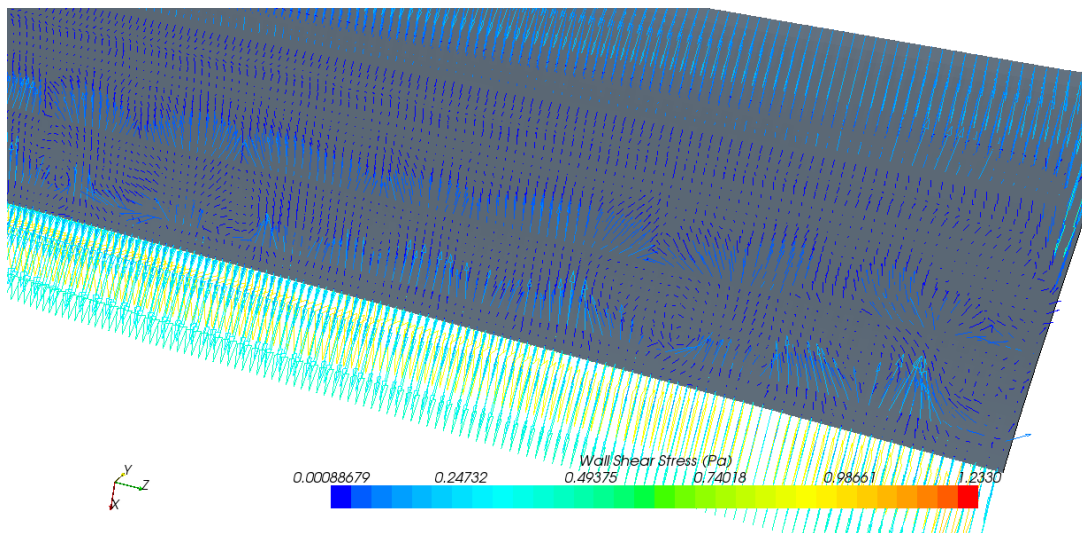
Figure 42: Flow separation pattern of wing lower surface at -10 degree pitch angle shown by wall shear stress vector calculation

The separation phenomenon occurs at both high positive and high negative angle of attacks. Experiment results does not exhibit rapid drag increase associated with wing stall either at high positive or high negative angles of attacks.

6.2 Computational Results of the five wing-fuselage configurations

Five wing-fuselage configurations are simulated to study behavior of flow around wing-fuselage junctions with particular focus on viewing the results in comparison to results of the experiment in the wind tunnel as well as for comparisons among the different configurations. The simulation runs include 40 cases; i.e. five models with 8 pitch angles for each model. Flow conditions are assigned to obtain close similarity with the wind tunnel experiment. Integrated total force components were computed primarily for drag and lift. Flow visualizations are used to assist in discovering reasons for the flow behavior observed/measured.

6.2.1 Computational Results: Lift Coefficient versus Pitch Angle

Lift Coefficients from the simulations are shown in figure 43. Figure 43 should be compared to Figure 26 which shows experimental results. Here we focus on a comparison of the configurations as predicted by the CFD simulations.

Lift Comparison From Simulation
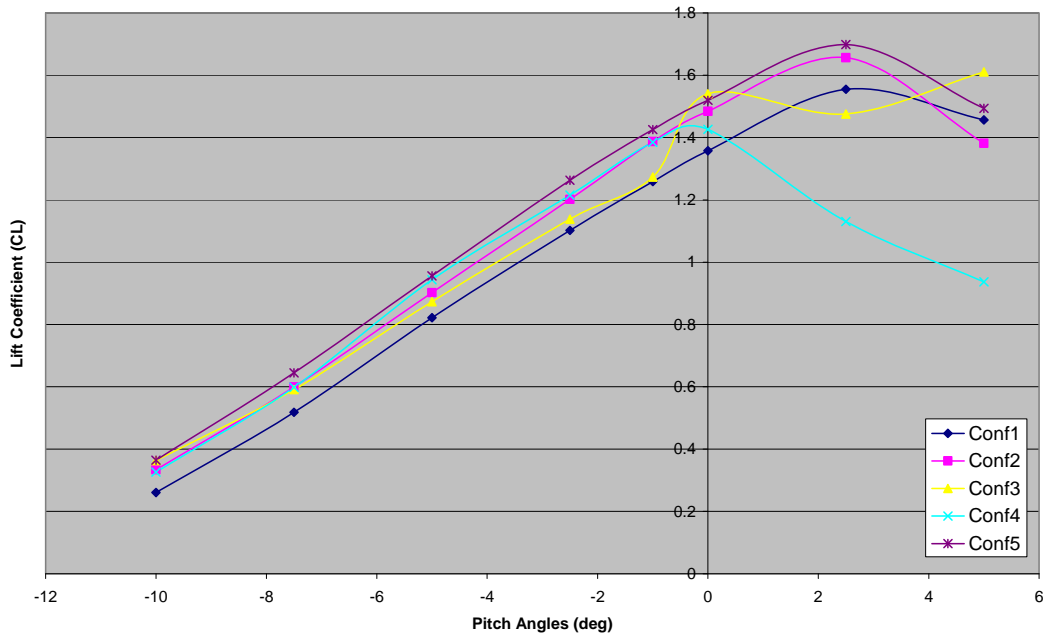
Figure 43: Predicted Lift Coefficient of five wing-fuselage configurations by Star CCM+ simulator with freestream condition at 80 MPH

The lift vs. pitch curves for configurations 1, 2, and 5 are quite similar with a zero offset and differing maximum values all occurring at the same pitch angle of +3 degrees. The curves for configurations 3 and 4 are different and differ from each other. Configuration 3 has an anomalous point at pitch of zero degrees and is continuing to rise at the highest pitch angle simulated of + 5 degrees. Configuration 4 appears to simply stall near pitch equal to zero degrees. Configuration 5 exhibits the overall highest lift coefficient with a maximum of 1.699 at 2.5 degree pitch angle.

There is some conflict between simulation and experimental data. Experimental lift coefficients do not drop after having reached their maximum values showing mild stable behavior, whereas the simulations always exhibit an abrupt stall behavior except possibly for configuration 3.

Direct comparisons of experimental results and CFD results for lift versus

pitch angles are now given by Figures 44 through 48.

Lift Coefficient Comparison Configuration 1
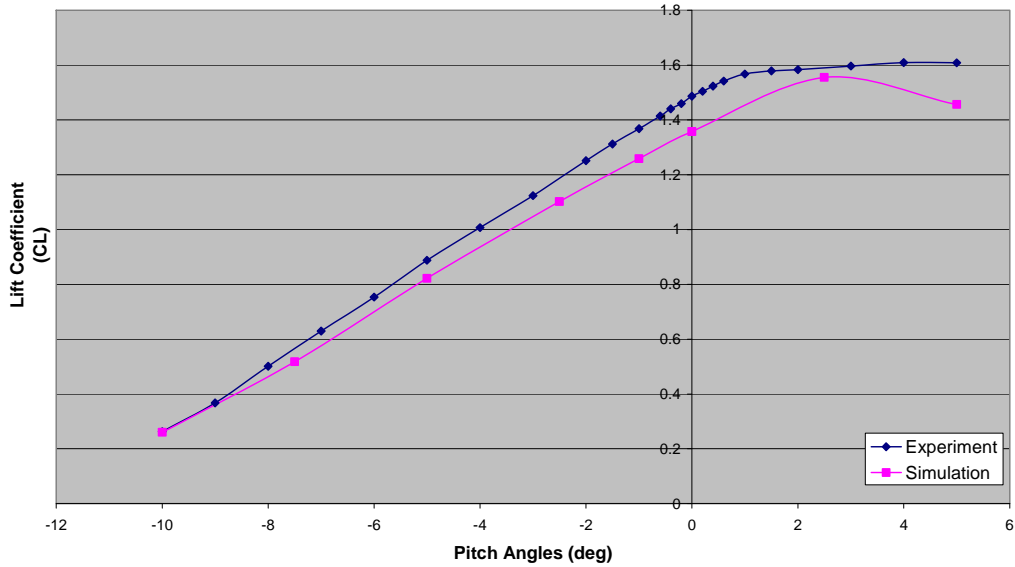
Figure 44: Comparison between experimental and simulational results of lift coefficient of the wing-fuselage configuration 1 at 80 MPH

Lift Coefficient Comparison Configuration 2
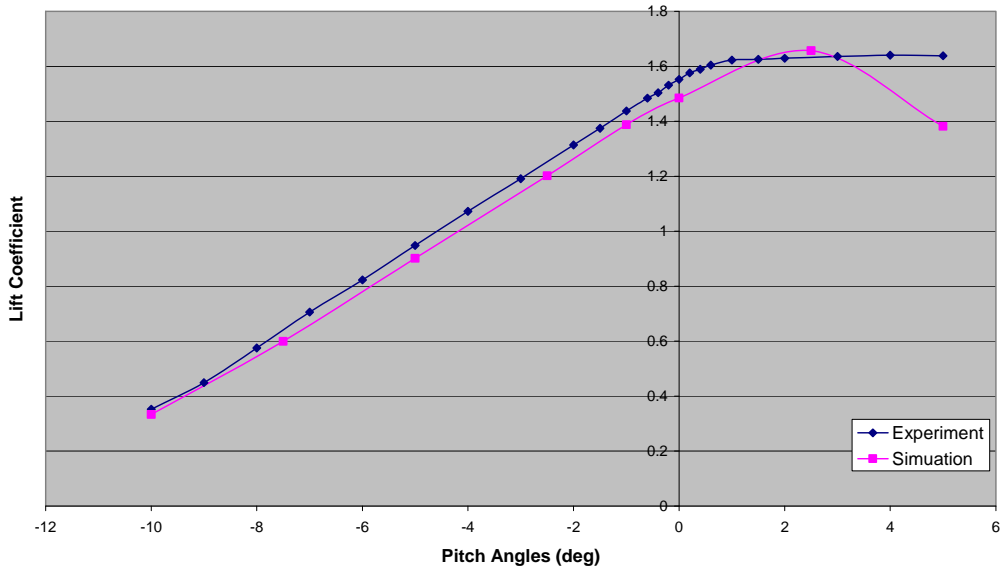
Figure 45: Comparison between experimental and simulational results of lift coefficient of the wing-fuselage configuration 2 at 80 MPH

Lift Coefficient Comparison COnfiguartion 3
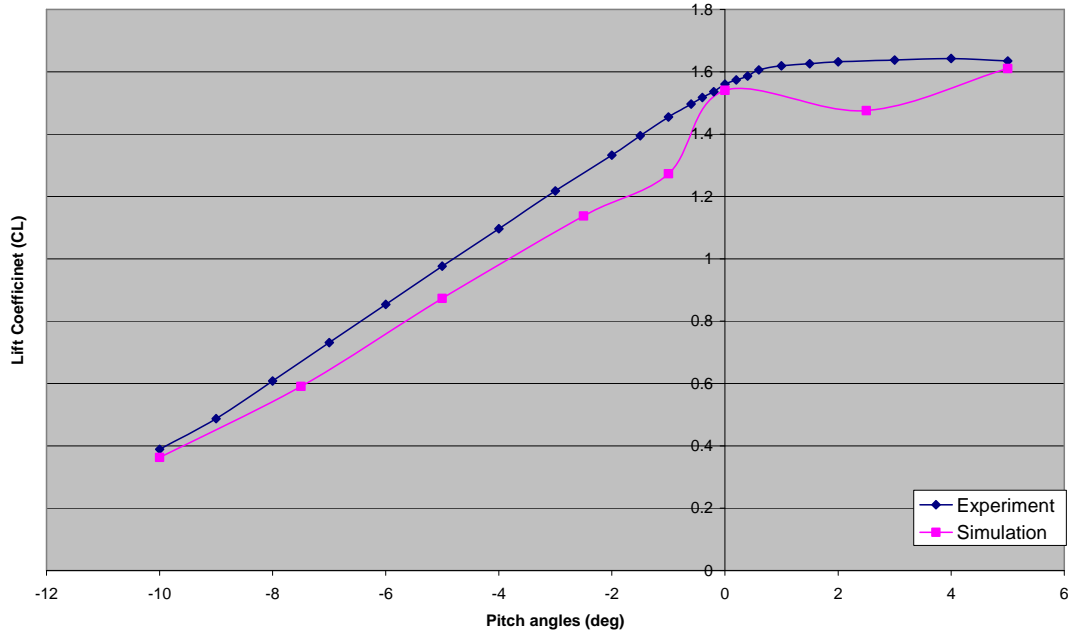
Figure 46: Comparison between experimental and simulational results of lift coefficient of the wing-fuselage configuration 3 at 80 MPH

Lift Coefficient Comparison COnfiguration 4
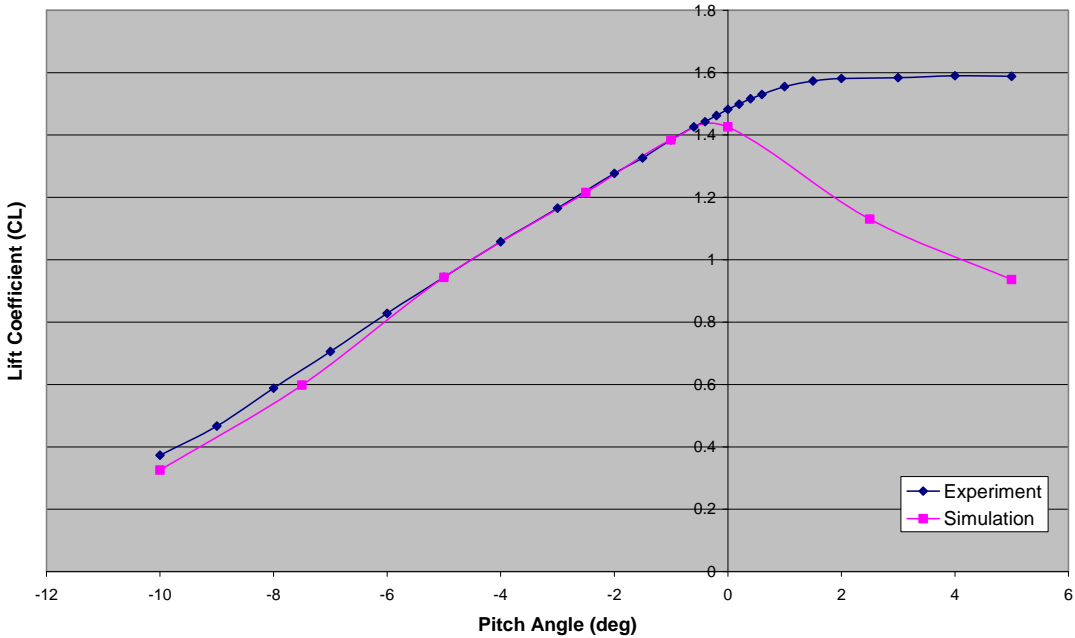
Figure 47: Comparison between experimental and simulational results of lift coefficient of the wing-fuselage configuration 4 at 80 MPH

Lift Coefficient Comparison Configuration 5
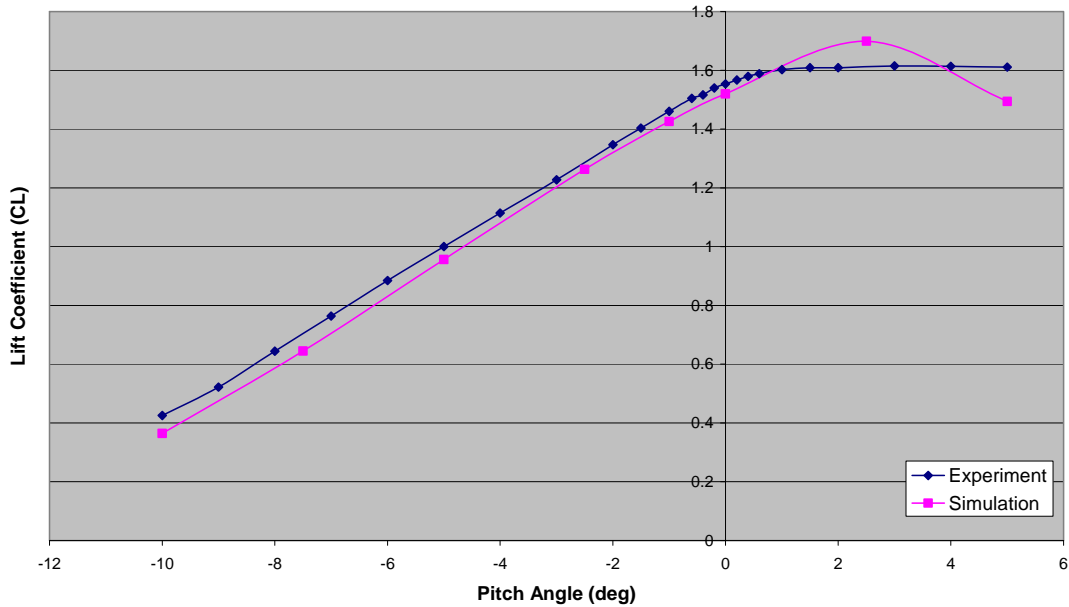
Figure 48: Comparison between experimental and simulational results of lift coefficient of the wing-fuselage configuration 5 at 80 MPH

Figures 46 through 48 shows direct comparisons of lift coefficient between experimental results and computational results. The graphs also explicitly show that errors of computation are largest where separations occur. It is noticeable that the lift slopes from the simulations data tend to be lower than the experiment. This implies that the computation may exaggerate flow separations, which limits performance of the models. Anomalous points appear most with configuration 3 followed by configuration 4. Results of lift prediction of other models seem to be within reasonable range of accuracy, especially for configuration 5 and configuration 2.

6.2.2 Computational results: Drag Coefficient versus Pitch Angles

Figure 49 through 53 show drag coefficients comparison between computational results and experimental results. Recall from figure 29, the results of drag from the experiment shows that configuration 1 produces highest overall drag, whereas configuration 5 and 2 produce smallest drag at different regions, negative pitch and positive pitch respectively. However, the focus of this section is to discuss and compare results of the simulation to the experimental results.

Drag Coefficient Comparison of Configuration 1
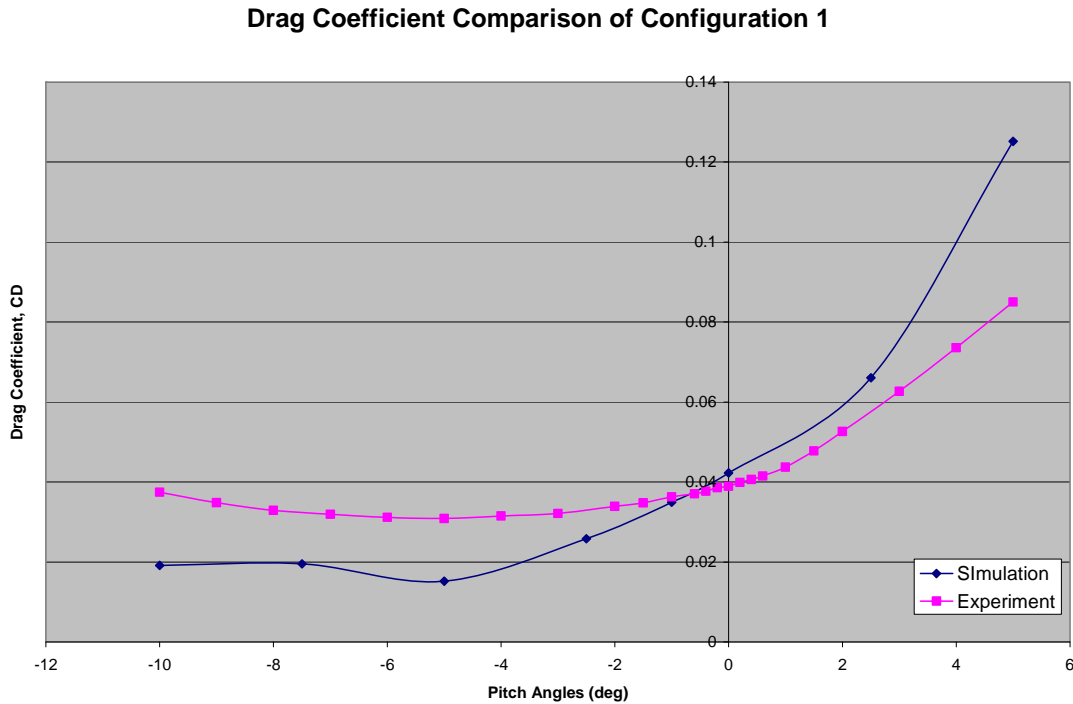
Figure 49: Comparison between experimental and simulation results of drag coefficient of the wing-fuselage configuration 1 at 80 MPH

Although all drag predictions follow the same trend lines as the measured values from the experiment, they are still not accurate, especially when compared to the lift predictions. The largest errors often occur at positive pitch or stall region, where flow separation is highly expected. The errors, overall, seem to have random pattern, do not have any fixed trend that has been identified.

Drag Coefficient Comparison of Configuration 2
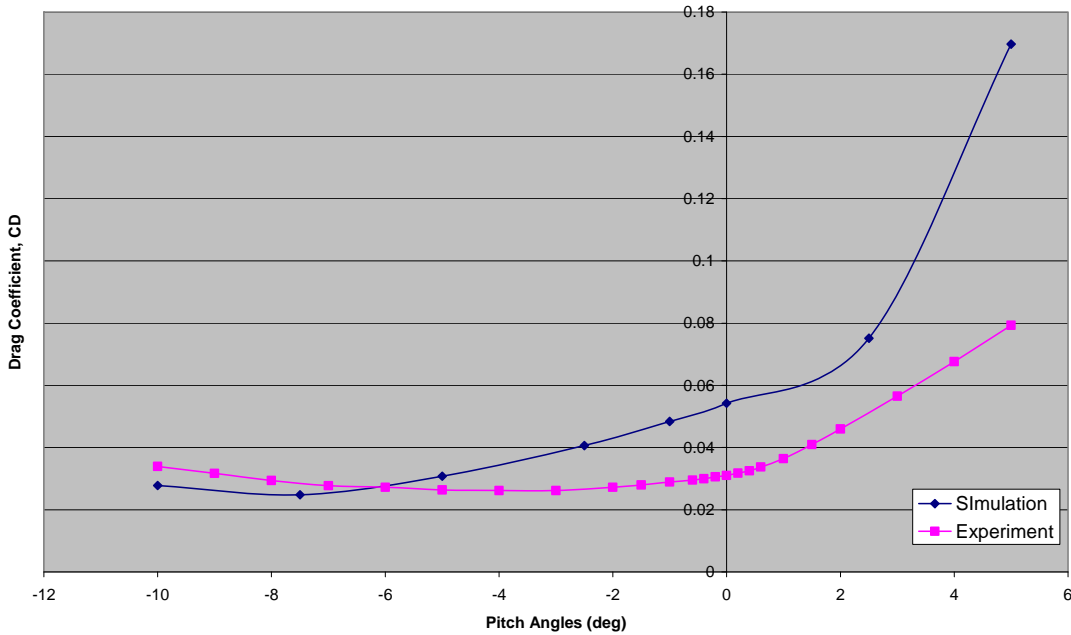
Figure 50: Comparison between experimental and simulation results of drag coefficient of the wing-fuselage configuration 2 at 80 MPH

The prediction of configuration 5 and 1 seems to give more accurate results than others. The simulated drag values of configuration 5 surprisingly show good accuracy at stall regions, but its errors are contained largely at low negative points. Configuration 3 and 4 shows unrealistic results at higher pitch angles, in which it repeats the same behavior as the lift prediction. Overall, the computational drag results follow the same trend lines as the experimental values, but with rather large absolute errors.

Drag Coefficient Comparison of Configuration 3
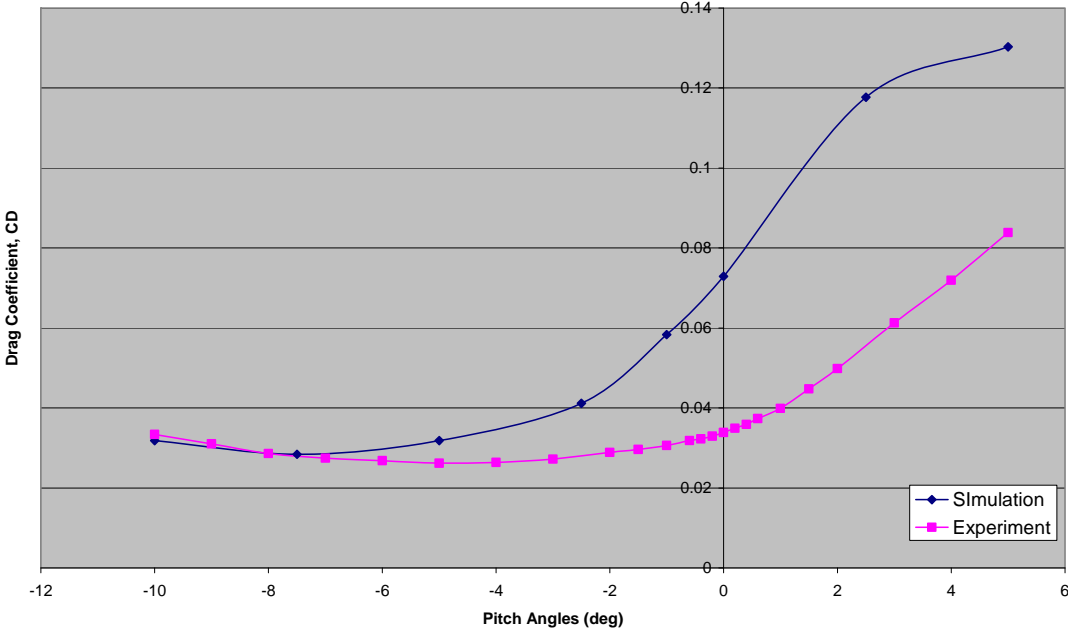
Figure 51: Comparison between experimental and simulation results of drag coefficient of the wing-fuselage configuration 3 at 80 MPH

Drag Coefficient Comparison of Configuration 4
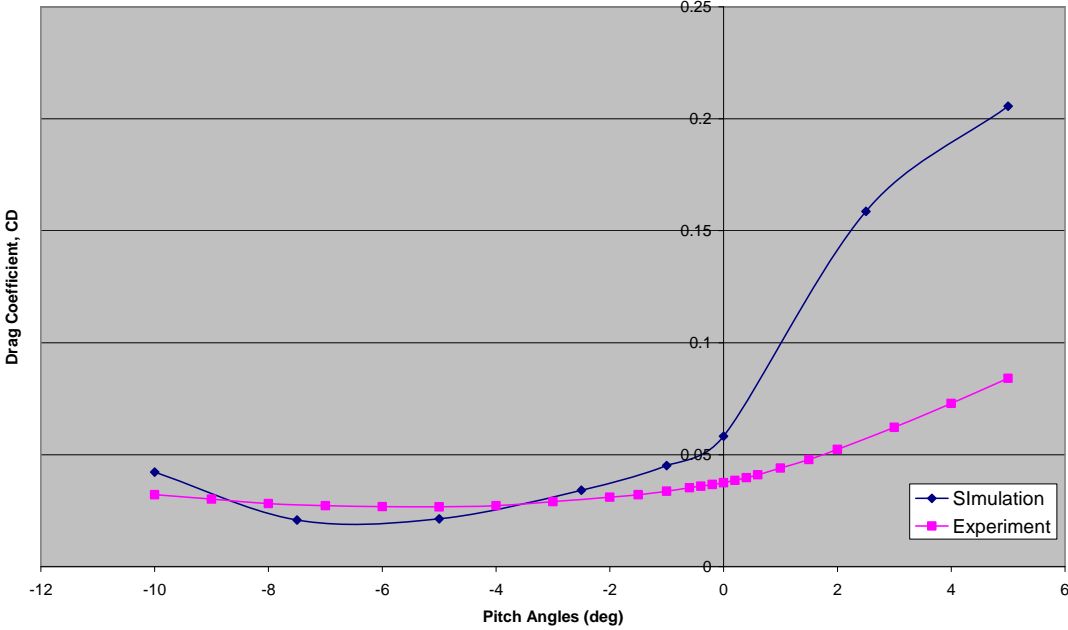
Figure 52: Comparison between experimental and simulation results of drag coefficient of the wing-fuselage configuration 4 at 80 MPH

Drag Coefficient Comparison of Configuration 5
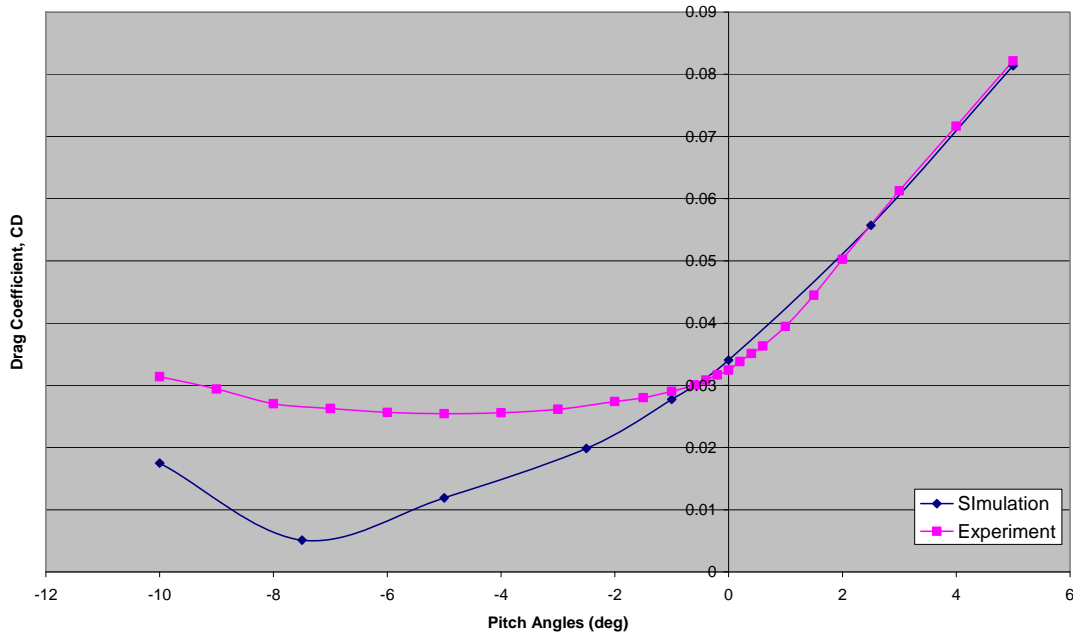
Figure 53: Comparison between experimental and simulation results of drag coefficient of the wing-fuselage configuration 5 at 80 MPH

6.2.3 Computational results: Lift Coefficient versus Drag Coefficient

Figure 54 shows the simulated lift coefficient versus drag coefficient for the five configurations. The wing-fuselage configuration 5 shows the overall best performance in comparison to other models. This is consistent with the experiment. However, the ranking of the other configurations from the CFD results is entirely different from the ranking obtained from the experiment. For example, the computational results show that configurations 1 and 2 have mediocre performance, with configuration 3 to be the worst. On the other hand, the experimental results show that configuration 1 is the worst, configuration 3 and 4 are the mediocre ones, and configuration 2 is the second best. The overall results of simulations contain large errors mainly due to inaccuracy of drag prediction, since the lift prediction is within

reasonable range of accuracy. Nevertheless, one data that the simulation agrees with

the experiment in that the performance of configuration 5 exceeds others.

Simulation Lift VS Drag Comparison
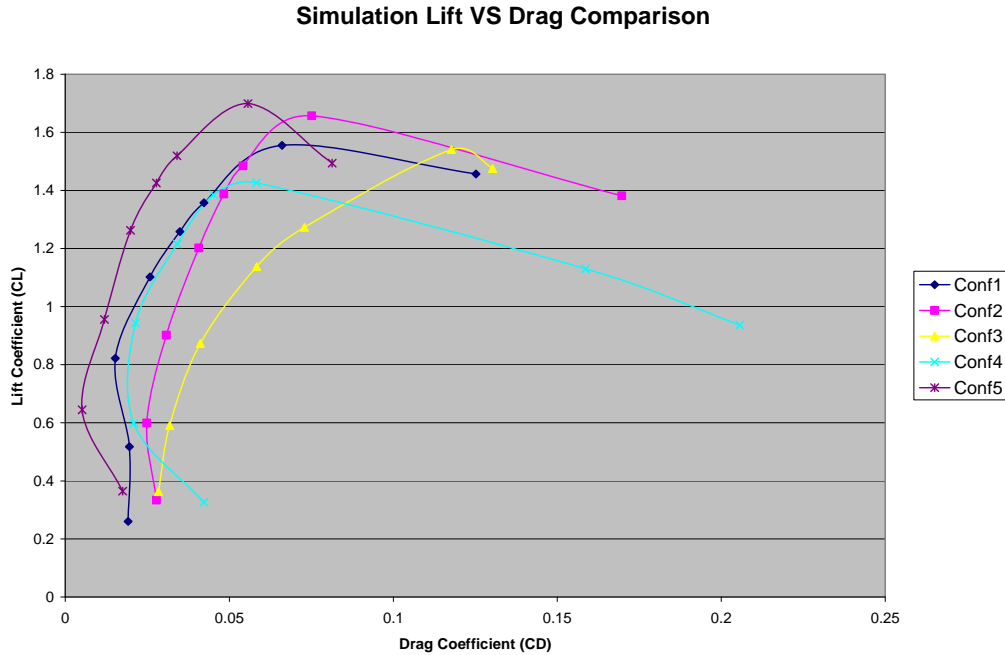
Figure 54: Predicted Lift to drag Coefficient of five wing-fuselage configurations by Star CCM+ simulator with freestream condition at 80 MPH

Although the simulation may not provide very accurate results, it can

somewhat determine characteristics of each configurations. For example,

configuration 4 shows early stall characteristics in the experiment. The simulation

shows similar behavior but with more extreme results. Configuration 1 is predicted to

have lowest maximum lift. Configuration 3 is shown to have high lift, but also high

drag which leads to limitation of its performance. These characteristics of the

prediction are similar to the experiment, even though they are not greatly accurate. It

is considered to be reasonable to use the advantage for flow visualization which was

not available in the experiment.

6.2.6 Discussion and presentation of some flow field details from simulations

This section describes and illustrates flow behavior as indicated by the simulation of five configurations.
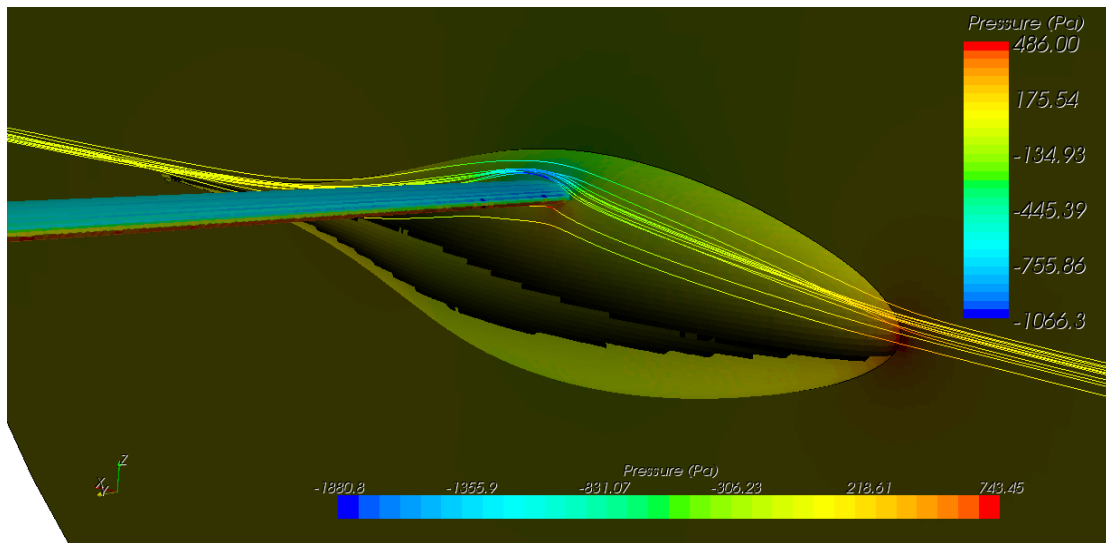
Figure 55: Pressure distribution of wing-fuselage configuration 1 at 0 degree pitch angle

Figure 55 shows the pressure distribution of the wing-fuselage configuration 1 along with plots of selected streamlines. At 0 degree pitch angle the model configuration 1 has smooth streamlines passing in the near region of the wing-fuselage junction. The pressure distribution indicates lower pressures on the upper surface on the wing and high pressure on lower surface, and low pressure on upper surface. Higher pressures also appear at stagnation points, such as the fuselage nose and wing leading edge. This illustration serves as an example of flow visualization using the results of the CFD simulation. Other configurations behave in similar ways at non-stall pitch angles although details differ and corresponding integrated forces vary.

In order to compare performance of the five configurations, appropriate criteria must be chosen. It has been decided compare the configurations with the pitch angle to be standard at zero degrees, because this is near the range of maximum lift to drag ratio of all models and it also is the point where all configurations are about to enter stall regions. Figure 56 through 60 show the wall shear stress calculation in vector form in front of or behind the wing-fuselage junction.
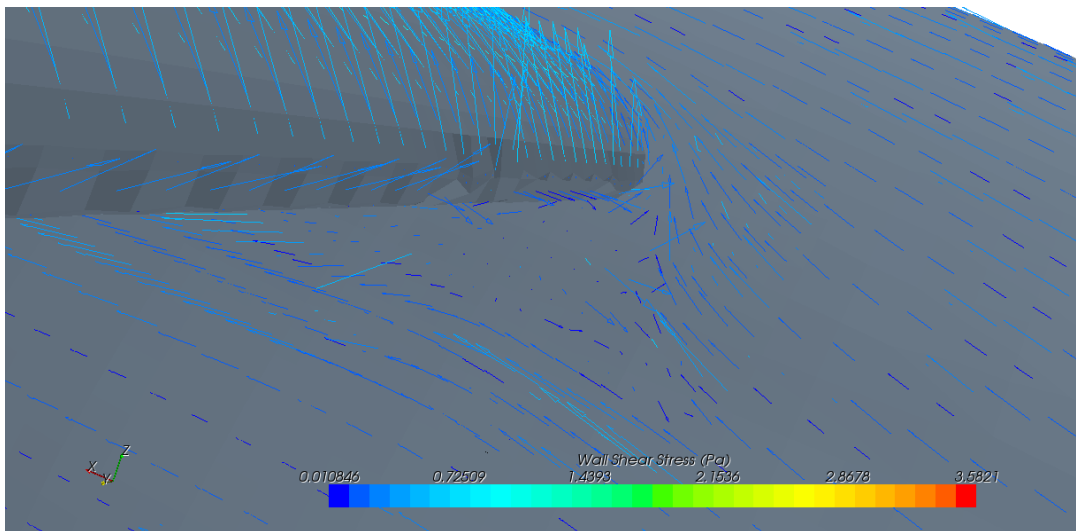
Figure 56: Wall shear stress Flow visualization of wing-fuselage configuration 1 at 0 degree pitch angle

Figure 56 shows the vector flow visualization of wall shear stress calculation. The wall shear stress pattern indicates that there is a slight reversed flow at the wing-fuselage junction, which causes slight drag increment. A sharp corner intersection does not have fillet to prevent or alleviate flow separation. Turbulence also occurs underneath the wing and slightly behind the junction. This may cause a limitation of lift being produced, and may lead to a drag increment.
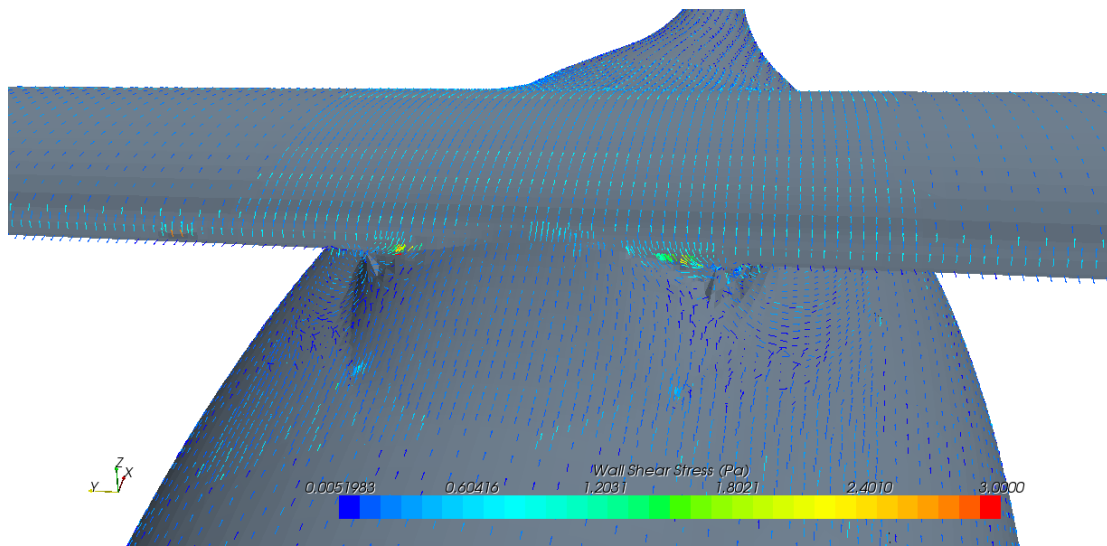
Figure 57: Vector result of wall-shear stress calculation on wing-fuselage configuration 2 at zero degree pitch angle at 80 MPH

Figure 57 shows mild separation in front of the wing-fuselage junction. Little or no turbulence can be observed aft of the wing-fuselage intersection. The separation in front of the wing shows no sign of vortex formation, and flow separation behavior is very subtle. However, vector lines do show airstreams moving downward on the fuselage surface underneath the wing. This could be due to the height of the wing not being sufficiently high above the fuselage. This costs some amount of drag rises. However, the simulation may be more sensitive than what actually happened, because the drag computational results slightly higher than the experimental results.

Configuration 3 has computational drag highest among all models. Vector calculation of wall shear stress shows high flow turbulence in front of the wing-fuselage intersection as displayed in figure 58. The design of the fairing seems to induce separations even prior to reaching the wing-body junction. This causes slightly reversed wall shear stress reflecting the formation of a vortex on top of fuselage. However, the wing itself does not experience this turbulence. This phenomenon

definitely limits the performance of this model. Again, the computation may show more sensitivity of separation than the experiments.
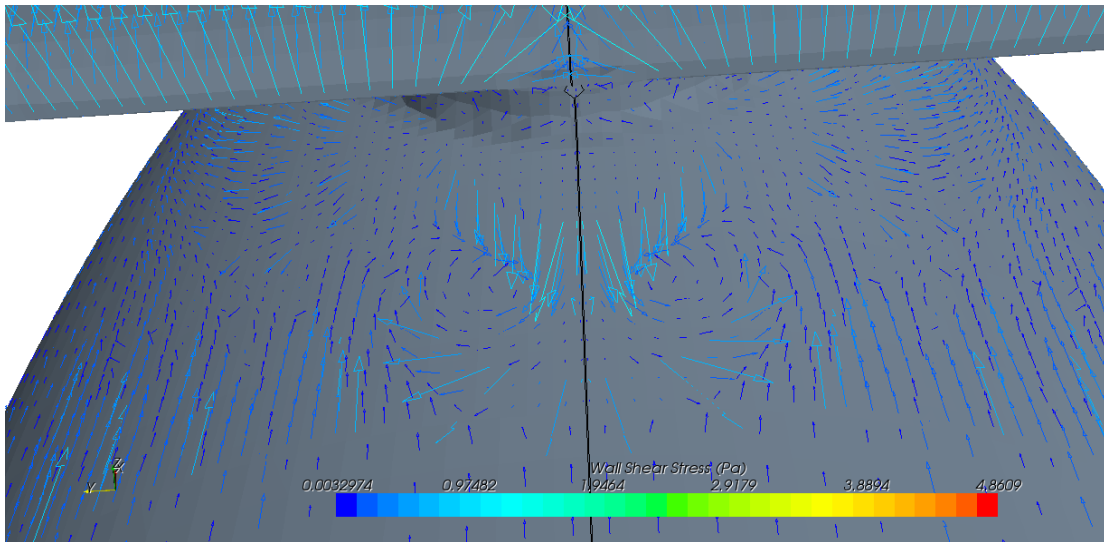
Figure 58: Result of wall shear stress calculation of wing-fuselage configuration 3 at zero pitch angles with 80 MPH airspeed.

Wing-fuselage configuration 4 shows a low lift and high drag between 0 to 5 degrees pitch angle, where stall occurs. Figure 59 displays the result of wall shear stress calculation of wing-fuselage configuration 4 vectors at zero degree pitch angle. No sign of large separation occurs in front of or behind wing-fuselage junction. It shows the separation at trailing edge of the wing near mid-span area. Turbulent transition area is quite large, which is associated with an earlier stall than for other configurations. A vortex is formed over the trailing edge at mid-span, where converging and diverging flow reacts against each other. An adverse pressure gradient occurs within this regions, which limits the performance of the wing; and thus performance limitation of the full body as well. The simulation does follow with the experiment, but tends to be more extreme. This means that this type of

phenomena could actually occur on configuration 4 during the experiment, but with

less severe condition.
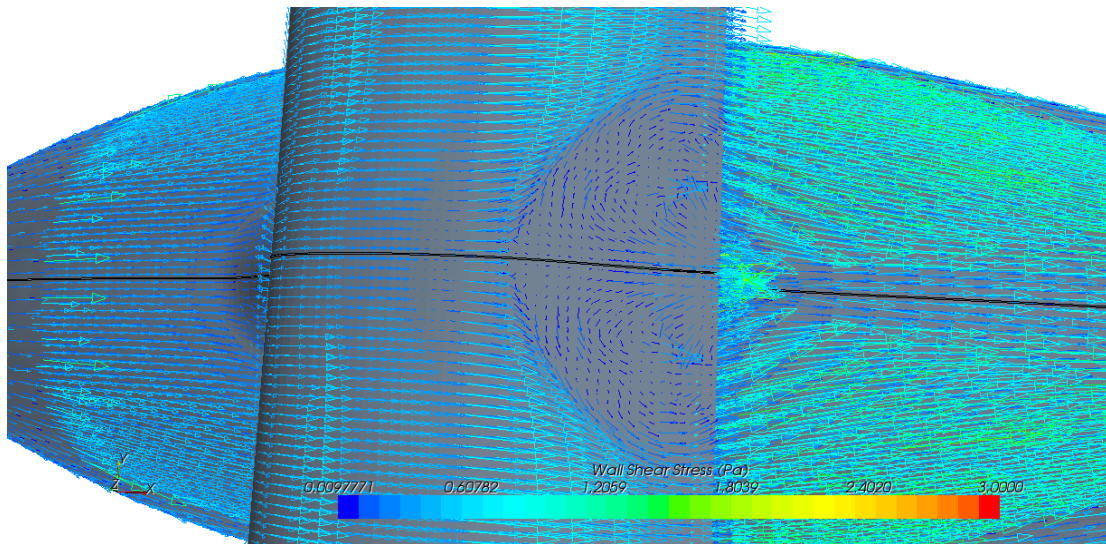
Figure 59: Result of wall shear stress calculation of wing-fuselage configuration 4 at zero pitch angles with 80 MPH airspeed
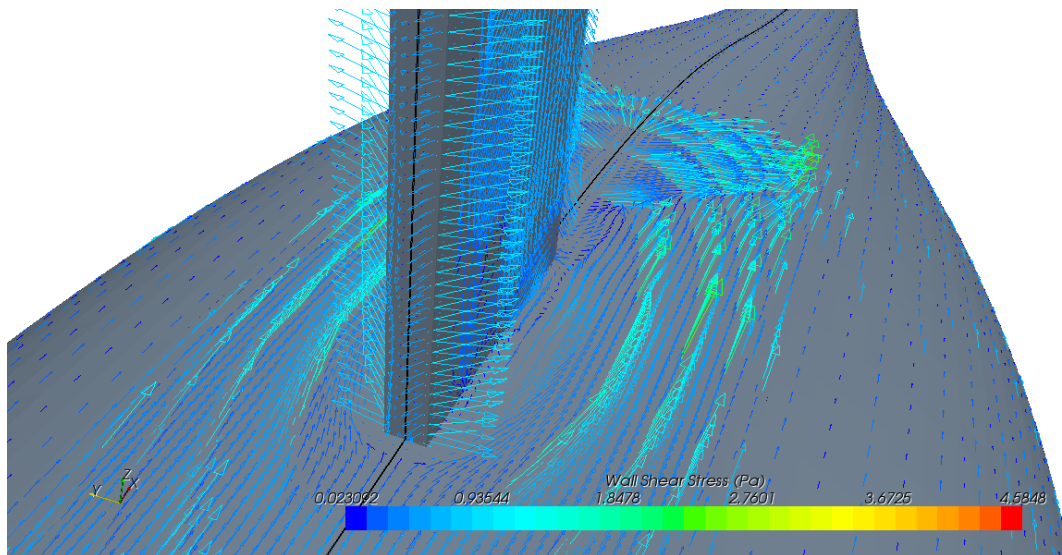
Figure 60: Vector result of wall-shear stress calculation on wing-fuselage configuration 5 at zero degree pitch angle at 80 MPH showing normal separation but no sign of flow reversal

Figure 60 shows the result of wall-shear stress calculation of configuration 5

at zero pitch angles. The strut link of the wing-fuselage is relatively thin, but also has

sharp edges. The flow separation in front of the fuselage due to the strut is quite subtle and uniform. It does not show any sign of vortex formation or any turbulence. The airstream on the strut itself slightly changes in direction because of the junction flow, but it smoothes out at certain distance above and below the junction. The wall shear stress also displays flow interaction behind the strut-fuselage junction. The airstreams sway away from the fuselage centerline, but no vortex formation or severe interactions occur.

Aerodynamic characteristics of five models are distinctive from each other, even though they are built with the same piece of wing and fuselage. Configuration 5 has the best performance. The visualization clearly shows that the wing-fuselage junction causes very little flow separation on the fuselage, and no separation at all on the wing. Configuration 2 also shows little separation in front of the fuselage with no sign of turbulence behind the wing-fuselage junction. Configurations 3 and 4 have high turbulence in the vicinity of the win-body junction which clearly limits their performance. The turbulence occurs on the wing for configuration 4 which illustrates the reason why its drag rises at higher rate than others at zero degree pitch. Configuration 1 has the worst performance, since the separations occur in many regions of the body.

At high positive pitch angles, ie 5 degrees, all wing-fuselage configurations have a tendency to stall. However, the experiment shows very subtle stall characteristics, whereas the simulation gives highly sensitive and strong loss of lift. Large separation zones and flow reversals appear in the stall regions, most often on the wing. Adverse pressures gradients occur within these stall regions. The typical

separation is mushroom pattern over the wing upper surface, differing somewhat in locations and specific details for each model.
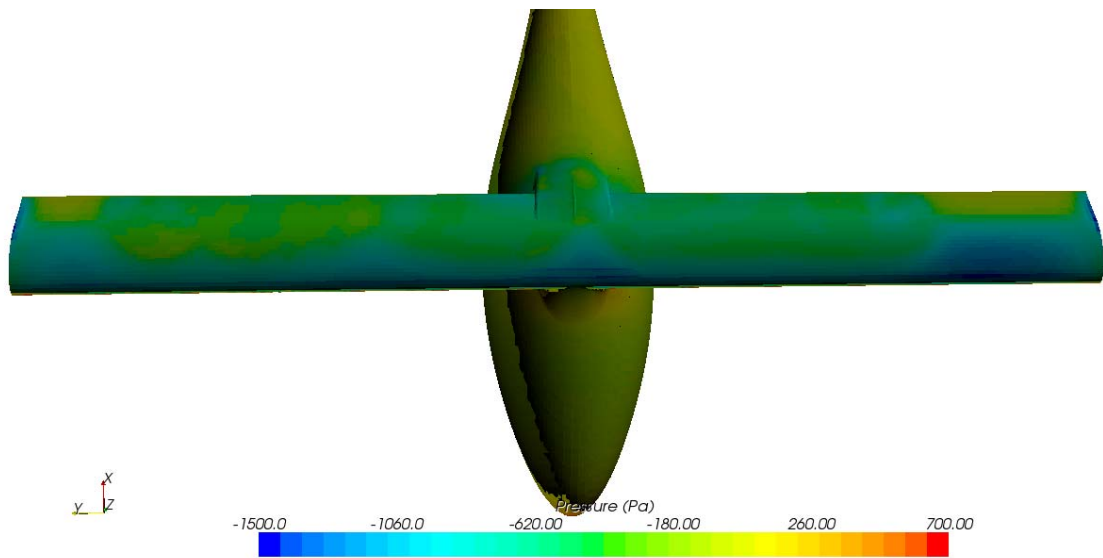
Figure 61: Results of Pressure distribution of wing-fuselage configuration 2 at +5 degrees pitch angle

Figure 61 shows the results of pressure distribution of configuration 2 at positive 5 degrees pitch. Flow separation zones are shown more clearly by figure 61. It is noticeable that the pressure changes unevenly over the wing surface. Pressure is raised on the wing upper surface compared to pitch angle of zero thus resulting in reduced lift from the simulation. The simulation results for this case show large lift loss, with lift coefficient dropping nearly 35% and its drag coefficient increasing by 125% from lift and drag at zero degree pitch.
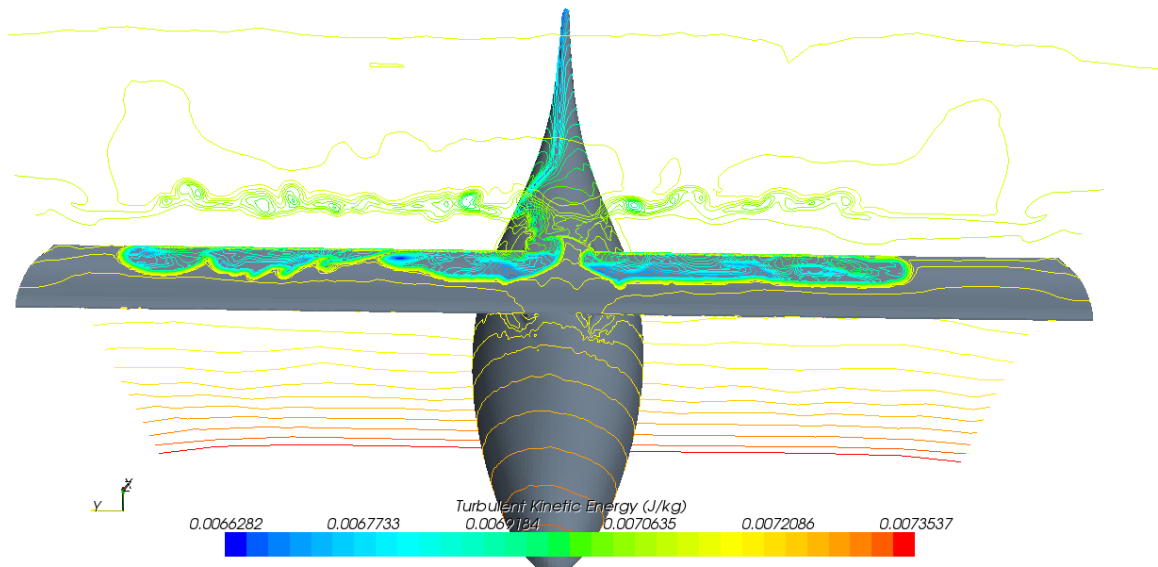
Figure 62: Result of Turbulent kinetic energy calculation of wing-fuselage configuration 2 at 5 degree pitch angles at 80 MPH airspeed

Figure 62 shows scalar plot of turbulent kinetic energy at the surface indicating the separation pattern over the top of the wing. The separation begins near the wing-fuselage junction and extends spanwise toward the wing tip with lower strength. The turbulent wake is further observed on fuselage in the wing region. A cut plane section behind the wing displays the turbulent wake generated from the wing stall cells.

The wing-fuselage configuration 4 has the strongest simulated stall characteristics. The wing stall initiates at zero degree pitch angles. The wing stall (maximum lift coefficient) occurs at zero degree pitch angle. Figure 63 shows the result of Mach number contours on the body and wing surfaces. Strong separation patterns occur on wing upper surface at +5 degrees pitch. It is inferred from the typical mushroom patterns that there is flow reversal along the trailing edge of the wing.

91
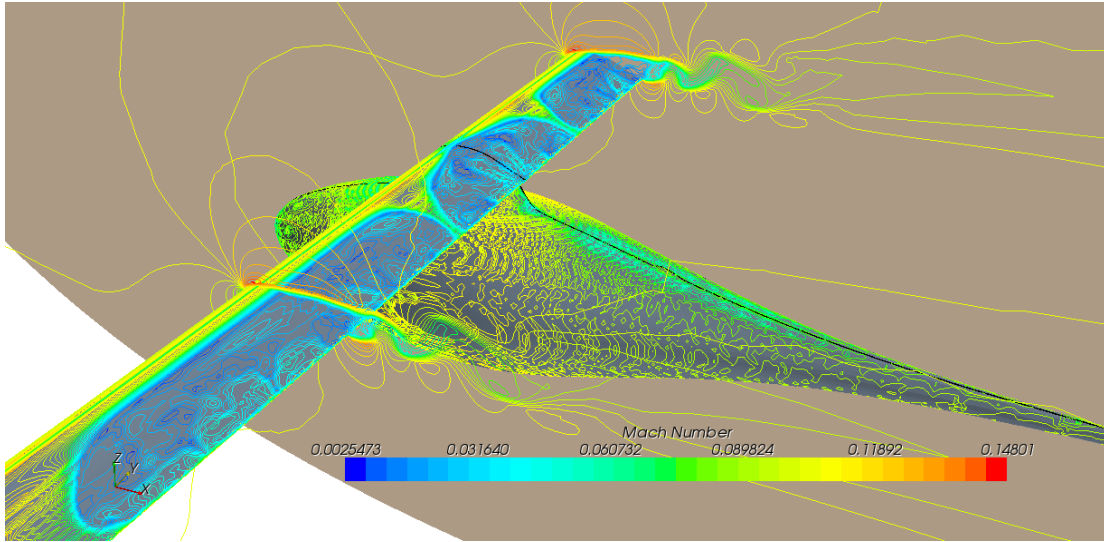
Figure 63: Results of Mach number distribution of wing-fuselage configuration 4 at +5 degree pitch angle at 80 MPH airspeed

The reduction of airspeed over the wing corresponds to a positive pressure increment relative to non-separated flow. As a result, lift is reduced, and drag is increased. Furthermore, the plane sections display highly turbulent wake behind the wing, which also causes some drag penalty. However, the fuselage is not affected by stalled wake of the wing, because the wing is located well above the fuselage. The stall characteristics of wing-fuselage configuration 4 exhibit more similarity to the wing alone than configurations with the wing at lower positions.

At -10 degree pitch angle, separation can also be observed beneath on the wing lower surfaces. Similar phenomenon to the high pitch angle stall occurs. This increases pressure for lower surface, but at the same time, it induces flow reversal and increases drag forces. Lift does not seem to experience a large influence by this type of separation. Figure 64 shows wing lower surface stall at -10 degree pitch angle. Turbulation occurs and spread spanwise to the side edges of the wing.

92
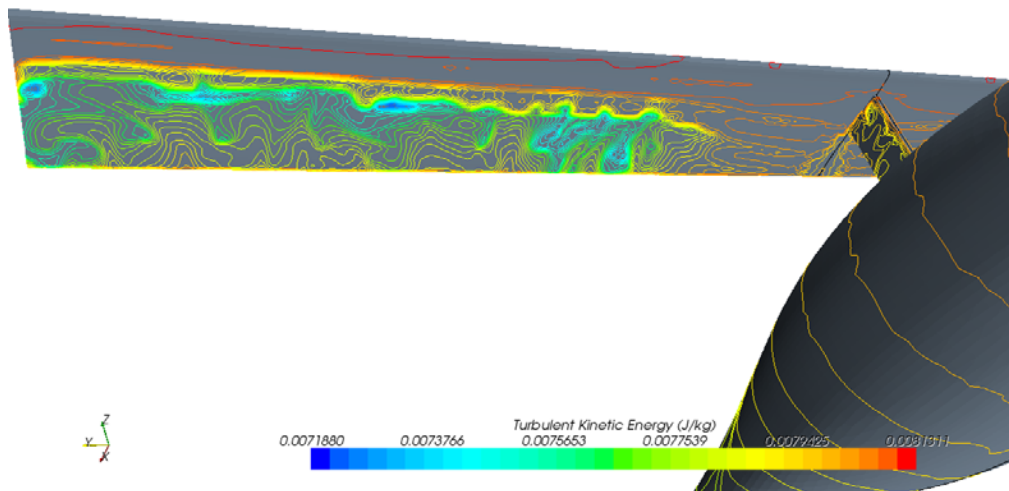
Figure 64: Result of turbulent kinetic energy distribution of wing-fuselage configuration 5 at -10 degree pitch angle at 80 MPH airspeed

Overall, the flow visualizations show that lower wing models may experience larger effects of flow separation because the turbulent separated flow over wing may also cause some on the fuselage. Configuration 1 is seen to suffer the most from this effect, plus it does not have any types of fillets to alleviate the flow separation at the junction. This may cause mid-wing design to be quite undesirable. However, high wing configurations also show some design flaw. Configuration 4 is observed to have flow separation over the top of the wing surface at moderate pitch angles.

In conclusion, the flow visualizations appear to show some true characteristics of all five models, but in reality, effects of wing-fuselage junctions may not be as severe as the simulation indicates.

6.3 Computational Results Discussion

The computational results clearly indicate the wing-fuselage configuration 5 has the best performance of overall the five configurations. Its ability to generate lift surpasses other models. It also has the smallest overall drag coefficient, which leads it to have the best lift to drag ratio. This agrees with experimental results. Flow visualization is helpful to determine flow behavior of the five models.

The wing-fuselage configuration 1 shows flow separation in front of the non-filleted junction with v-shape wing downwash on the fuselage aft section. This certainly lowers lifting capability and increases drag due to separation. The configurations 2 and 5, on the other hand, do not display high junction turbulence at non-stall angles of attack, which give them better results. The high-wing configuration 4 shows early stall due to strong adverse pressure gradient causing early separation on the wing surface. Its fuselage, though, does not seem to be affected by the flow separation. Pressure displays show smooth and effective distribution over the model except at high stall angles.

However, one needs to consider the accuracy of computational results compared to experimental results. Table 10 shows errors of the computational results in percentage in comparison with the experiment. The simulation of wing-fuselage configuration 3 gives the largest alteration from the experimental results. Lift prediction is generally more accurate than drag prediction, as seen in table 10.

Table 14: Erroneous in percentage in comparison of computational results and experimental results

MODEL	Configuration1	

Pitch [deg]	Lift Errors (%)	Drag Errors (%)
5	9.43	-47.19
0	8.67	-8.66
-1	39.93	58.09
-5	-8.66	50.77
-10	0.87	78.14
average	10.05	26.23

MODEL	Configuration2	

Pitch [deg]	Lift Errors (%)	Drag Errors (%)
5	15.67	-113.99
0	4.37	-74.71
-1	3.49	-67.32
-5	4.91	-16.643
-10	5.33	18.07
average	6.75	-50.92

MODEL	Configuration3	

Pitch [deg]	Lift Errors (%)	Drag Errors (%)
5	1.48	-55.35
0	1.253	-115.33
-1	12.48	-90.50
-5	10.57	-21.50
-10	6.65	4.63
average	6.49	55.61

MODEL	Configuration4	

Pitch [deg]	Lift Errors (%)	Drag Errors (%)
5	41.03	-141.75
0	3.80	-55.46
-1	0.01	-24.30
-5	0.07	19.82
-10	12.74	-31.25
average	11.53	-46.58864564

MODEL	Configuration5	

Pitch [deg]	Lift Errors (%)	Drag Errors (%)
5	7.26	0.93
0	2.20	-5.04
-1	2.41	4.49
-5	-0.79	53.22
-10	14.36	44.26
average	5.09	19.57

MODEL	Wing	

Pitch [deg]	Lift Errors (%)	Drag Errors (%)
5	11.99	-30.23
0	0.67	-31.14
-1	0.30	-42.17
-5	-2.27	-8.49
-10	-24.35	-157.50
average	-2.738	-53.91

The calculation of percentage error in Table 14 is obtained as follows,

$$Percentage\ erroneous = \left(\frac{Experiment - Simulation}{Experiment} \right) x100$$

According to table 14, lift coefficients obtained from the simulation are mostly lower than the actual lift coefficient from the experiment. The wing-fuselage configuration 4 has highest average errors of lift coefficient of 11.5%. All five models

have a tendency to have extreme drops in lift coefficient at high positive and high

negative angles of attack. On the other hand, computational results for wing lift

coefficient shows a small average error, even though there is still a high percentage of

error at +5 degrees and -10 degrees. The wing-fuselage configuration 5 results for lift

coefficient calculation is relatively good with only 5% error.
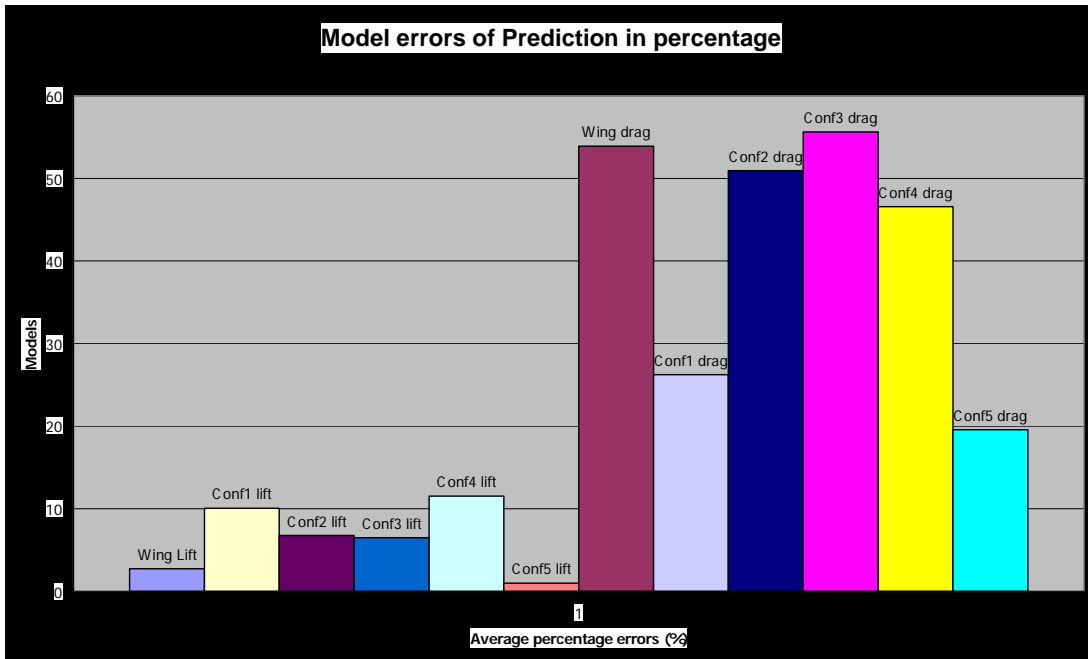
Figure 65: Errors of prediction in bar graph shown as average percentage of erroneous

The prediction of drag, in general, has a high level of uncertainty. Drag

coefficient in this simulation, in contrast of lift coefficient, shows high errors of

calculation. The percentages errors are in the order to 2 digits. The best drag

prediction is the wing-fuselage configuration 5 with average errors of 19 percent. The

CFD simulation in this case is not quite successful for drag prediction.

Many factors could cause the observed errors of drag prediction. One possible

factor is the environmental conditions. However, there is great confidence that they

are assigned correctly for the simulation, and have been confirmed during the

simulation. Airspeed is checked to ensure that the simulation is running at 80 MPH. Density, temperature, and pressure calculations ensure that the simulated free stream flow condition is running at the same or very close values to those in the wind tunnel experiment at each specific cases. The flow angles are set properly for every angle of attack. Turbulence intensity is obtained from the wind tunnel condition, which is a rather certain value. Therefore, it is believed that setting of environmental conditions is not the source of the errors.

Other factors such as mesh quality, and model errors are candidates as sources of error. To ensure the correctness of simulation settings, airfoil sections NACA 63-415 and NACA 63-015 were simulated. The two airfoil sections were drawn and extruded by the computer aided design software (CAD) to obtain 3 dimensional with the same spans. The same flow and turbulence conditions with 80 MPH airspeed were assigned to the NACA airfoil models. The results obtained were quite accurate with very small percentage of errors compared to theoretical results. This helps to confirm that the environmental set up is correct.

The volume mesh was generated with trimmer model which has a rectangular shape. It is an effective type of mesh to create the most accurate result of all 3 available types. Prior the simulation, meshes were checked by Star CCM+ auto-mesh check to ensure their qualities and validities. The free-stream boundary was also checked by parametric study to ensure sufficient space boundary such that it would not interfere or change flow condition before reaching the model. Mesh refinement were done to ensure that increasing or decreasing numbers of current mesh do not alter results by great degree. However, since the mesh is generated by automatic

program of Star CCM+, its quality might not by as could be generated by special purpose mesh generator software. It is suspected is that the predicted results of the wing-fuselage configuration 1 and 5, have the simplest shapes, are generally better than for the other models. Perhaps improvements in mesh quality and refinement, most accurate results could be obtained for the other models.

Errors between thee physical models and the geometry for the simulations could be one possibility that causes unmatched results. The actual models that were run in the wind tunnel experiment could have variances alteration from the computer aided design (CAD) models that were used to generate the simulated geometry. However, this is believed to be at most a small factor. The errors of the results can certainly be decreased with additional time and resources. Yet, this simulation experiences, nevertheless, greatly helps to envision flow behavior over the wing-fuselage intersection. It is also highly beneficial for studying different characteristics of wing-body geometries.

CHAPTER 7: Conclusion

Five configurations for joining the wing and fuselage have been evaluated in this study. The configurations have been illustrated by Figure 66 to 70 and are repeated here for ease of reference. The configurations numbered 1 through 5 have the wing in successively higher locations relative to the base.

Figure 66: Configuration 1 – Mid-wing with no filleting [7]

Configuration 1 has the wing penetrating the fuselage somewhat above the vertical center but still well below the top of the fuselage. This can be thought of as representative of "mid-wing" designs without fillets.
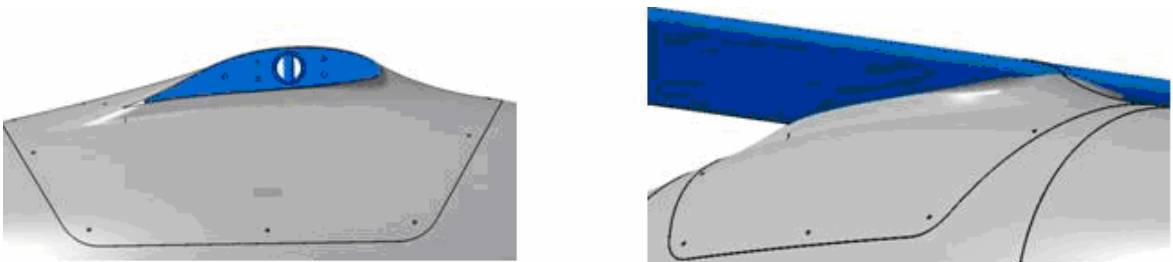
Figure 67: Configuration 2 – wing blended into top of fuselage [7]

Configuration 2 has the wing essentially sitting on top of the fuselage with the surface blending from the side view. The fuselage surface rises to meet the wing leading edge ahead of the wing.
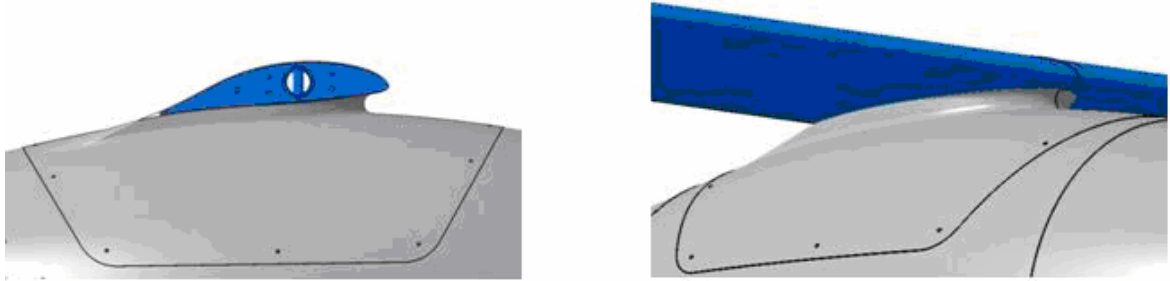
Figure 68: Configuration 3 - Wing at same height as Configuration 2 without surface blending [7]

Configuration 3 has the wing only very slightly higher than for configuration 2 but the fuselage has no blending ahead of the wing leading edge. Instead, there is what may be described as a base of a streamlined strut rising from the fuselage on which the wing sits. The front of this strut base is about 10% chord aft of the wing leading edge so that the wing leading edge protrudes forward from its support.
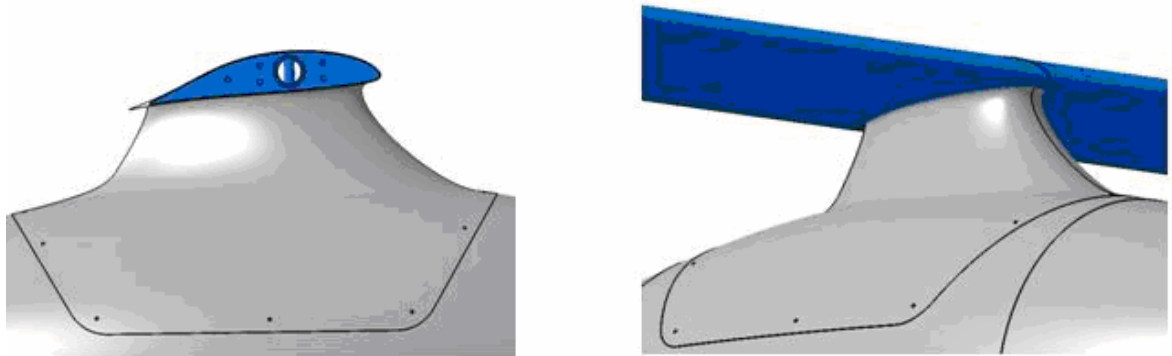
Figure 69: Configuration – Wing on streamlined strut about ½ chords above fuselage. [7]

Configuration 4 is supported on top of the streamlined strut about half a chord above the fuselage. The strut is streamlined and blended into the fuselage, but with no significant filleting at the juncture with the wing.
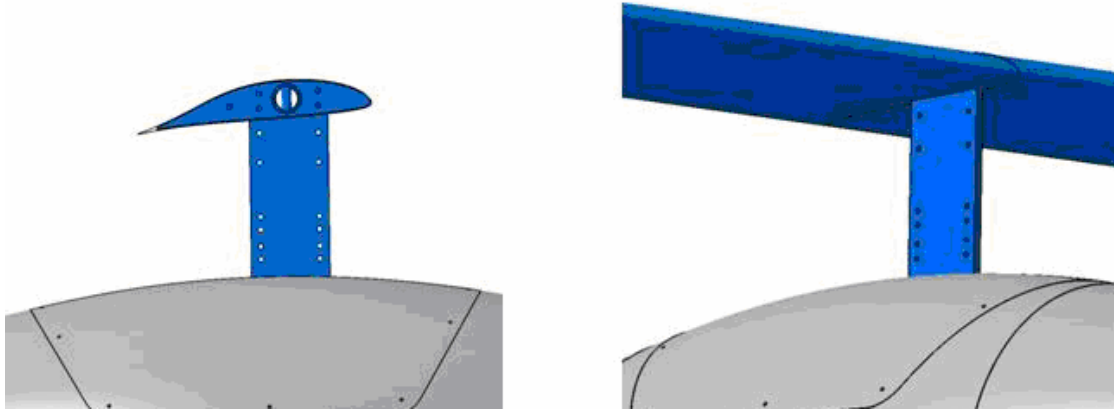
Figure 70: Configuration 5 – Wing on simple strut about 1 chord above fuselage with no fillets or blending [7]

Configuration 5 has the wing sitting on top of a simple thing rectangular strut with rounded edges supporting the wing about 1 chord above the top of the fuselage. There are no fillets or blending of the strut at its junctions with the fuselage or the wing.

Primary results of this investigation are summarized in the following 8 points.

1.   The high wing wing-fuselage configuration 5 with wing-fuselage flow fields isolated from one another as far as feasible shows the best overall performance of the five configurations subjected to test and analysis. It has the highest maximum lift to drag ratio with the lowest minimum drag coefficient. Its performance is superior in the primary operating regions. It is likely that the minimum drag could be reduced further with some attention to the strut-fuselage and strut-wing interference.

2.   The second best performance is shown by wing-fuselage configuration 2. It actually the exceeds performance of the wing-fuselage configuration 5 near and beyond the pitch for maximum lift. The performance of configuration 2 is less than configuration 5 in the primary operating regions.

3.   The worst performance overall is shown by configuration 1 which has the highest minimum drag coefficient, and lowest maximum lift to drag ratio. It also shows more extensive separation on the lower surface at high negative angles of attack.

4.   Configuration 4 has the lowest maximum lift coefficient, whereas wing-fuselage configuration 3 has highest maximum lift coefficient. Although along with the highest maximum lift coefficient, wing-fuselage configuration 3 also has high drag, which leads to its lower lift to drag ratio.

5.   Significant flow separation can be observed from 0 degree pitch angle and higher. The experiment shows that stall effect is very mild with the lift coefficient remaining near its maximum value instead of falling after significant separation begins.

6.   The predicted lift coefficient from the computational method is reasonably accurate, but drag prediction is rather inaccurate. The computational results are useful for flow visualization at the wing-fuselage junction, and to visualize the spread of separated regions as pitch angle increases.

7.   The computational result for the mid-wing configuration 1 shows effects of wing root wake on the fuselage, which increases amount of drag during in both operational and stalled regions. Wing-fuselage configuration 2 also suffers from wake effects on top of fuselage to some degree. The higher wing configurations 3-5 do not exhibit wake wash from the wing apparently due to the larger separation of the wing from the fuselage.

8.   Configuration 5 has a thin strut connection between the wing and fuselage. This is relatively clean aerodynamically. This produces the best performing configuration. However, it may not be practically feasible in terms of its structural properties.

There are a number of very interesting extensions of this study that would be very instructive for airplane designers. Several are listed here.

1.   Filleting studies: All of the configurations studied have some obvious possibilities for improving the smoothness of flow in the wing-fuselage or wing-strut or strut-fuselage junction areas.   Systematic efforts to improve the performance of each configuration by filleting would yield valuable insights.

2.   Experimental flow visualizations: Very useful information would be gained by repeating the same experiments with extensive flow visualization as part of the test activity. It would be very desirable to include both surface flow visualizations and flow field visualizations. This would be expected to yield direct insight from the experiments and would assist in efforts to improve the correlation between the experiments and the computational results.

3.   Finite wing effects: The configurations studied here all had the same wing which extended essentially the full width of the wind tunnel. This was done to limit the number of variables. However, it could be expected that finite wing effects could enter into the trade effects, so it would be instructive to include aspect ratio effects on the wing-body junction optimization.

4.   Computational Method Improvements: It would be very useful to revisit the computational methods of this study with sufficient resources to close the

Future work could be appointed to study complete airplane model. Horizontal, vertical tail and other components can be added into future investigation. Optimization of component locations on specific model can be study and applied in the experiment. Computational fluid dynamics method can be improved for better accuracy of prediction. Accurate simulations would help on the design process prior to the wind-tunnel experiment, which would reduce time and resources of the investigation.

Bibliography

[1] Anderson, J. D., Jr., *Fundamental of Aerodynamics*, Third Edition, McGraw-Hill, 2001.

[2] Barlow, J., Rae, W., Pope, A., *Low Speed Wind Tunnel Testing*, Jon Wiley & Sons, 1999.

[3] Hoerner, S. F., *Fluid-Dynamic Drag*, (S. F. Hoerner, Midland Park, New Jersey, 1958).

[4] Schlichting, H., Truckenbrodt E., *Aerodynamics of the Airplane*, McGraw-Hill, 1979.

[5] Simpson, R. L., "*Junction Flow*," Annual Reviews Fluid Mech. 2001. 33:415-43, 2001.

[6] CD-Adapco, "*Instruction Manual of Star CCM+ 2.08.007*," 2007.

[7] Hatfield, D., Garret, P., "*Wing-body interface drag test experiment proposal*," Aurora Flight Sciences., 2007.

[8] Kentfield, J.A.C., Jones, H. L., "*Fuselage-Wing Interference Drag of Aircraft with Relatively Short, Pod-Type, Fuselages*," AIAA, 2002.

[9] Maughmer, M., Hallmann, D., Ruszkowski, R. Chappel, G., Waitz, I., "*Experimental investigation of Wing/Fuselage Geometries*," J. Aircraft, Vol.26, No.8, 1999

[10] Althaus, D., "*Wind-Tunnel Measurements on Bodies and Wing-Body Combinations,*" Institut fur Aerodynamik und Gasdynamik der Universitat Stuugart.

[11] Green, B., Whitesides, L. "A Method for Designing Leading-Edge Fillets to Eliminates Flow Sepration," AIAA, 2000.